

Award Number: W81XWH-11-1-0248

TITLE: Echo-Planar Imaging-Based, J-Resolved Spectroscopic Imaging for Improved Metabolite Detection in Prostate Cancer

PRINCIPAL INVESTIGATOR: Michael Albert Thomas Ph.D.

CONTRACTING ORGANIZATION:
University of California, Los Angeles
Los Angeles, CA 90024-1406

REPORT DATE: December 2016

TYPE OF REPORT: Final

PREPARED FOR: U.S. Army Medical Research and Materiel Command
Fort Detrick, Maryland 21702-5012

DISTRIBUTION STATEMENT: Approved for Public Release;
Distribution Unlimited

The views, opinions and/or findings contained in this report are those of the author(s) and should not be construed as an official Department of the Army position, policy or decision unless so designated by other documentation.

REPORT DOCUMENTATION PAGE			<i>Form Approved</i> <i>OMB No. 0704-0188</i>		
Public reporting burden for this collection of information is estimated to average 1 hour per response, including the time for reviewing instructions, searching existing data sources, gathering and maintaining the data needed, and completing and reviewing this collection of information. Send comments regarding this burden estimate or any other aspect of this collection of information, including suggestions for reducing this burden to Department of Defense, Washington Headquarters Services, Directorate for Information Operations and Reports (0704-0188), 1215 Jefferson Davis Highway, Suite 1204, Arlington, VA 22202-4302. Respondents should be aware that notwithstanding any other provision of law, no person shall be subject to any penalty for failing to comply with a collection of information if it does not display a currently valid OMB control number. PLEASE DO NOT RETURN YOUR FORM TO THE ABOVE ADDRESS.					
1. REPORT DATE December 2016		2. REPORT TYPE Final		3. DATES COVERED 30Sep2011 - 29Sep2016	
4. TITLE AND SUBTITLE Echo-Planar Imaging-Based, J-Resolved Spectroscopic Imaging for Improved Metabolite Detection in Prostate Cancer			5a. CONTRACT NUMBER W81XWH-11-1-0248		
			5b. GRANT NUMBER		
			5c. PROGRAM ELEMENT NUMBER		
6. AUTHOR(S) Michael Albert Thomas Ph.D. E-Mail: athomas@mednet.ucla.edu			5d. PROJECT NUMBER		
			5e. TASK NUMBER		
			5f. WORK UNIT NUMBER		
7. PERFORMING ORGANIZATION NAME(S) AND ADDRESS(ES) AND ADDRESS(ES) University of California, Los Angeles Los Angeles, CA 90095			8. PERFORMING ORGANIZATION REPORT NUMBER		
9. SPONSORING / MONITORING AGENCY NAME(S) AND ADDRESS(ES) U.S. Army Medical Research and Materiel Command Fort Detrick, Maryland 21702-5012			10. SPONSOR/MONITOR'S ACRONYM(S)		
			11. SPONSOR/MONITOR'S REPORT NUMBER(S)		
12. DISTRIBUTION / AVAILABILITY STATEMENT Approved for Public Release; Distribution Unlimited					
13. SUPPLEMENTARY NOTES					
14. ABSTRACT Purpose: 1) To implement an echo-planar imaging (EPI)-based 2D J-resolved spectroscopy on a 3T MRI/MRS scanner; 2) To evaluate the multi-voxel 2D J-resolved echo-planar spectroscopic imaging (EP-JRESI) in malignant prostate cancer (PCa) patients, benign prostatic hyperplasia (BPH) patients and healthy prostates. 3) To develop and further optimize the ProFit algorithm to post-process the multi-dimensional MRS data from different prostate pathologies. Scope: Improved cancer detection (specificity) in differentiating malignant from benign prostate cancer can be achieved using a novel four-dimensional (4D) EP-JRESI. Improved spectroscopic imaging techniques will enable unambiguous detection of metabolites and the lipids in situ, which could potentially complement existing diagnostic modalities commonly used in PCa. Progress and Major Findings: After successful implementation of the 4D EP-JRESI sequence on a 3T MRI scanner, the 4D EP-JRESI data were recorded in 47 PCa patients and 9 healthy males during the funded years. The sequence has been compiled using Siemens different platform compilers and the sequence is currently shared with other sites. Seven peer-reviewed manuscripts, 13 conference abstracts and two book chapters have been published so far with one more manuscript in preparation. Our abstract to the 2017 ISMRM meeting has been invited for oral as well as ePoster presentations.					
15. SUBJECT TERMS: Digital Rectal Examination, prostate specific antigen, Four Dimensional (4D) Echo-Planar J-Resolved Spectroscopic Imaging (EP-JRESI); Citrate, Choline, Creatine, Spermine, 3Tesla MRI scanner, Endo-rectal MR coil, WET Water Suppression, prostate cancer (PCa), benign prostatic hyperplasia (BPH), prior-knowledge fitting					
16. SECURITY CLASSIFICATION OF:			17. LIMITATION OF ABSTRACT	18. NUMBER OF PAGES	19a. NAME OF RESPONSIBLE PERSON USAMRMC
a. REPORT U	b. ABSTRACT U	c. THIS PAGE U			19b. TELEPHONE NUMBER (include area code)
			UU	59	

Table of Contents

	Page
Introduction.....	4
Body.....	4
Key Research Accomplishments.....	10
Reportable Outcomes.....	10
Conclusion.....	12
References.....	12
Appendices.....	14

Introduction: Prostate cancer (PCa) is the most common cancer in men in several countries, with the American Cancer Society (ACS) estimating 241,740 new cases of PCa to be diagnosed and deaths of 28,170 men of PCa (1). Due to its prevalence in the male population as well as its unpredictable clinical course, early detection and diagnosis have become a priority for many health care professionals. Another method for staging prostate cancer is through imaging techniques including ultrasound, computed tomography (CT), and magnetic resonance imaging (MRI) with or without the help of dynamic contrast enhancement modeling (DCE-MRI), diffusion weighted imaging (DWI), and magnetic resonance spectroscopy (MRS) (2-5). MRS is a powerful tool for exploring the cellular chemistry of human tissues (3,5,6-11). There is a growing body of evidence that ¹H MRS may contribute to the clinical evaluation of prostate cancer and also for evaluating the metabolic alterations due to therapy. There have been no reports on combining two spectral dimensions with two-dimensional (2D) or three dimensional (3D) spatial encoding applicable to prostate cancer. Acceleration of magnetic resonance spectroscopic imaging (MRSI) has been demonstrated using echo-planar imaging techniques (12-13). Recently, Schulte et al. have successfully developed an algorithm called prior-knowledge fitting (ProFit) to quantify metabolite concentrations using the JPRESS spectra recorded using a Philips 3T MRI scanner (14). It was demonstrated that metabolite quantitation of JPRESS spectra with ProFit was accurate, robust and yielding generally consistent results, both *in vivo* and *in vitro*. Their results suggest that the number of quantifiable prostate metabolites can be increased from 3-4 with 1D PRESS/LC-Model to more than 10 with JPRESS/ProFit (15-16).

Body:

*i) **Proposed Task 1 (Months 1-6):** To implement a multi-voxel based extension of the JPRESS sequence, in which two spectral encodings will be combined with two spatial encodings using the new Siemens VB17a platform. This four-dimensional (4D) data acquisition scheme will be accomplished utilizing the EPI approach that is commonly used for spatial encoding in MRI.*

The 4D echo-planar J-resolved spectroscopic imaging (EP-JRESI) sequence as shown in Fig.1 was successfully compiled using the Siemens VB17a compiler. The volume of interest (VOI) was localized using three selective radio-frequency (RF) pulses similar to the PRESS sequence that is routinely used by MR researchers around the world. There were B_0 crusher gradient pulses around the two refocusing 180° (π) RF pulses. The EPI read-out enabled readout of 512 maximum t_2 spectral points and $16k_x$ spatial points. Remaining spectral and spatial encodings were accomplished using incremented Δt_1 and k_y . Total echo time ($TE = TE_1 + TE_2$) was 30 ms. The 4D raw data was typically $512t_2 * 64-100t_1 * 16k_x * 16k_y$. Since the 4D EP-JRESI sequence is a home-built sequence, there is no manufacturer supplied extraction program to post-process the acquired data. Hence, our group had to develop extraction codes using the MATLAB library.

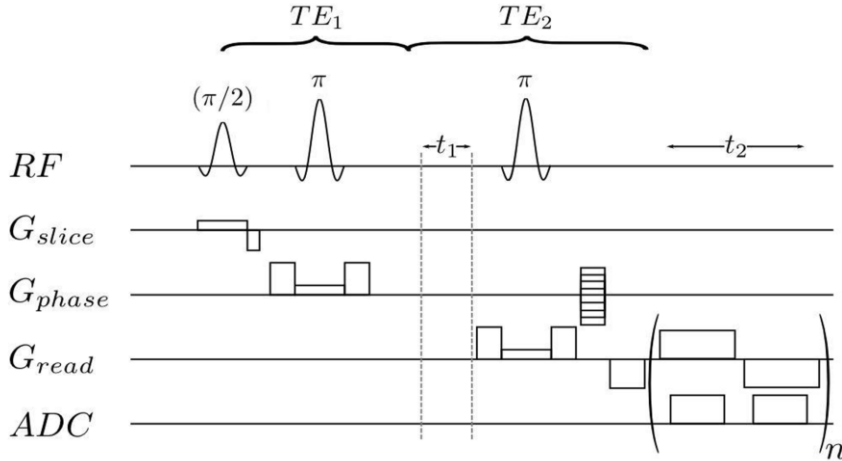


Figure.1. The 4D EPJRESI sequence showing two spatial encodings (k_x, k_y) and two spectral encodings (t_2, t_1). Inherent acceleration of k_x and t_2 is enabled here by the echo-planar imaging (EPI)-based read-out.

ii) **Proposed Task 2:** To evaluate the EPI-based JPRESS using a prostate phantom containing several metabolites which have been reported in prostate tissues, and to optimize the EP-JRESI sequence and other acquisition parameters using the phantom (Months 6-12).

The sequence was tested using a prostate phantom containing 10 different metabolites at physiological concentrations (pH set to 7.2). A 500 ml prostate phantom was prepared containing the following metabolites at physiological concentrations as reported in healthy human prostate (15-16): Citrate (Cit, 50mM), Creatine (Cr, 5mM), Choline (Cho, 1mM), Spermine (Spm, 6mM), myo-inositol (mi, 10mM), Phosphocholine (PCh, 2mM), Taurine (Tau, 3mM), Glutamate (Glu, 4mM), Glutamine (Gln, 2.5mM) and Scyllo-Inositol (sl, 0.8mM). Shown in Fig.2A is an axial MRI slice image showing the multi-voxel grids of MRSI with the yellow boundary of the field of view (FOV), and the white box representing the volume of interest (VOI) localized by the PRESS sequence which is an integral part of the EP-JRESI sequence. The following parameters were used for acquiring the fully sampled EP-JRESI data: TR/TE=1500/30ms, 16 phase encodes (k_y), 32 read-out points (k_x) with oversampling, 512 \pm read-out trains resulting in 512 pairs of complex spectral points in the 2nd spectral dimension (t_2), 100 t_1 increments for the indirect spectral dimension and one average per encoding. A total duration of 40 minutes was necessary to acquire this water-suppressed EP-JRESI data. A non-water-suppressed EP-JRESI data using 4 averages with only one t_1 increment was used for eddy current and phase correction of the suppressed data (14). After apodization and Fourier transformation of this 4D data, the reconstructed multi-voxel 2D J-resolved spectra (shown in Fig.2C) were overlaid on top of the 16x16 spatial grids. An extracted 2D J-resolved spectrum (3ml) around the center of the VOI is shown in Fig. 2B.

As mentioned before, Fig.2 demonstrates the successful implementation of the 4D EP-JRESI sequence on the 3T MRI scanner. Significant programming efforts were necessary for accomplishing this on both acquisition and post-processing fronts.

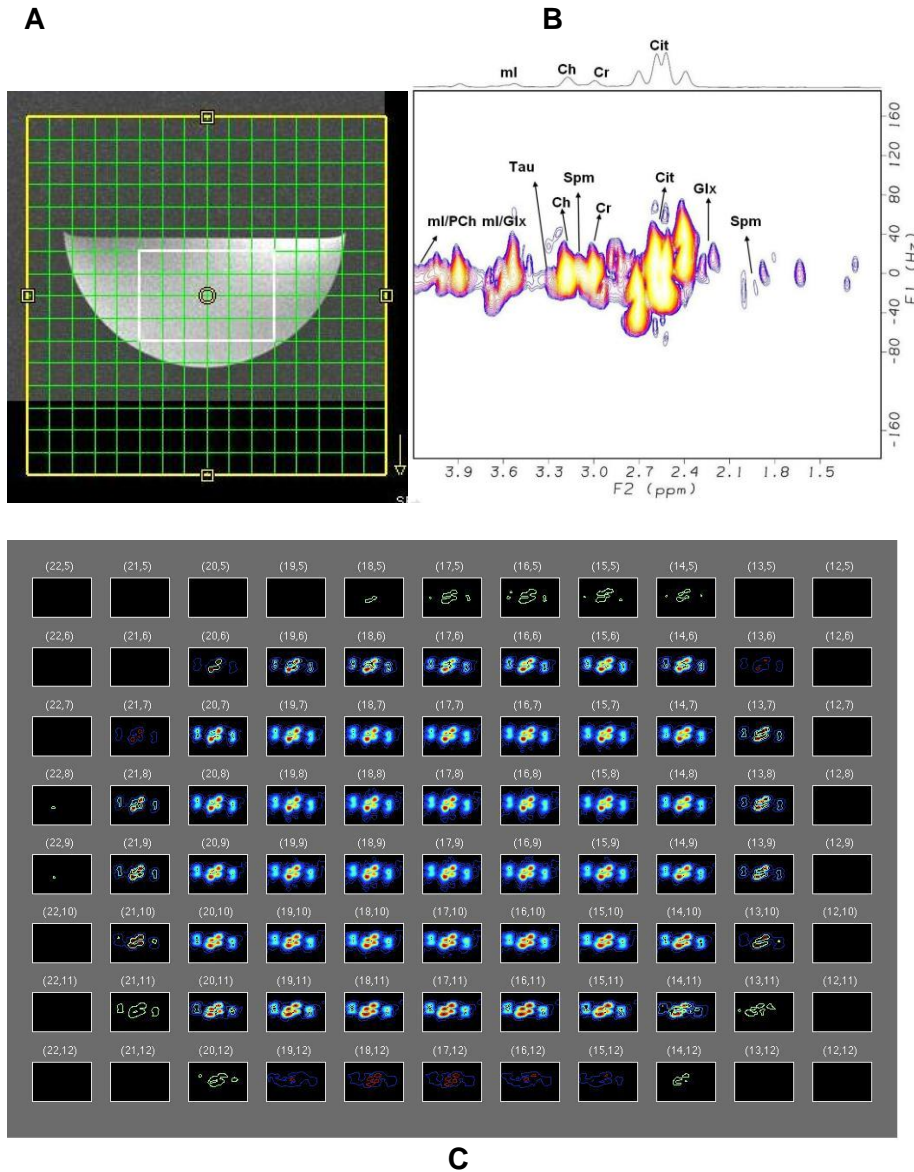


Figure 2.A. An MRI axial slice image of the prostate phantom showing the VOI localization (white box) and field of view (FOV) for spatial encoding (yellow grids). **B.** Extracted 3ml 2D J-resolved spectrum from the center of the phantom. **C.** Multi-voxel display of Cit recordable within the white box boundary; the peaks outside the VOI are due to Gibbs' ringing or bleed.

iii) Proposed Task 3: To develop, evaluate and optimize the prior-knowledge basis set spectra using the GAMMA-simulation and prostate phantom solutions as prior knowledge for the multi-voxel based JPRESS spectra recorded using the 3T MRI scanner (**Months 6-12**).

Shown in Fig.3 is a 2D J-Resolved spectrum recorded in a 27 y.o. healthy male. Presence of several metabolites is clearly marked here. More than 10 basis-sets were constructed for the prior-knowledge fitting developed using the GAMMA library (17).

Figure 3. A 2D J-resolved spectrum recorded in a healthy male prostate.

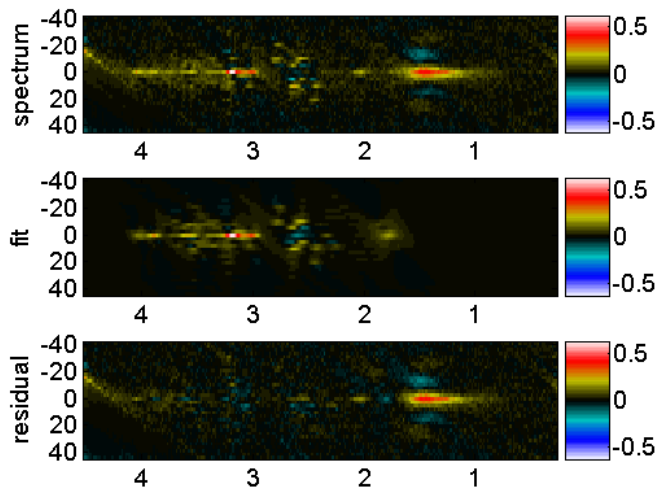
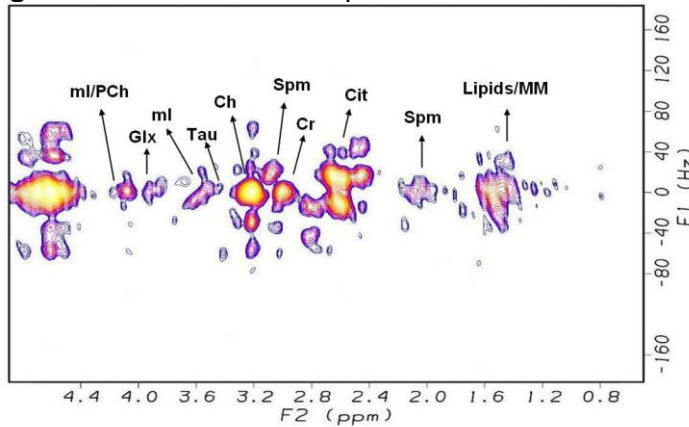


Figure 4. Prior-knowledge J-resolved spectra for the prostate metabolites: Experimental (top), fitted using ProFit algorithm (middle) and residual (bottom).

Shown in Fig.4 are 2D plots showing ProFit quantitation using MATLAB codes. Using the spectral data recorded in the peripheral zone of the 27y.o. healthy volunteer, following ratios were quantified (/Cr): PCh: 0.09, Cit: 7.36, Spm: 8.55, Glycerlphosphocholine (GPC): 0.483, Cho: 0.01, ml:3.79, sl:0.012, Tau:1.47, Gln: 0.03, Glu:1.52. These preliminary results show the feasibility of detecting more metabolites in the 4D EP-JRESI spectrum than the conventional MRSI showing 3-4 metabolites only.

iv) Proposed Task 4: *To record the 4D EP-JRESI spectra in the peripheral, central and transition zones of healthy prostates. (Months 6-18).*

A 32 yo healthy human subject was investigated on the 3T MRI scanner using the quadrature body coil “transmit” and external body matrix “receive” coil assembly. The following parameters were used to acquire the EP-JRESI data: TR/TE=1.5s/30ms, 2 averages, 512 t_2 , oversampled 32 k_x , 64 increments along the indirect spectral (t_1) and 16 spatial k_y dimensions. In Fig. 5A, an axial MRI of the abdomen is shown displaying the VOI covering the prostate localized by the PRESS sequence and the EP-JRESI grids. The multi-voxel display of a selected region is shown in Fig. 5B. The 2D J-resolved spectrum (2ml) extracted from the location (*) is shown in Fig. 5C. The 2D diagonal and cross peaks

of Cit and other metabolites are visible. As shown below, the endorectal “receive” coil is expected to facilitate at least one order of magnitude higher sensitivity than that of the body matrix assembly used here.

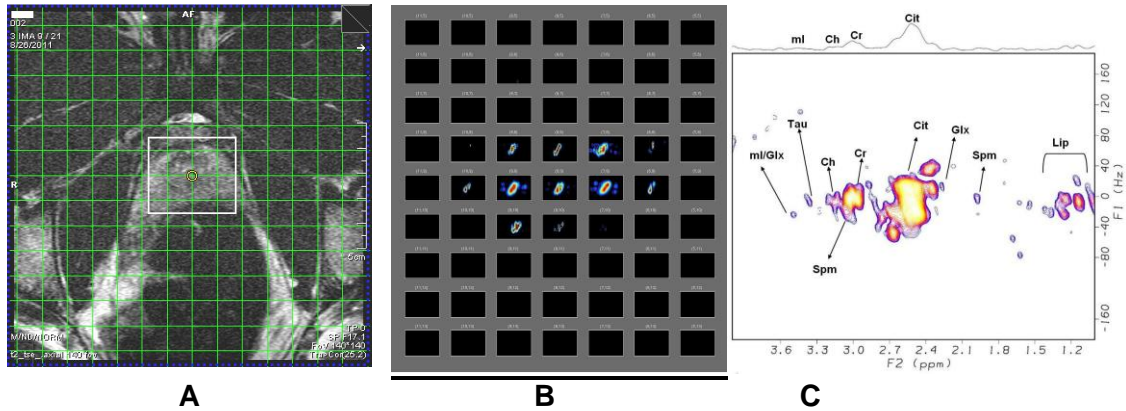


Figure 5. A. An axial MRI slice of the 32y.o. healthy male subject showing the VOI and MRSI grids. **B.** Expanded multi-voxel 2D spectra showing the Cit multiplets. **C.** The 2D J-resolved spectrum extracted from a 2ml voxel of the peripheral zone.

Using the endorectal "receive" coil, another 4D EP-JRESI data acquired in a 61 year old PCa patient having PSA of 9.1 and two malignant lesions (GS3+4 in the right base and GS4+3 in the right mid regions) and extracted spectra from 2 different locations (1ml) are shown in Figure 6. The extracted two spectra from the malignant masses in the right mid (GS4+3) (ii) and right base (iii) regions, and iv) healthy peripheral zone.

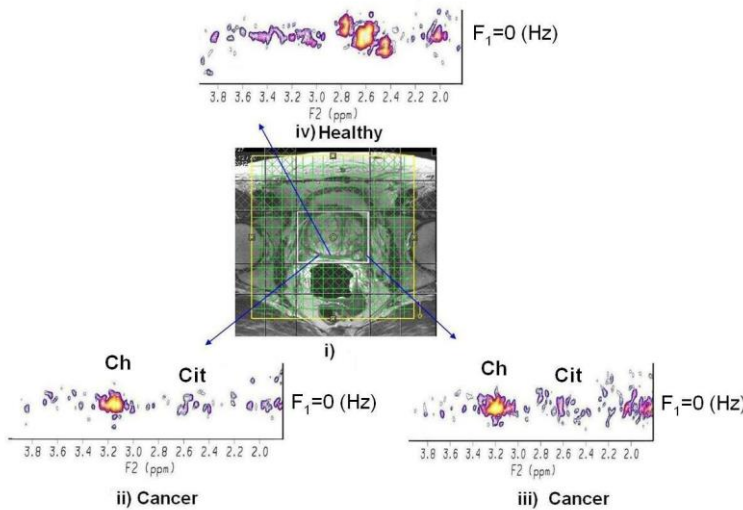


Figure 6. i) An axial T₂W MRI slice showing the multi-voxel EP-JRESI grids; extracted 2D JPRESS spectra of malignant voxels (ii) and (iii), and the healthy voxel in the peripheral zone (iv).

Nine healthy males have been investigated.

v) Proposed Task 5: To record the multi-voxel-based 2D spectra in the peripheral, central and transition zones of patients with BPH and malignant prostate cancer. The prostate metabolite concentrations calculated using the ProFit algorithm prepared for the multi-

voxel data will be compared with LC-Model processed 1D spectral based MRSI data (Months 18-48).

Forty seven malignant prostate cancer patients and nine healthy males were investigated during the funded period. The 4D EP-JRESI data were recorded using the following parameters: TR/TE=1.5s/30ms, 2 averages, 512 t_2 , oversampled $32k_x$, 64 increments along the indirect spectral (t_1) and 16 spatial k_y dimensions; the endorectal "receive" coil. The oversampled $32k_x$ were processed to normal $16k_x$ points. First, the 4D NUS EP-JRESI data was acquired in a 71 year old PCa patient; In our recent publication, we had included twenty two PCa patients with a mean age of 63.8 years (range: 46–79 years) who subsequently underwent radical prostatectomy. Patients' Gleason scores varied between 6 and 9. Prostate-specific antigen (PSA) levels varied from 0.7 to 22.8 ng/mL (mean of 6.23 ng/mL).

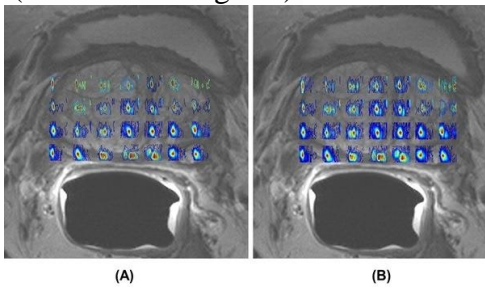
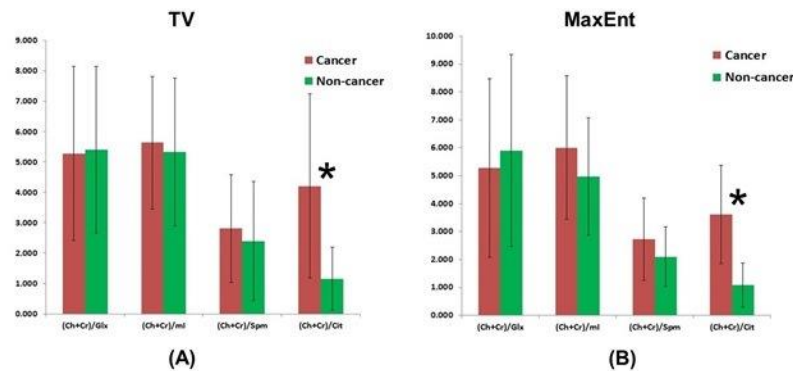


Figure 7. Spatial maps of (Ch +Cr) for TV (A) and MaxEnt (B) non-linear reconstruction methods of the 4D EP-JRESI data recorded in a 74 year old PCa patient. The EP-JRESI was overlaid on top of the T₂ weighted MRI.

We were able to reproduce the above mentioned findings in more patients with known GS, and also, in remaining patients whose histology findings were not known. 2D peak (cross and diagonal) volumes were defined by the operator in the frequency domain 2D JPRESS data for this pilot analysis. Two different non-linear reconstruction methods such as maximum entropy (MaxEnt) and total variation (TV). As evident in Fig.8, selected ratios showed significant changes ($p < 0.05$); however, this outcome from a small group of PCa patients

Fig.8. Metabolite ratios of Cit, Spm, ml and Glx in cancer and non-cancer locations processed by non-linear reconstruction methods using TV and MaxEnt.



needs to be treated with caution showing a necessity for further research using larger patient cohorts.

Key Research Accomplishments

- Evaluation of the 4D EP-JRESI sequence in 47 malignant prostate cancer patients who had also benign masses and 9 healthy male subjects.
- The sequence was tested using phantom model solutions first using metabolites known to exist in prostate cancer (citrate, creatine, choline, glutamate, glutamine, etc.).
- A prior knowledge based fitting algorithm called ProFit was developed to process the 4D EP-JRESI data.
- We have made progress on compressed sensing reconstruction of the non-uniformly undersampled 4D EP-JRESI sequence using different reconstruction methods such as maximum entropy, total variation (TV), etc. The results were published in two different peer-reviewed manuscripts. This will facilitate shortening the endorectal spectral acquisition and reducing the patient inconvenience during the scan.
- The sequence has been compiled for different Siemens 3T MRI scanner platforms (VB17a, VD13a, VD13D, VE11A, VE11B and VE 11C between 2012 and 2017).
- We have been sharing the sequence with outside researchers (Harvard, University of Pennsylvania, Switzerland, Australia, Canada) after the research agreements were signed by both parties for sharing the compiled object code.
- Using the preliminary results obtained using this IDEA grant, we had submitted a NIH R01 grant application submission entitled “Fast J-resolved Prostate MR Spectroscopic Imaging and Non-linear Reconstruction” was resubmitted on February 5, 2015 and we plan to resubmit this grant to NIH.

Reportable Outcomes:

A. Peer-reviewed Publications:

1. Nagarajan R, Margolis D, Raman S, et al. MR Spectroscopic Imaging and Diffusion-Weighted Imaging of Prostate Cancer With Gleason Scores. *J Magn Reson Imaging* 2012; 36: 697-703 [**PMID: 22581787**].
2. Nagarajan R, Margolis D, Raman S, et al. Correlation of Gleason Scores with Diffusion-Weighted Imaging Findings of Prostate Cancer. *Advances in Urology* 2012; 2012:374805. Epub 2011 Dec 15 [**PMID: 22216026**].
3. McClure TD, Margolis DJ, Reiter RE, et al. Use of MR imaging to determine preservation of the neurovascular bundles at robotic-assisted laparoscopic prostatectomy. *Radiology*. 2012 Mar;262(3):874-83. Epub 2012 Jan 24 [**PMID: 22274837**].
4. Furuyama J, Wilson NE, Burns BL, et al. Application of Compressed Sensing to Multidimensional MR Spectroscopic Imaging in Human Prostate. *Magn Reson Med* 2012;67: 1499-1505 [**PMID: 22505247**].
5. Nagarajan R, Margolis D, Raman S, et al. MR Spectroscopic Imaging of Peripheral zone in Prostate Cancer using a 3T MRI scanner: Endorectal versus External Phased array Coils. *Magnetic Resonance Insights* 2013; 6: 51-58 [**PMID: 25114544**; **PMCID:PMC4089813**].

6. Thomas MA, Nagarajan R, Huda A, et al. Multidimensional MR Spectroscopic imaging of Prostate Cancer In vivo. *NMR in Biomedicine* 2014 Jan;27(1):53-66. Epub 2013 July 31(Epub ahead of print). [PMID: 23904127].
7. Nagarajan R, Iqbal Z, Burns B, et al. Accelerated Echo Planar J-Resolved Spectroscopic Imaging in Prostate Cancer: Nonlinear Reconstruction Using Total Variation and Maximum Entropy. *NMR in Biomedicine* 2015; 28: 1366–1373. [PMID:26346702; PMCID:PMC4618758].

B. Presentations:

- 1) “Novel Multi-dimensional Magnetic Resonance Spectroscopic Imaging: Implementation and Pilot Validation in Prostate and Breast Cancer in vivo” was submitted and presented at the 17th International Biophysics Congress (IUPAB) conference in Beijing, China (Oct.30-Nov.3, 2011).
- 2) Summary of the implementation of the 4D EP-JRESI sequence and evaluation of it in healthy males was presented at the 2011 Radiological Society of Northern America (RSNA) meeting (Nov.-Dec.2011) in Chicago, IL. 2012.
- 3) "Accelerated Multi-Voxel Two-Dimensional In Vivo Spectroscopy Using Compressed Sensing" was presented at the 53rd Experimental NMR Conference (ENC) meeting in Miami, Florida (April 15-20, 2012).
- 4) "Accelerating Echo-Planar J-Resolved Spectroscopy of the Prostate using Compressed Sensing in a Clinical Setting" was presented at the 20th International Society of Magnetic Resonance in Medicine (ISMRM) meeting in Melbourne, Australia (May 5-11, 2012).
- 5) “Accelerated Four-Dimensional Echo-Planar J-Resolved Spectroscopic Imaging of Human Prostate: Prospective Non-Uniform Undersampling and Maximum Entropy Reconstruction.” was submitted and presented at the 54th Experimental Nuclear Magnetic Resonance (ENC), Asilomar, CA, Abstract #214, (April 14-19, 2013).
- 6) “Nonuniformly Under-Sampled (NUS) Echo Planar J-Resolved Spectroscopic Imaging (EP-JRESI) of Prostate Cancer Patients and Compressed Sensing Reconstruction” summarizing the implementation of the 4D EP-JRESI sequence and evaluation of it in the prostate cancer patients was presented at the 21st International Society of Magnetic Resonance in Medicine (ISMRM), Salt Lake, Utah, April 20-26, 2013, #3959.
- 7) “Accelerated Echo Planar J-Resolved Spectroscopic Imaging in Prostate Cancer: Nonlinear Reconstruction Using Total Variation And Maximum Entropy” 23rd International Society of Magnetic Resonance in Medicine (ISMRM), Milan, Italy, May 10-16, 2014 (oral presentation), #962.
- 8) “Maximum Entropy Reconstructed Echo Planar J-Resolved Spectroscopic Imaging and Diffusion Weighted Imaging in Prostate Cancer” 23rd International Society of Magnetic Resonance in Medicine (ISMRM), Milan, Italy, May 10-16, 2014 (eposter), # 4108.
- 9) “Compressed Sensing based Echo-planar 3D MRSI Using Short Echo Time: A Pilot Evaluation Using a Prostate Phantom” 23rd International Society of Magnetic Resonance in Medicine (ISMRM), Milan, Italy, May 10-16, 2014 (poster), # 1529
- 10) “Semi-Laser 5D Echo-Planar J-Resolved Spectroscopic Imaging: Pilot Validation in Prostate Cancer”. 23rd International Society of Magnetic Resonance in Medicine (ISMRM), Toronto, Canada, May 30-June 5, 2015, #2020.

- 11) “How Accurately Multiparametric MRI Detect Prostate Cancer?”, 23rd International Society of Magnetic Resonance in Medicine (ISMRM), Toronto, Canada, May 30-June 5, 2015 (eposter), # LL-PHE118.
- 12) “Prostate Cancer Detection Using Accelerated 5D EPJRESI - sLASER Combined With DWI”, 24th International Society of Magnetic Resonance in Medicine (ISMRM), Singapore, May 7-13, 2016, abstract#3558.
- 13) “Resolution Enhanced accelerated Four Dimensional Echo Planar Spectroscopic Imaging: Application in Prostate Cancer”, 25th ISMRM Annual Meeting, Honolulu, HI, April 22-27, 2017, accepted for short oral and ePoster presentations.

C. Books: Two book chapters including some prostate data were published in the following chapters:

- 1) Huda A, Nagarajan R, Furuyama J and Thomas MA. In Vivo Two-Dimensional Magnetic Resonance Spectroscopy "Comprehensive Biomedical Physics" Elsevier Publishers, 2014, Pp 359-77.
- 2) Thomas MA, Iqbal Z, Sarma MK, Nagarajan R, Macey PM, Huda AS. (2016). ‘Two-Dimensional NMR Spectroscopy Plus Spatial Encoding’ in *Handbook of Magnetic Resonance Spectroscopy In Vivo: MRS Theory, Practice and Applications*, Bottomley, P.A. and Griffiths, J.R. (eds). John Wiley & Sons Ltd, Chichester, UK, pp 495-520.

Conclusions: After successfully implementing the 4D EP-JRESI scanning protocol on the 3T MRI scanner and testing it in healthy controls and patients during the past five years, We have studied a total of 47 PCa patients (masses include both malignant and benign) and 9 healthy males. During this IDEA grant funded period (2012-2016), we have published a total of 7 peer-reviewed manuscripts, 13 conference abstracts and 2 book chapters that were also peer-reviewed.

References

- 1) Dall’era MA, Cooperberg MR, Chan JM, *et al.* Active surveillance for early-stage prostate cancer: review. *Cancer*. 2008 Apr 15;112(8):1650-9. **PMID: 18306379**
- 2) McNeal JE. Normal histology of the prostate. *Am J Surg Pathol* 1988;12:619-633. **PMID: 2456702**
- 3) Weinreb JC, Blume JD, Coakley FV, *et al.* Prostate cancer: sextant localization at MR imaging and MR spectroscopic imaging before prostatectomy--results of ACRIN prospective multi-institutional clinicopathologic study. *Radiology*. 2009 Apr;251(1):122-33. **PMID: 19332850**
- 4) Jacobs MA, Ouwerkerk R, Petrowski K and Macura KJ. Diffusion-weighted imaging with apparent diffusion coefficient mapping and spectroscopy in prostate cancer. *Top Magn Reson Imaging*. 2008;19:261-72 **PMID:19512848**
- 5) Scheenen TW, Heijmink SW, Roell SA, *et al.* Three-dimensional proton MR Spectroscopy of human prostate at 3T without endorectal coil: feasibility. *Radiology* 2007;245:507-16. **PMID: 17848681**
- 6) Thomas MA, Narayan P, Kurhanewicz J, Jajodia P, Weiner MW. 1H MR spectroscopy of normal and malignant human prostates in vivo. *J Magn Reson* 1990; 87:610–619. **PMID:N/A**

- 7) Thomas MA, Narayan P, Kurhanewicz J, *et al.* Detection of phosphorus metabolites in human prostates with a transrectal ^{31}P NMR probe. *J Magn Reson* 1992; 99: 377-386. **PMID: N/A**
- 8) Narayan P, Kurhanewicz J. Magnetic Resonance spectroscopy in prostate disease: diagnostic possibilities and future developments. *Prostate* 1992; Suppl 4: 43-50. **PMID: 1374177**
- 9) van der Graaf M, Schipper RG, Oosterhof GO, J.A. Schalken, AA. Proton MR spectroscopy of prostatic tissue focused on the detection of spermine, a possible biomarker of malignant behavior in prostate cancer. *MAGMA* 2000; 10(3):153-9. **PMID: 10873205**
- 10) Jordan KW and Cheng LL. NMR-based metabolomics approach to target biomarkers for human prostate cancer. *Expert Rev Proteomics* 2007;4:389-400. **PMID: 17552923**
- 11) Kurhanewicz J, Swanson MG, Nelson SJ, and Vigneron DB. Combined magnetic resonance imaging and spectroscopic imaging approach to molecular imaging of prostate cancer. *J Magn Reson Imaging* 2002;16(4):451-463. **PMID: 12353259**
- 12) Mansfield P. Spatial mapping of the chemical shift in NMR. *Magn Reson Med* 1984; 1: 370 – 386. PMID:6571566
- 13) Posse S, Otazo R, Caprihan A, et al. Proton echo-planar spectroscopic imaging of J-coupled resonances in human brain at 3 and 4 Tesla. *Magn Reson Med* 2007; 58(2): 236-44. PMID: 17610279
- 14) Schulte RF and Boesiger P. ProFit: two-dimensional prior-knowledge fitting of J-resolved spectra. *NMR Biomed* 2006;19:255-263. **PMID: 16541464**
- 15) Lange T, Schulte RF and Boesiger P. Quantitative J-resolved prostate spectroscopy using two-dimensional prior-knowledge fitting. *Magn Reson Med* 2008;59:966-972. PMID: 18429013
- 16) Thomas MA, Lange T, Velan SS, et al. Two-dimensional MR Spectroscopy of healthy and cancerous prostates in vivo. *Magn Reson Mater Phy (MAGMA)* 2008;21(6):443-58. **PMID: 18633659**
- 17) Wright A, Tessem MB, Bertilsson H, et al. Quantitative ^1H HR-MAS using LC Model shows glutamate, choline, glycerylphosphocholine, and glucose as biomarkers of prostate. *Proc Intl Soc Magn Reson Med* 2012;20:2975. **PMID: N/A**
- 18) Stenman K, Hauksson JB, Grobner G, et al. Detection of polyunsaturated omega-6 fatty acid in human malignant prostate tissue by 1D and 2D high resolution magic angle spinning NMR spectroscopy. *MAGMA* 2009;22:327-31 **PMID: 19921294.**

Appendix:

1. Furuyama J, Wilson NE, Burns BL, et al. Application of Compressed Sensing to Multidimensional MR Spectroscopic Imaging in Human Prostate. *Magn Reson Med* 2012;67:1499-1505.
2. Nagarajan R, Iqbal Z, Burns B, et al. Accelerated echoplanar J-resolved spectroscopic imaging in prostate cancer: a pilot validation of non-linear reconstruction using total variation and maximum entropy. *NMR Biomed.* 2015 Nov;28(11):1366-73.
3. Thomas MA, Iqbal Z, Sarma MK, Nagarajan R, Macey PM, Huda AS. (2016). 'Two-Dimensional NMR Spectroscopy Plus Spatial Encoding' in *Handbook of Magnetic Resonance Spectroscopy In Vivo: MRS Theory, Practice and Applications*, Bottomley, P.A. and Griffiths, J.R. (eds). John Wiley & Sons Ltd, Chichester, UK, pp 495-520.
4. Nagarajan R, Iqbal Z, Wilson N, et al. Prostate Cancer Detection Using Accelerated 5D EPJRESI - sLASER Combined With DWI, 24th International Society of Magnetic Resonance in Medicine (ISMRM), Singapore, May 7-13, 2016, abstract#3558.
5. Iqbal Z, Burns BL, Nagarajan R, et al. Resolution Enhanced accelerated Four Dimensional Echo Planar Spectroscopic Imaging: Application in Prostate Cancer", 25th ISMRM Annual Meeting, Honolulu, HI, April 22-27, 2017 (accepted for a short oral as well as an ePoster presentations).

Application of Compressed Sensing to Multidimensional Spectroscopic Imaging in Human Prostate

Jon K. Furuyama, Neil E. Wilson, Brian L. Burns, Rajakumar Nagarajan, Daniel J. Margolis, and M. Albert Thomas*

The application of compressed sensing is demonstrated in a recently implemented four-dimensional echo-planar based J-resolved spectroscopic imaging sequence combining two spatial and two spectral dimensions. The echo-planar readout simultaneously acquires one spectral and one spatial dimension. Therefore, the compressed sensing undersampling is performed along the indirectly acquired spatial and spectral dimensions, and the reconstruction is performed using the split Bregman algorithm, an efficient TV-minimization solver. The four-dimensional echo-planar-based J-resolved spectroscopic imaging data acquired in a prostate phantom containing metabolites at physiological concentrations are accurately reconstructed with as little as 20% of the original data. Experimental data acquired in six healthy prostates using the external body matrix “receive” coil on a 3T magnetic resonance imaging scanner are reconstructed with acquisitions using only 25% of the Nyquist–Shannon required amount of data, indicating the potential for a 4-fold acceleration factor in vivo, bringing the required scan time for multidimensional magnetic resonance spectroscopic imaging within clinical feasibility. Magn Reson Med 67:1499–1505, 2012. © 2012 Wiley Periodicals, Inc.

Key words: Compressed sensing; prostate; magnetic resonance; citrate; echo-planar J-resolved spectroscopic imaging

Magnetic resonance spectroscopy and magnetic resonance spectroscopic imaging have evolved as powerful research tools for their ability to study the underlying biochemistry of tissue (1) and can greatly complement standard magnetic resonance imaging (MRI). One of the major drawbacks of one-dimensional (1D) spectroscopy is the inherent overcrowding of spectra due to overlapping peaks. This limitation can be alleviated with the addition of more spectral dimensions by which resonances can be spread apart, increasing the spectral dispersion (2). Different two-dimensional (2D) spectroscopic techniques have been successfully used in vivo such as J-resolved spectroscopy (3) and localized correlated spectroscopy (4). However, these were originally limited to single voxel acquisitions. To increase the spatial coverage, the localized correlated

spectroscopy and J-resolved spectroscopy sequences were recently modified with an echo-planar spectroscopic imaging (EPSI) (5–7) readout to yield 2D spectra from multiple voxels in a single experiment, called echo-planar correlated spectroscopic imaging (8) and echo-planar J-resolved spectroscopic imaging (EP-JRESI) (9), respectively. Despite the rapid acquisition of EPSI, such four-dimensional (4D) scans still require a considerable amount of scan time (~20–40 mins/average depending on the desired spatial/spectral resolution), severely limiting clinical applicability.

In recent years, the field of compressed sensing (CS) has garnered much interest in the imaging community for its ability to reconstruct images from datasets whose sampling does not meet the Nyquist–Shannon criterion (10,11). CS operates under the assumption that the fully sampled data is sparse within some transform domain. The CS reconstruction attempts to enforce this assumption in that particular transform domain, while maintaining fidelity with the acquired measurements. Since the application of CS in MRI was demonstrated (12,13), there has been a trove of proposed applications for imaging studies as well as high resolution nuclear magnetic resonance, many of which hold the potential to reduce scan times by a factor of 2–8 times (14–18).

Despite the many potential applications in standard MRI, there have not been many proposed implementations for use in magnetic resonance spectroscopic imaging (19). Part of the reason is that while CS can provide acceleration factors ranging from 2 to 8 times in standard chemical shift imaging with multiple phase encoding directions, the acceleration factor of using an EPSI readout is on the order of 16–32. The challenge is thus to further accelerate EPSI with CS. Since EPSI simultaneously reads out one spatial and one spectral dimension, there remains only one dimension that can be undersampled in a 2D spatial acquisition. However, it has been previously discussed that CS can perform better when the undersampling is spread across multiple dimensions (20). Hu et al. employed pseudo-random phase-encoding blips during the EPSI readout to create nonuniform sampling along the spatial as well as spectral dimensions for use in hyperpolarized ^{13}C spectroscopic imaging (19).

In the EP-JRESI sequence, the EPSI readout simultaneously acquires one spatially encoded dimension (k_x) and one temporal dimension (t_2), leaving the remaining spatial and spectral dimensions (k_y and t_1 , respectively) to be incrementally collected. We propose the use of nonuniform undersampling (NUS) in the remaining $k_y t_1$ plane, using CS to reconstruct the equivalent missing data to a fully sampled 4D EP-JRESI acquisition. Despite the mixing

Department of Radiological Sciences, University of California, Los Angeles, California, USA

Grant sponsor: IDEA (US Army Department of Defense); Grant sponsor: Prostate Cancer Research Program (PCRP); Grant number: W81XWH-11-1-0248

*Correspondence to: M. Albert Thomas, Ph.D., Department of Radiological Sciences, University of California, Los Angeles, CA 90095. E-mail: AThomas@mednet.ucla.edu

Received 23 November 2011; revised 27 February 2012; accepted 28 February 2012.

DOI 10.1002/mrm.24265

Published online 13 April 2012 in Wiley Online Library (wileyonlinelibrary.com).

of spatial and spectral dimensions in the reconstruction, the sparsity requirement for reconstruction is shown to still be satisfied, as required by CS. Since the $k_y t_1$ plane is incrementally acquired, NUS can be trivially applied to the sequence without pseudo-random gradient blips.

Using fully sampled prostate phantom datasets, the NUS can be simulated and the data can be reconstructed using publicly available ℓ_1 -norm minimization algorithms. We show that the CS reconstruction performs favorably with as little as 20–25% of the original data, implying an acceleration factor of 4–5 times and scan times less than 4–5 mins for the NUS 4D EP-JRESI sequence. Nonuniformly undersampled data were collected in the prostate of healthy volunteers amounting to 25% of the sampling required by the Nyquist–Shannon criterion. The reconstructed NUS data shows good spatial and spectral quality in the undersampled dimensions, comparable to the fully sampled reconstruction.

THEORY

In order for CS to be successfully applied, the following criteria must be satisfied. First, the data must have a sparse representation: namely, there must exist some transform domain in which the data has many coefficients that are zero or nearly zero. Second, the NUS must be such that it produces incoherent aliasing artifacts within the transform domain, which is easily obtained by sampling the dataset at random. With these conditions, the fully sampled dataset can be recovered using nonlinear reconstruction algorithms that attempt to enforce the sparsity while simultaneously maintaining the fidelity of the original measurements to within the noise. CS solves the constrained optimization problem (12)

$$\min_m \|\Psi m\|_1 \quad \text{s.t.} \|\mathcal{F}_u m - y\|_2^2 < \epsilon^2 \quad [1]$$

where Ψ is the transform operator in which the reconstructed data, m , is sparse, \mathcal{F}_u is the undersampled Fourier transform, y is the sampled data, ϵ is a fidelity factor, and $\|x\|_n$ is the ℓ_n norm: $\|x\|_n = (\sum_i |x_i|^n)^{1/n}$, for $n > 0$. The minimization of the ℓ_1 -norm in Eq. 1 promotes sparsity by trying to reduce the number of nonzero coefficients as much as possible. The ℓ_1 -norm objective function is offset by the ℓ_2 -norm constraint that the reconstruction remains consistent with the measured data within the tolerance, ϵ .

In MRI, wavelets have been the popular transform domain in which the ℓ_1 -norm is minimized. However, in this work, the data is undersampled in the $k_y t_1$ plane in which the wavelet transform may not necessarily be as optimal as in MRI. As described by Lustig et al., minimizing finite differences ($\Psi = \nabla$), or total variation (TV), can also be used alongside the wavelet transform as a form of smoothing the data (12). Other work has shown that minimizing TV alone is sufficient to adequately reconstruct undersampled datasets (13,21,22). Here, we use TV exclusively to sparsify the data.

The constrained problem in Eq. 1 can alternatively be written as an unconstrained problem

$$\min_m \|\nabla_{y,F_1} m\|_1 + \frac{\lambda}{2} \|\mathcal{F}_u m - y\|_2^2 \quad [2]$$

where λ is a regularization parameter that weighs the sparsity against the data consistency, $m = S(x, y, F_1, F_2)$ is the final dataset, \mathcal{F}_u is applied only along the y and F_1 dimensions, $y = s(x, k_y, t_1, F_2)$ is the sampled data, and ∇_{y,F_1} is the gradient in the yF_1 plane.

In a fully sampled EP-JRESI sequence, the final 4D dataset, $S(x, y, F_1, F_2) = \mathcal{F}\{s(k_x, k_y, t_1, t_2)\}$, is composed of two spatial and two spectral dimensions. The simplest way to visualize the data is to consider that for every point in the xy spatial plane (voxel), there is a 2D J -resolved spectrum (F_1, F_2). An example of this is shown in Fig. 1a,b. Experimentally, the data is collected such that the entire $k_x t_2$ plane is acquired during a single EPSI readout for a given (k_y, t_1) point. Nonuniformly undersampling the $k_y t_1$ plane will result in incoherent aliasing in the yF_1 plane following Fourier transform. Figure 1c shows the yF_1 plane for the choline peak at 3.2 ppm (dotted line in 1B) for a given point along the x -direction (dotted line in 1A). Figure 1c also shows the finite differences along the y and F_1 dimensions. While it can be seen that the yF_1 plane appears sparse within the identity domain ($\Psi = \mathbb{1}$), it can be seen that $\|\nabla m\|_1 < \|\mathbb{1}m\|_1$, as sought out by Eq. 1, and thus minimizing the finite differences are well suited for CS reconstruction. The optimal sparsifying transform for a given application is not yet known and is the subject of ongoing research (23).

METHODS

Phantom

To determine the feasibility as well as evaluate the performance of the CS reconstruction, numerous retrospective undersampling and reconstructions were performed on a fully sampled prostate EP-JRESI phantom dataset. A 500 mL prostate phantom was prepared containing the following metabolites at physiological concentrations as reported in healthy human prostate (24,25): citrate (Cit, 50 mM), creatine (Cr, 5 mM), choline (Cho, 1 mM), spermine (Spm, 6 mM), myo-inositol (mI, 10 mM), phosphocholine (PCh, 2 mM), taurine (Tau, 3 mM), glutamate (Glu, 4 mM), glutamine (Gln, 2.5 mM) and scyllo-inositol (Scy, 0.8 mM). The dataset was localized with a field of view (FOV) of $16 \times 16 \text{ cm}^2$ on a 16×16 grid with a slice thickness of 2 cm for an individual voxel volume of 2 cm^3 ; 512 bipolar gradient echo pairs (t_2 samples) were collected with a repeat time of 0.84 ms and $100t_1$ increments with $\Delta t_1 = 1 \text{ ms}$ resulting in F_1 and F_2 bandwidths of 1000 Hz and 1190 Hz, respectively. With pulse repetition time/echo time = 1500/30 ms and one average, the EP-JRESI phantom scan duration was 40 mins. Water suppression was performed using the WET sequence (26) just before PRESS localization (27). To correct for eddy-currents generated by the EPSI readout, a nonwater-suppressed scan was acquired as a reference (28).

The NUS was simulated by zeroing data points in the fully sampled $k_y t_1$ plane according to the exponentially decaying sampling density

$$\rho(k_y, t_1) = \exp \left\{ -\frac{|k_y|}{a} - \frac{t_1}{b} \right\} \quad [3]$$

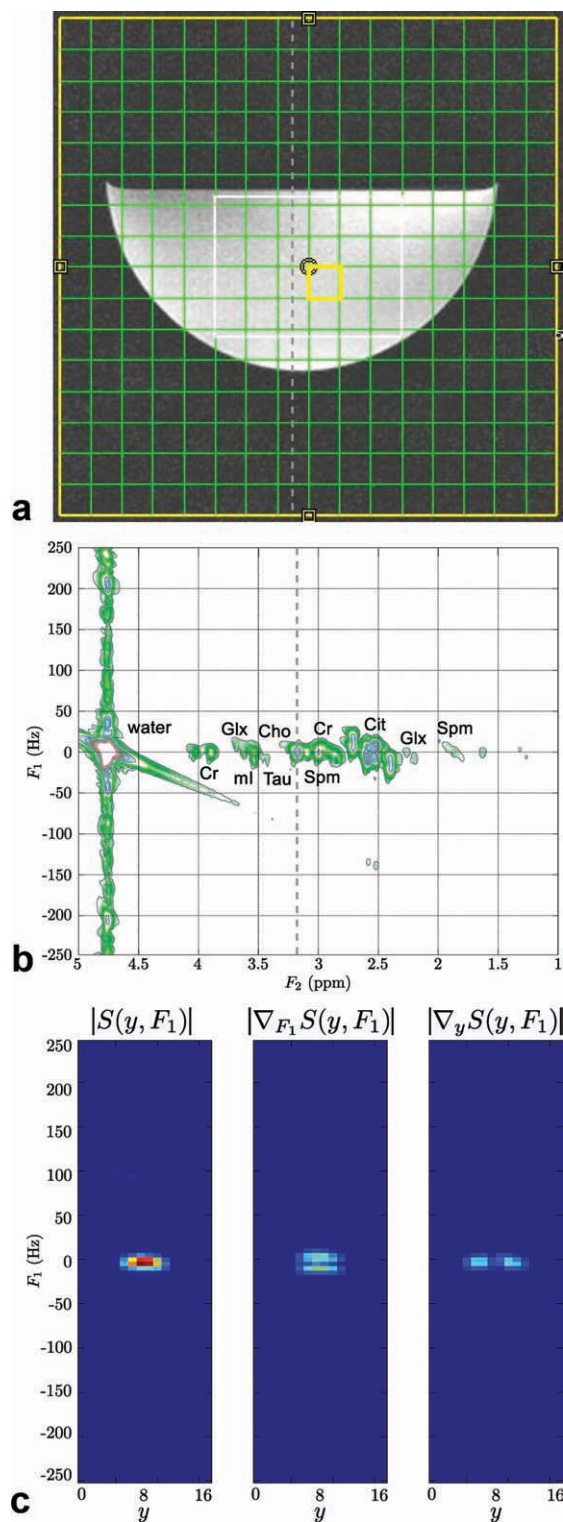


FIG. 1. **a:** T_1 -weighted axial MRI of a prostate phantom where the white box indicates the PRESS localized volume. **b:** 2D J -resolved spectrum from the center voxel (yellow box in **a**) of the prostate phantom. **c:** Demonstration of the sparsity of the undersampled yF_1 plane, $S(y, F_1)$, for a given x and F_2 point as indicated by the dotted lines in **(a)** and **(b)** as well as the finite differences of the same plane, $\nabla_{y, F_1} S(y, F_1)$.

where $\rho(k_y, t_1)$ is the probability a data point is sampled, $-k_{y, \max} \leq k_y \leq k_{y, \max}$, $0 \leq t_1 \leq t_{1, \max}$, and a and b are flexible parameters that determine the percentage of data that is sampled. The signal in the indirect t_1 dimension has an exponential decay envelope determined by T_2 -weighting and the center of k -space has the highest signal intensity. Therefore, Eq. 3 ensures that the regions in the $k_y t_1$ plane with the greatest signal-to-noise ratio (SNR) are collected. Different trials were conducted for NUS, keeping 50%, 33%, 25%, 20%, 16%, and 10% of the original phantom data, corresponding to acceleration factors from 2 to 10 times. For each simulation, a different mask was randomly generated with $a = b$ such that the degree of undersampling was distributed equally between the k_y and t_1 dimensions.

In Vivo

The performance of the reconstruction algorithm was tested in vivo by collecting undersampled data in the prostate of 6 healthy volunteers (age range 25-57 years old) using a body matrix “receive assembly” on a Siemens 3T Trio-TIM MRI scanner (Siemens Medical Solutions, Erlangen, Germany) running the VB17a platform. The FOV was a $16 \times 16 \text{ cm}^2$ area localized onto a 16×16 grid with slice thickness of 2 cm, for an individual voxel volume of 2 cm^3 . The usual fully sampled data consists of 64 t_1 increments. The scanner was programmed to collect only 25% of the fully sampled data matrix according to the sampling density in Eq. 3. Points that were not collected were set to zero. Two averages were acquired for a total scan duration of 12 min 48 s. A nonwater-suppressed scan was also acquired as a reference scan for eddy-current correction and coil combination purposes by fully sampling k_y with only the first t_1 increment, adding 30 s to the total scan duration.

Reconstruction

All data reconstructions were performed by solving Eq. 2 using the split Bregman iterative method (29) with $\lambda = 1$ such that the data fidelity is weighed equally against the minimization of the finite differences. The algorithm was iterated until $\nabla_{y, F_1} m$ was minimized while maintaining a normalized error of no greater than 1 part per million (ppm), namely $\|\mathcal{F}_u m - y\|_2^2 < 1 \times 10^{-6}$. While the reconstruction was performed on the entire dataset, the TV operator, ∇_{y, F_1} , only acted on data in the undersampled $k_y t_1$ plane. The entire 4D reconstruction required roughly 30 mins/channel on a standard desktop PC.

For both phantom and in vivo scans, we have used the maximum-echo sampling method as reported by Schulte et al. (30). This yields a spectrum with a COSY-like diagonal where the J -resolved peaks are centered around the diagonal. Each t_1 row was time-shifted during postprocessing such that the diagonal is rotated 45° , having the appearance of a conventional 2D J -resolved spectrum (31) with an F_1 bandwidth of $\pm 250 \text{ Hz}$.

For the phantom, the CS reconstruction was applied to a processed fully-sampled dataset that had NUS imposed retrospectively. However, for the in vivo scan more steps were required since the raw metabolite data itself was undersampled. A nonwater-suppressed scan was collected to correct for eddy current distortions and to serve as

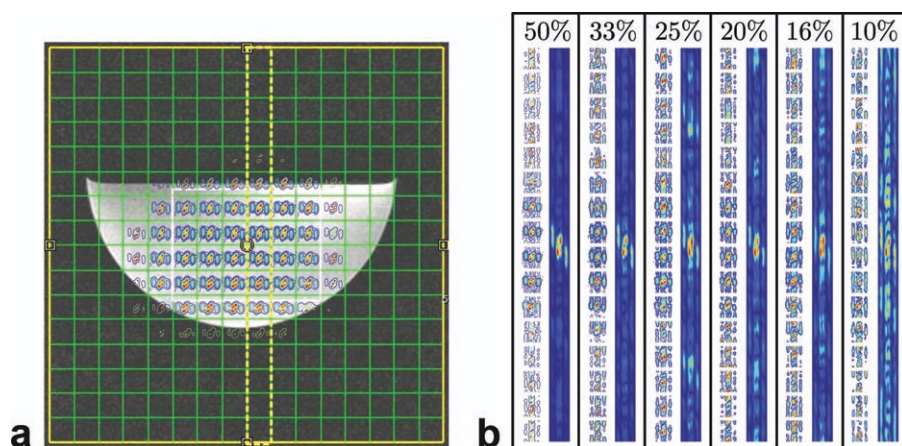


FIG. 2. **a**: Spatial distribution of the fully sampled J -resolved citrate multiplet at 2.6 ppm on the T_1 -weighted axial MRI. **b**: The effect of the incoherent aliasing along both the y -direction as well as the F_1 -dimension as a function of the percentage of the nonuniformly sampled data. For each amount of kept data, the column along the y -direction for a given point along x (left column) is marked by the dotted yellow box in (a), and the F_1 column (right column) is centered around the citrate multiplet at $F_2 = 2.6$ ppm.

a reference for coil combination. The 4D reconstruction was performed on the raw metabolite data for each channel individually, followed by eddy-current correction and coil combination. For a quantitative comparison of the in vivo data, the Creatine+Spermine+Choline to Citrate ratio, $(Cr+Spm+Cho)/Cit$, can be measured by calculating the volume integrals of the diagonal and cross peaks between 2.9 and 3.3 ppm for Cr+Spm+Cho, and between 2.4 and 2.8 ppm for Cit.

RESULTS

Phantom

There are many ways to view the 4D dataset. One simple way is to view each 2D voxel as containing an individual 2D spectra. Although intuitive, it can be cumbersome to view all spectra at once, in the case of a 16×16 imaging grid there are 256 different spectra. For simplicity, a chosen peak can be overlaid on top of a localization image to show the spatial distribution of that peak, as shown with the strongly coupled (AB) citrate multiplet (32,33) (centered at $F_2 = 2.6$ ppm) in Fig. 2a. Although there seems to be some leakage from the point spread function as well as chemical shift artifacts, the peaks with the brightest intensity appear within the PRESS excitation volume marked by the white box.

The effect of NUS leads to incoherent aliasing as shown in Fig. 2b with data that has been filled simply using zeros. To simplify viewing the data, one column (marked by the dotted yellow box in 2a) was selected to display the incoherent aliasing along the y -direction, and one region centered around the citrate multiplet (centered at $F_2 = 2.6$ ppm) is shown to display the incoherent aliasing in the F_1 dimension. For 50% of the data, there is noticeable leakage of the citrate multiplet in the y -direction. The peaks from the fully sampled data shown in 2a are better resolved than the under-sampled peaks in Fig. 2b (first column in each pair) and still maintain the same shape across the PRESS excitation volume. The same can be said along the F_1 dimension where signal leakage is taking place due to the NUS in Fig. 2b (second column in each pair). As the number of sampled points is reduced, the degree of incoherent aliasing along both the y and F_1 dimensions increases. At 16%, most of the original shape has been

heavily degraded as the signal now appears to be incoherently smeared across both y and F_1 dimensions. By 10%, there is little resemblance to the original dataset.

The CS reconstruction of the undersampled phantom datasets along with the normalized root mean square error (RMSE), calculated with respect to the fully sampled data, is shown in Fig. 3. The same column and citrate region in Fig. 2 are displayed in 3a. It can be seen visually and from the low RMSE values that the CS reconstruction successfully cleans up the incoherent aliasing produced by the NUS when Figs. 2 and 3 are compared. For as little as 20% of the original sample points, the spatial reconstruction of the citrate multiplet is very close to the original fully sampled data (yellow box in Fig. 2a). At 16% of the original data, it can be seen that while the spatial distribution along the y -direction is still consistent with the fully sampled data, the shape of the peaks starts to deviate slightly. The same can be seen for the reconstruction of the F_1 dimension where the algorithm performs well in removing the incoherent aliasing. Again, at 16% of the original sample points, there begins to be slight deviations in the shape of the peak (reflected by the notably higher RMSE) when compared to datasets with higher percentages of the original sample points. At 10% of the data, it can be seen that while a lot of the incoherent aliasing has been removed, the final reconstruction has noticeable visual deviations from the original dataset, along with an RMSE above 1%.

Figure 3b is CS reconstructed spectra from only 20% of the original data, taken from the same location as the example spectra in Fig. 1b. While there are slight differences in noise and contour levels, the same basic features present in the fully sampled spectra are clearly visible in the reconstructed spectra. In particular is the faithful reproduction of the citrate multiplet in which the J -resolved peaks are nicely resolved.

In Vivo

Figure 4 shows the results of the CS reconstruction of an undersampled in vivo scan of a 29-year-old healthy prostate. The mask that was used to sample 25% of the $k_y t_1$ plane is shown in Fig. 4. The spatial distribution of the J -resolved citrate multiplet at 2.6 ppm is shown in Fig. 4b. As in the phantom, the peaks are localized within the PRESS excitation volume (white box) with some slight leakage

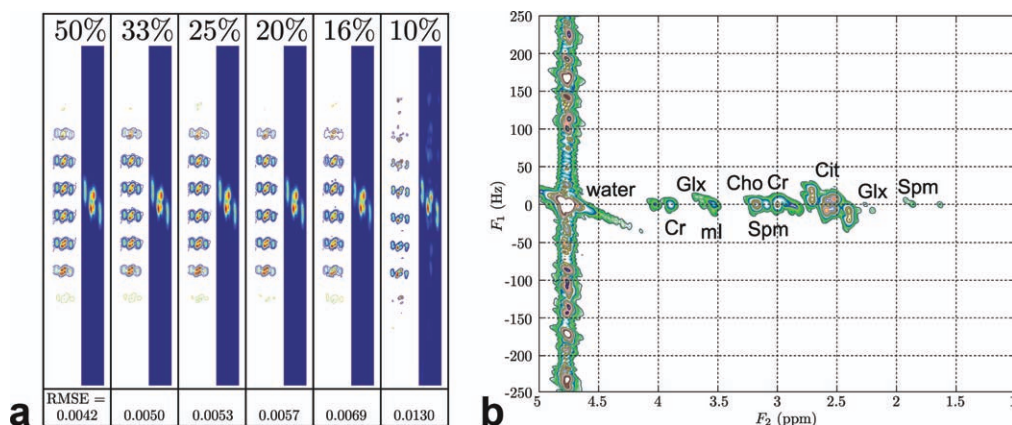


FIG. 3. **a**: Reconstructions of the retrospectively undersampled datasets shown in Fig. 2. The same columns in Fig. 2 are displayed to show the effect of the reconstruction algorithms along with the normalized RMSE values. **b**: A reconstructed spectrum from the same voxel in Fig. 1b with only 20% of the original data from the same voxel as the sample spectrum in Fig. 1b and contains the same annotated metabolites.

due to the point spread function as well as chemical shift artifacts. An individual J -resolved spectrum from a select 2 cm^3 voxel is shown in Fig. 4c. The extracted spectra have considerably more noise than the phantom scans, but the main metabolites, citrate, creatine, spermine, choline, etc. can be detected. For the spectrum shown in Fig. 4b, the $(\text{Cr}+\text{Spm}+\text{Cho})/\text{Cit}$ was calculated to be 0.395. The mean $(\text{Cr}+\text{Spm}+\text{Cho})/\text{Cit}$ value for all six volunteers from a similar location was measured to be 0.451 with a coefficient of variance of 19%, and is consistent with what has been reported in the literature (34,35). To demonstrate the reproducibility between all the scans, the reconstructed citrate multiplet from the left peripheral zone of each volunteer is shown in Fig. 5.

DISCUSSION

The application of CS requires that the fully sampled dataset be sparse in some transform domain and that the NUS pattern be such that any aliasing be incoherent. Since the undersampling performed in the $k_y t_1$ plane of the 4D

EP-JRESI data was shown in Fig. 1c to have a sparse representation using finite differences, it is suitable to use TV minimization in the CS reconstruction. By randomly sampling in the $k_y t_1$ plane according to a probability density (Eq. 3), the data yielded incoherent artifacts that spread across each NUS dimension as seen in Fig. 2b. The incoherent artifacts have the appearance of noisy data and get progressively worse as fewer samples are used in the reconstruction. While the incoherent artifacts are not technically “noise” in the conventional sense in that they are not random, they may be removed by “de-noising” algorithms. Total variation has previously been used as a method for noise removal in images (36) and thus serves as a suitable objective function for the CS reconstruction. The reconstruction can be seen to act as a smoothing algorithm that effectively “de-noises” the data so long as it is consistent with the collected data. Such data-consistent denoising effectively fills in the missing data-points while maintaining the fidelity of the originally sampled data.

As can be seen in Fig. 3, the CS reconstruction successfully cleans up the incoherent artifacts for undersampled

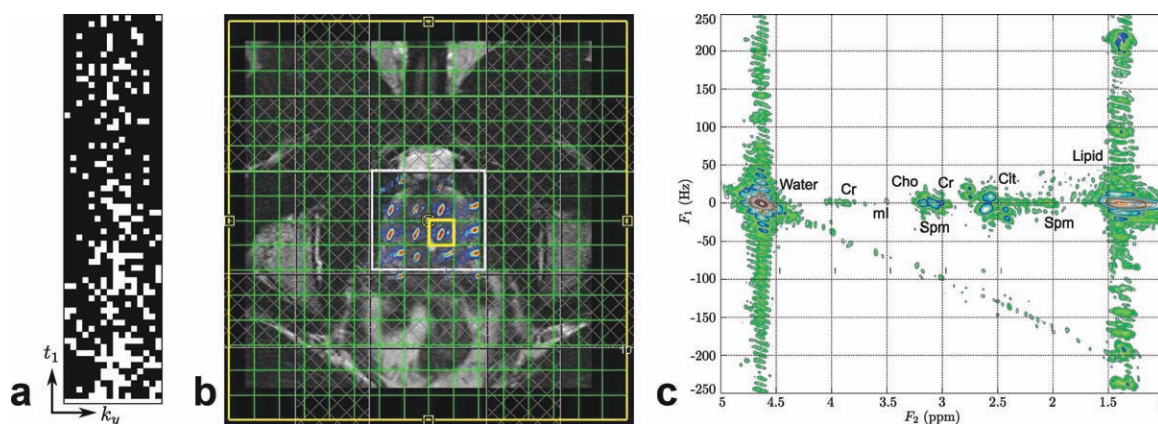


FIG. 4. Reconstruction of an undersampled 4D EP-JRESI in vivo prostate scan with only 25% of the samples as required by the Nyquist-Shannon criterion showing (a) the mask used to undersample the $k_y t_1$ plane where the white points indicate those that were sampled, (b) the multivoxel spatial distribution of the citrate multiplet at 2.6 ppm overlaid on top of the T_2 -weighted axial MRI with the white box indicating the PRESS localization, and (c) a J -resolved spectrum from a select voxel in the reconstruction.

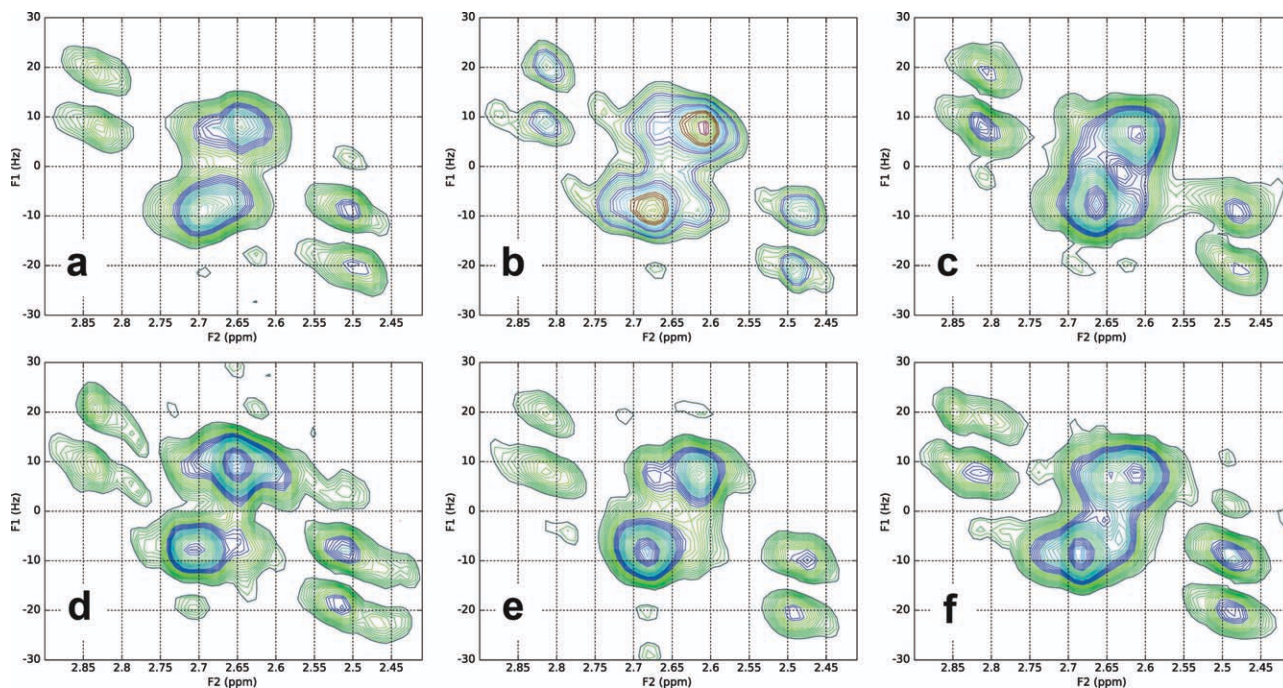


FIG. 5. **a-f**: Expanded view of the citrate multiplet from a select voxel in the left peripheral zone from each of the six healthy male volunteers.

data. For the undersampled data containing more than 20% of the fully sampled data, the reconstruction produces a high fidelity reproduction of the original data, with RMSE values all below 0.6%. The performance of the reconstruction algorithm begins to degrade with fewer sample points, in this case, once the data drops below 20%. Despite the performance drop, it is still remarkable to see that even at 10% of the data, the CS reconstruction does a decent job of cleaning up the incoherent artifacts, with an RMSE of 1.3%, resulting in a yF_1 profile that is similar to the original fully sampled data. This observation can be useful if a high-fidelity reconstruction is not required, and the data can be undersampled to a higher degree to save time. As expected, the RMSE values increase with the acceleration factor demonstrating the tradeoff between acceleration and accuracy of the reconstruction.

The undersampled in vivo results demonstrate the feasibility in reducing scan times in multidimensional spectroscopic imaging sequences by means of nonuniformly sampling the $k_y t_1$ plane and CS reconstruction. While collecting only 25% of the data results in an acceleration factor of 4, two averages were acquired for SNR purposes, thus resulting in only a 2-fold acceleration. Alternatively, collecting 50% of the data with only 1 average would result in the same acceleration factor as well as the same SNR. However, without sufficient SNR, many of the lower concentration metabolites run the risk of being de-noised, or wiped out completely by the reconstruction, as the data fidelity term in the objective function allows for the modification of features on the order of the noise-level. Since the phantom reconstruction with 25% of the data was comparable to the reconstruction with 50% of the data, only 25% of the in vivo data was collected with two averages in an attempt to boost the SNR of the metabolites with lower sensitivity. The minimum SNR for reconstruction, which

depends on the overall sparsity of a particular signal as well as the extent of the incoherent aliasing is an ongoing field of research and will be the subject of future work (37). Given improved sensitivity (such as better shimming, more sensitive coils, and/or higher B_0), the SNR would be sufficient without having to average, yielding a full acceleration factor of 4.

As the 4D in vivo dataset was actually undersampled during the scan, there is no direct means to compare with a fully sampled dataset as was the case with the reconstructions on the phantom dataset. The reconstructed in vivo spectra and profiles recorded in the 6 healthy controls show similar quality to previously reported fully sampled EP-JRESI spectra acquired in the prostate of healthy volunteers (9). The citrate multiplet is well reconstructed showing a nicely J -resolved AB-type structure. The other major metabolites are visible as well, in which their calculated ratios are in agreement with the literature and consistent throughout all the volunteer scans.

This pilot study made use of randomly generated sampling masks according to Eq. 3 to selectively delete points in the fully sampled dataset to simulate undersampling. The same type of randomly generated sampling mask was used on the MRI scanner to collect an undersampled in vivo dataset. While this technique satisfies the incoherent aliasing criterion in CS, it is not necessarily the optimal sampling scheme. Not all sampled points have equal contribution to the overall structure of the data, and it can be seen that the collection of certain points can be more critical than other points. That is not to say that certain points are unimportant, but rather the collection of certain key points can be critical such as the point at $k_y = 0$ and $t_1 = 0$. Likewise, it is possible that for some applications, one of the dimensions in the yF_1 plane may be more sparse than the other, and so the values for a and b (which were

set to be equal in this study) can be adjusted accordingly. This may be an even larger concern for the echo-planar correlated spectroscopic imaging sequence since the cross peak signals have a J -dependent maximum intensity in the t_1 dimension and thus cannot be modeled as simple decaying exponentials like in Eq. 3. As a result, determining the optimal sampling masks for both EP-JRESI as well as echo-planar correlated spectroscopic imaging is the subject of further investigation and will be reported elsewhere.

CONCLUSION

In the acquisition of a 4D spectroscopic imaging sequence (2D spatial, 2D spectral), an EPSI readout can be used to simultaneously accelerate the collection of one spatial and one spectral dimension. This is the first in vivo study to show that CS can be used to simultaneously accelerate the acquisition of the remaining spatial and spectral dimensions. Two techniques have thus been combined, both of which simultaneously accelerate the collection of one spatial and one spectral dimension. Such acceleration has the potential to bring 4D spectroscopic imaging (2D spatial and 2D spectral) scan times well under the coveted 10 min barrier, allowing for the power of 2D in vivo MRS to become a clinical reality.

REFERENCES

- Negendank W. Studies of human tumors by MRS: a Review. *NMR Biomed* 1992;5:303–324.
- Aue W, Bartholdi E, Ernst R. Two-dimensional spectroscopy. Application to nuclear magnetic resonance. *J Chem Phys* 1976;64:2229–2246.
- Ryner L, Sorenson J, Thomas M. Localized 2D J-resolved 1H MR spectroscopy: strong coupling effects in vitro and in vivo. *Magn Reson Imag* 1995;13:853–869.
- Thomas M, Yue K, Binesh N, Davanzo P, Kumar A, Siegel B, Frye M, Curran J, Lufkin R, Martin P, Guze B. Localized two-dimensional shift correlated MR spectroscopy of human brain. *Magn Reson Med* 2001;46:58–67.
- Mansfield P. Spatial mapping of the chemical shift in NMR. *J Phys D Appl Phys* 1983;16:L235–L238.
- Posse S, DeCarli C, Le-Bihan D. 3D echo planar spectroscopic imaging at short echo times in human brain. *Radiology* 1994;192:733–738.
- Mulkern R, Panych L. Echo planar spectroscopic imaging. *Concepts Magn Reson* 2001;13:213–237.
- Lipnick S, Verma G, Ramadan S, Furuyama J, Thomas M. Echo planar correlated spectroscopic imaging: implementation and pilot evaluation in human calf in vivo. *Magn Reson Med* 2010;64:947–956.
- Nagarajan R, Furuyama J, Margolis D, Raman S, Sarma M, Thomas M. Echo Planar Based J resolved and correlated spectroscopic imaging of Human Prostate Using External Coil. In: *Proceedings of the ISMRM, Montreal, Canada, 2011*. p 2801.
- Candés E, Romberg J, Tao T. Robust uncertainty principles: exact signal reconstruction from highly incomplete frequency information. *IEEE Trans Inf Theory* 2006;52:489–509.
- Donoho D. Compressed sensing. *IEEE Trans Inf Theory* 2006;52:1289–1306.
- Lustig M, Donoho D, Pauly J. Sparse MRI: the application of compressed sensing for rapid MR imaging. *Magn Reson Med* 2007;58:1182–1195.
- Block K, Uecker M, Frahm J. Undersampled radial MRI with multiple coils. Iterative image reconstruction using a total variation constraint. *Magn Reson Med* 2007;57:1086–1098.
- Drori I. Fast L1 minimization by iterative thresholding for multidimensional NMR spectroscopy. *J Adv Signal Proc* 2007;1:1–10.
- Gamper U, Boesiger P, Kozerke S. Compressed sensing in dynamic MRI. *Magn Reson Med* 2008;59:365–373.
- Kim Y, Narayanan S, Nayak K. Accelerated three-dimensional upper airway MRI using compressed sensing. *Magn Reson Med* 2009;61:1434–1440.
- Liang D, Liu B, Wang J, Ying L. Accelerating SENSE using compressed sensing. *Magn Reson Med* 2009;62:1574–1584.
- Otazo R, Kim D, Axel L, Sodickson D. Combination of compressed sensing and parallel imaging for highly accelerated first-pass cardiac perfusion MRI. *Magn Reson Med* 2010;64:767–776.
- Hu S, Lustig M, Chen A, Crane J, Kerr A, Kelley D, Hurd R, Kurhanewicz J, Nelson S, Pauly J, Vigneron D. Compressed sensing for resolution enhancement of hyperpolarized 13C flyback 3D-MRSI. *J Magn Reson* 2008;192:258–264.
- Lustig M, Donoho D, Santos J, Pauly J. Compressed sensing MRI. *IEEE Signal Process Magn* 2008;25:72–82.
- Huang F, Chen Y, Yin W, Lin W, Ye X, Guo W, Reykowski A. A rapid and robust numerical algorithm for sensitivity encoding with sparsity constraints: self-feeding sparse SENSE. *Magn Reson Med* 2010;64:1078–1088.
- Chang C, Ji J. Compressed sensing MRI with Multichannel data using multicore processors. *Magn Reson Med* 2010;64:1135–1139.
- Bilgin A, Kim Y, Liu F, Nadar M. Dictionary Design for Compressed Sensing MRI. In: *Proceedings of the ISMRM, Stockholm, Sweden, 2010*. p 4887.
- Lange T, Shulte R, Boesiger P. Quantitative J-resolved prostate spectroscopy using two-dimensional prior-knowledge fitting. *Magn Reson Med* 2008;59:966–972.
- DeFeo E, Cheng L. Characterizing human cancer metabolomics with ex vivo 1H HRMAS MRS. *Technol Cancer Res Treat* 2010;9:381–391.
- Ogg R, Kingsley P, Taylor J. WET, a T1 and B1 insensitive water-suppression method for in Vivo localized 1H NMR spectroscopy. *J Magn Reson B* 1994;104:1–10.
- Bottomley P. Spatial localization in NMR spectroscopy in vivo. *Ann NY Acad Sci* 1987;508:333–348.
- Klose U. In vivo proton spectroscopy in presence of Eddy currents. *Magn Reson Med* 1990;14:26–30.
- Goldstein T, Osher S. The split Bregman method for L1-regularized problems. *SIAM J Imaging Sci* 2009;2:323–343.
- Schulte RF and Boesiger P. ProFit: two-dimensional prior-knowledge fitting of J-resolved spectra. *NMR Biomed* 2006;19:255–263.
- Macura S, Brown L. Improved sensitivity and resolution in two-dimensional homonuclear J-resolved NMR spectroscopy of macromolecules. *J Magn Reson* 1982;53:529–535.
- Wilman A, Allen P. The response of the strongly coupled AB system of citrate to typical 1H MRS localization sequences. *J Magn Reson B* 1995;107:25–33.
- Yue K, Marumoto A, Binesh N, Thomas M. 2D JPRESS of human prostates using an endorectal receiver coil. *Magn Reson Med* 2002;47:1059–1064.
- Mueller-Lisse U, Scherr M. Proton MR spectroscopy of the prostate. *Eur J Radiol* 2007;63:351–360.
- Wang X, Wang B, Gao Z, Liu J, Liu Z, Sun QNZ, Yuan Y. 1H-MRSI of prostate cancer: the relationship between metabolite ratio and tumor proliferation. *Eur J Radiol* 2010;73:345–351.
- Rudin L, Osher S, Fatemi E. Nonlinear total variation based noise removal algorithms. *Phys D* 1992;60:259–268.
- Aeron S, Saligrama V, Zhao M. Information theoretic bounds for compressed sensing. *IEEE Trans Inf Theory* 2010;56:5111–5130.

Accelerated echo planar *J*-resolved spectroscopic imaging in prostate cancer: a pilot validation of non-linear reconstruction using total variation and maximum entropy

Rajakumar Nagarajan^a, Zohaib Iqbal^a, Brian Burns^a, Neil E. Wilson^a, Manoj K. Sarma^a, Daniel A. Margolis^a, Robert E. Reiter^b, Steven S. Raman^a and M. Albert Thomas^{a*}

The overlap of metabolites is a major limitation in one-dimensional (1D) spectral-based single-voxel MRS and multivoxel-based MRSI. By combining echo planar spectroscopic imaging (EPSI) with a two-dimensional (2D) *J*-resolved spectroscopic (JPRESS) sequence, 2D spectra can be recorded in multiple locations in a single slice of prostate using four-dimensional (4D) echo planar *J*-resolved spectroscopic imaging (EP-JRESI). The goal of the present work was to validate two different non-linear reconstruction methods independently using compressed sensing-based 4D EP-JRESI in prostate cancer (PCa): maximum entropy (MaxEnt) and total variation (TV). Twenty-two patients with PCa with a mean age of 63.8 years (range, 46–79 years) were investigated in this study. A 4D non-uniformly undersampled (NUS) EP-JRESI sequence was implemented on a Siemens 3-T MRI scanner. The NUS data were reconstructed using two non-linear reconstruction methods, namely MaxEnt and TV. Using both TV and MaxEnt reconstruction methods, the following observations were made in cancerous compared with non-cancerous locations: (i) higher mean (choline + creatine)/citrate metabolite ratios; (ii) increased levels of (choline + creatine)/spermine and (choline + creatine)/myo-inositol; and (iii) decreased levels of (choline + creatine)/(glutamine + glutamate). We have shown that it is possible to accelerate the 4D EP-JRESI sequence by four times and that the data can be reliably reconstructed using the TV and MaxEnt methods. The total acquisition duration was less than 13 min and we were able to detect and quantify several metabolites. Copyright © 2015 John Wiley & Sons, Ltd.

Keywords: MRS; prostate cancer; 4D EP-JRESI; citrate; myo-inositol; Glx; echo planar spectroscopic imaging

INTRODUCTION

Prostate cancer (PCa) is the most commonly diagnosed non-cutaneous malignancy in the USA and is the second leading cause of cancer-related death in men (1). One in six men will be diagnosed with PCa during their lifetime, but only one in 36 will die of this disease. Currently, the annual prostate-specific antigen (PSA) test and digital rectal examination (DRE) are routinely performed (2) for screening. The PSA screening test measures the serum level of PSA in blood samples. However, it is a controversial test because 65–75% of PSA screening gives false-positive results leading to overdiagnosis (3). The use of systematic transrectal biopsy can miss significant cancer lesions because of random sampling error (4) and the observation that one-third of significant tumors lie in the anterior part of the gland, based on studies of radical prostatectomy specimens (5). Hence, there is an immediate need for early, yet accurate, detection of PCa to improve disease outcomes.

¹H MRS enables the detection of a range of biochemicals in the prostate by making use of the proton signals in these molecules. The detection of biochemicals *in vivo* is limited to concentrations of more than 0.5–1 mM. Signals of citrate (Cit), creatine (Cr), choline (Ch) and spermine (Spm) can be detected

throughout the prostate, with increased levels of Ch and decreased levels of Cit being indicative of cancer (6–8).

* Correspondence to: M. A. Thomas, Radiological Sciences, David Geffen School of Medicine at UCLA, Los Angeles, 90095 CA, USA.
E-mail: athomas@mednet.ucla.edu

a R. Nagarajan, Z. Iqbal, B. Burns, N. E. Wilson, M. K. Sarma, D. A. Margolis, S. S. Raman, M. A. Thomas
Radiological Sciences, University of California Los Angeles, Los Angeles, CA, USA

b R. E. Reiter
Urology, University of California Los Angeles, Los Angeles, CA, USA

Abbreviations used: 1D, one-dimensional; 2D, two-dimensional; 3D, three-dimensional; 4D, four-dimensional; AUC, area under the curve; Ch, choline; Cit, citrate; Cr, creatine; DRE, digital rectal examination; EP-JRESI, echo planar *J*-resolved spectroscopic imaging; EPSI, echo planar spectroscopic imaging; Gln, glutamine; Glu, glutamate; Glx, glutamine + glutamate; JPRESS, *J*-resolved spectroscopy/spectroscopic; MaxEnt, maximum entropy; ml, myo-inositol; NPV, negative predictive value; NUS, non-uniform undersampling/non-uniformly undersampled; NWS, non-water-suppressed; PCa, prostate cancer; PPV, positive predictive value; PSA, prostate-specific antigen; PZ, peripheral zone; RF, radiofrequency; ROC, receiver operating characteristic; SNR, signal-to-noise ratio; Spm, spermine; TV, total variation; T2W, T₂-weighted; VOI, volume of interest; WS, water-suppressed.

Current limitations of single-voxel-based MRS and MRSI in the prostate are caused by the overlap of metabolite resonances, allowing the quantification of only a few metabolites (Cit, Ch, Cr and Spm) and the use of long TEs. The conventional MRSI technique can be accelerated by echo planar spectroscopic imaging (EPSI) (9–13). EPSI speeds up MRSI using an echo planar readout of one spectral and one spatial dimension, thereby achieving an acceleration factor equal to the number of points along one of the spatial dimensions. For example, a two-dimensional (2D) spatial matrix array (16 × 16) would be acquired 16 times faster with EPSI than with conventional MRSI. However, the acceleration may be at the cost of the signal-to-noise ratio (SNR) (11) and the spectra could be affected by Nyquist ghost artifacts (14).

A single-voxel-based 2D J-resolved spectroscopic (JPRESS) sequence has been evaluated in PCa, and has shown improved spectral dispersion because of the added spectral dimension (15,16). New computational methods have made compressed sensing feasible to accelerate MRI by exploiting the sparsity of the images in a known transform domain to reconstruct non-uniformly undersampled (NUS) k -space data (17). For further acceleration, the application of compressed sensing for MRSI is apt, exploiting sparsity in multiple dimensions of frequency and space in transform domains of wavelets and total variation (TV) (18–20). By combining EPSI with JPRESS, 2D spectra can be recorded in multiple locations in the prostate using four-dimensional (4D) echo planar J-resolved spectroscopic imaging (EP-JRESI), which combines two spectral with two spatial dimensions. A pilot feasibility has been demonstrated recently to map metabolites in the healthy human prostate and brain (21,22).

Maximum entropy (MaxEnt) reconstruction finds the spectrum that maximizes entropy whilst maintaining consistency with the measured data. MaxEnt reconstruction is an alternative non-linear reconstruction technique to compressed sensing. MaxEnt has been successfully used to reconstruct undersampled images in astronomy and multidimensional spectra in NMR (23–25), but has not been applied to the spatial-spectral domain (k_y - t_1) of 4D EP-JRESI of PCa. MaxEnt and TV algorithms have been used to reconstruct the NUS indirect spectral and spatial dimensions (21,26).

The TV algorithm was first proposed by Rudin *et al.* (27) for image denoising and, since then, has been successfully used for image restoration. In the TV algorithm, an objective function using the TV norm is minimized subject to a data fidelity term posed by the acquired projection data. Minimization of the image gradient essentially suppresses those high spatial frequency parts, such as streaking artifacts and noise, in the reconstructed images.

The goal of the present work was to validate the MaxEnt and TV non-linear reconstruction algorithms separately in patients with PCa using compressed sensing-based 4D EP-JRESI data.

MATERIALS AND METHODS

Patients

Between March 2012 and May 2013, twenty-two patients with PCa with a mean age of 63.8 years (range, 46–79 years), who subsequently underwent radical prostatectomy, were selected for the study. The patients' Gleason scores varied between 6 and 9. Their PSA levels varied from 0.7 to 22.8 ng/mL (mean, 6.23 ng/mL). These patients were scanned using a 3-T Siemens (Siemens Medical Solutions, Erlangen, Germany) MRI scanner with an endorectal 'receive' coil. The protocol combining MRI

and MRS was performed at least 8 weeks after transrectal ultrasound-guided sextant biopsy. The entire protocol was approved by the Institutional Review Board, and informed consent was obtained from each patient. PCa was histopathologically confirmed after radical prostatectomy. The voxels covering the tumorous lesions from the peripheral zone (PZ) were selected and indicated as tumor voxels, which was confirmed by the pathology report. After reconstruction, the EP-JRESI data were overlaid onto MRI images.

MRI and MRSI

A body matrix phased-array coil assembly, combined with an endorectal coil, was used in the 'receive' mode, whereas a quadrature body 'transmit' coil was used. All patients were imaged in the supine (feet-first) position. Axial images were oriented to be perpendicular to the long axis of the prostate, which was guided by the sagittal images. Axial, coronal and sagittal T_2 -weighted (T_2W) turbo spin echo images were recorded using the following parameters: TR/TE = 3850–4200 ms/96–101 ms; slice thickness, 3 mm; field of view, 20 × 20 cm²; echo train length, 13; data matrix, 320 × 256.

A compressed sensing-based 4D EP-JRESI sequence was validated on the 3-T MRI scanner and the volume of interest (VOI) was localized using three slice-selective radiofrequency (RF) pulses (90°–180°–180°) (Fig. 1). The total time for the acquisition of a fully sampled 4D EP-JRESI scan (TR = 1.5 s, 16 k_y × 16 k_x , 64–100 t_1 , 512 t_2) can be more than 25 min. The parameters for EP-JRESI were as follows: TR/TE/Avg = 1500 ms/30 ms/2; 16 phase-encoding steps; 512 complex points with an F_2 bandwidth of 1190 Hz along the detected dimension. For the second dimension (F_1), 64 increments with bandwidths of 1000 Hz were used. The in-plane spatial resolution and slice thickness were 1 × 1 cm² and 1 cm, respectively. As the EPSI readout simultaneously acquires one spatially encoded dimension (k_x) and one temporal dimension (t_2), we propose the use of NUS in the remaining k_y - t_1 plane, followed by compressed sensing reconstruction (MaxEnt and TV). A 4 × NUS was imposed along the plane containing the incremented spectral and spatial dimensions (t_1 and k_y). Despite the mixing of spatial and spectral dimensions in the reconstruction, the sparsity requirement for reconstruction is shown to be satisfied, as required by compressed sensing. As the k_y - t_1 values are incremented, NUS can be applied along the k_y - t_1 plane.

The individual voxel volume in human prostate was 1 mL. Two sets of data were collected: one water-suppressed (WS) scan with a total scan time of 12 min and a second non-water-suppressed (NWS) scan using one average and one t_1 increment (30 s). The NWS scan was used for phase corrections (eddy current corrections). The full width at half-maximum of the water peak in the cancerous and non-cancerous locations was between 20 and 25 Hz.

Data analysis

The NUS data were reconstructed by MaxEnt and TV separately. A modified Split-Bregman algorithm (28) solves the unconstrained TV optimization problem as:

$$\min_m \|\nabla m\|_1 + \lambda \|F_u m - y\|_2 \quad [1]$$

where ∇ is the gradient operator, m is the reconstructed data, $\|x\|_1$ is the l_1 -norm, λ is a regularization parameter, F_u is the

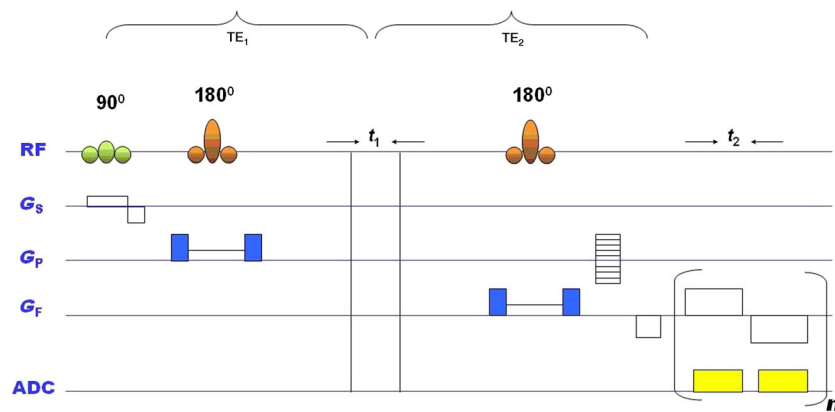


Figure 1. Schematic diagram of the four-dimensional (4D) echo planar *J*-resolved spectroscopic imaging (EP-JRESI) pulse sequence with the volume of interest (VOI) localized using point-resolved spectroscopy with three radiofrequency (RF) pulses (90°, 180°, 180°). The indirect dimension (t_1) was introduced before the last 180° pulse. ADC, analog to digital converter; G_s , G_p and G_f , gradients for slice selection, phase encoding and frequency encoding, respectively; t_2 , detected dimension; n , number of echo planar imaging bipolar readouts.

undersampled Fourier transform and y is the undersampled data. The above equation removes the incoherent artifacts caused by NUS by minimizing TV, whilst maintaining consistency with the sampled measurements. The TV regularization parameters were the same as reported by Burns *et al.* (29). We have used the Split-Bregman reconstruction method primarily for its robustness against the regularization parameters chosen. Because of the use of Bregman parameters in the reconstruction algorithm, which are calculated using the difference between the reconstruction and the sampled data at each iteration, the influence of the regularization parameters is greatly lessened compared with the use of other algorithms that solve the TV problems. Although the choice of parameters can influence the reconstruction, the algorithm allows for a wider range of possible values in order to achieve roughly the same results.

MaxEnt is a constrained convex optimization algorithm that uses a variant of the conjugate gradient method to iteratively solve the inverse problem (23,25,28):

$$\text{maximize } S_{1/2}(f) \text{ such that } \|F^{-1} Kf - D\|_2 \leq \sigma \quad [2]$$

where f is the estimated fully sampled spectrum at each iteration, F^{-1} is the inverse Fourier transform, K is the NUS matrix, D is the measured time domain data, σ is the noise standard deviation and $S_{1/2}(f)$ is the spin - 1/2 entropy of the estimated spectrum (24). All compressed sensing 4D EP-JRESI data were processed using TV and MaxEnt reconstruction with custom MATLAB software. The reconstruction time for each method took about 25 min using an 8 GB RAM, Intel Core i7-2600 CPU @ 3.40 GHz. For the 2D data processing, the raw matrix was apodized with phase shifted and squared sine bell functions along t_1 and t_2 , and zero filled to 128×1024 prior to fast Fourier transformation along the two dimensions. All 2D spectra were presented as contour plots, and the 2D spectral matrices were not skewed by 45° about $F_1 = 0$ Hz.

Statistical analysis

Statistical analyses were performed with SPSS 21 (SPSS Inc., Chicago, IL, USA). Using logistic regression analysis, areas under the curve (AUCs) of the receiver operating characteristic (ROC) were calculated for various metabolites to discriminate between

MaxEnt and TV reconstruction methods. In addition, the paired t -test was used to determine the various metabolite ratios in cancerous and non-cancerous locations. $p < 0.05$ was considered to be statistically significant.

RESULTS

Using this pilot validation, 2D peaks attributed to Cit, Ch, Cr, Spm, myo-inositol (ml) and glutamate (Glu) plus glutamine (Gln) (Glu + Gln = Glx) were quantified in cancerous and non-cancerous locations using the peak integration MATLAB code. Figure 2 shows (Ch + Cr)/Cit, (Ch + Cr)/Spm, (Ch + Cr)/ml and (Ch + Cr)/Glx of cancerous and non-cancerous locations processed by TV and MaxEnt. The mean metabolite ratios (\pm standard deviation, SD) of Cit, Spm, ml and Glx of the non-cancerous locations, processed using TV, were 1.158 ± 0.830 , 2.396 ± 1.95 , 5.325 ± 2.42 and 5.404 ± 2.74 , respectively. In the cancerous locations, the corresponding metabolite ratios were: 4.209 ± 2.132 , 2.808 ± 1.77 , 5.640 ± 2.18 and 5.275 ± 2.80 . Similarly, the mean metabolite ratios (\pm SD) of Cit, Spm, ml and Glx of the non-cancerous locations, calculated using the MaxEnt-reconstructed data, were 1.079 ± 0.795 , 2.096 ± 1.06 , 4.967 ± 2.114 and 5.902 ± 3.40 , respectively. In the cancerous locations, the corresponding metabolite ratios were 3.620 ± 1.759 , 2.727 ± 1.46 , 6.008 ± 2.57 and 5.275 ± 3.19 .

We found that the mean Cit metabolite ratios were significantly higher in cancerous locations relative to non-cancerous locations in both the TV and MaxEnt reconstructions ($p < 0.005$). Increased levels of Spm ($p = 0.46$) and ml ($p = 0.65$) ratios, and decreased levels of Glx ($p = 0.88$) ratios, were observed in cancerous locations relative to non-cancerous locations in the TV reconstruction. Similarly, in the MaxEnt reconstruction, increased levels of Spm ($p = 0.25$) and ml ($p = 0.15$) ratios, and decreased levels of Glx ($p = 0.81$) ratios, were observed in cancerous locations relative to non-cancerous locations. None of the ratios could discriminate significantly between differing grades (Gleason scores) of PCa because of overlap of the ratio values.

Figure 3 shows spatial maps of (Ch + Cr) for the TV and MaxEnt reconstructed data acquired in a 74-year-old patient with PCa. The MaxEnt and TV reconstructions of the cancerous (Fig. 4B, D) and non-cancerous (Fig. 4C, E) locations extracted from the

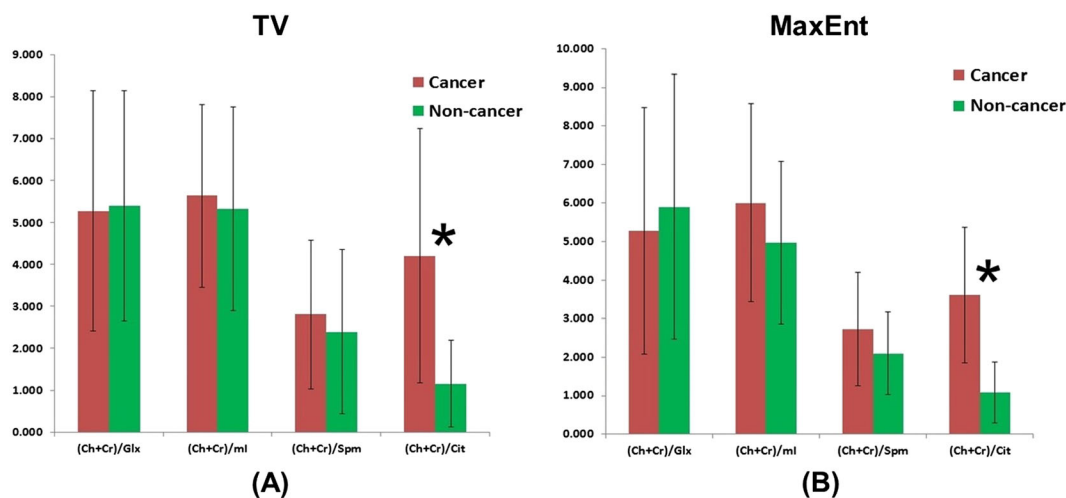


Figure 2. Metabolite ratios of citrate (Cit), spermine (Spm), myo-inositol (ml) and glutamine + glutamate (Glx) in cancerous and non-cancerous locations processed by non-linear reconstruction methods using total variation (TV) and maximum entropy (MaxEnt). Ch, choline; Cr, creatine.

JPRESS spectrum, obtained from the 4D EP-JRESI data, are shown in Fig. 4. Figure 4C illustrates the regions of interest used for peak integration. We compared and correlated the TV and MaxEnt reconstruction methods for Cit, Spm, ml and Glx in the cancerous and non-cancerous locations. The correlation of the (Ch + Cr)/Cit, (Ch + Cr)/Spm, (Ch + Cr)/ml and (Ch + Cr)/Glx ratios for the MaxEnt and TV reconstructions in the cancerous locations are shown in Fig. 5. For each patient, two to three voxels were selected in the PZ of the cancerous and non-cancerous locations, and the average values for each location were reported. A positive correlation was found for the following metabolites in the cancerous locations: (Ch + Cr)/Cit ($R^2 = 0.85$), (Ch + Cr)/Glx ($R^2 = 0.96$), (Ch + Cr)/Spm ($R^2 = 0.86$) and (Ch + Cr)/ml ($R^2 = 0.95$). The concentration of Cit is higher in healthy prostate. Hence, if the Cit peak was higher than the Ch peak, the voxel was considered to be non-cancerous for (Ch + Cr)/Cit values below 0.5 and malignant for (Ch + Cr)/Cit values above 0.5. These values were selected manually on each subject.

The results of the logistic regression analysis and consequent ROC curve analyses are given in Table 1, including the sensitivity,

specificity, positive predictive value (PPV), negative predictive value (NPV), AUC and accuracy for the classification of the MaxEnt and TV methods. ROC curve analyses for differentiating the metabolite ratios of cancerous and non-cancerous locations in MaxEnt suggest that the Cit ratio gives the best predictability, with a sensitivity of 86.4%, specificity of 90.0%, accuracy of 88.6% and AUC = 94.0%. In addition, the overall sensitivity, specificity, accuracy and AUC of ml and Spm were slightly better in MaxEnt compared with TV.

DISCUSSION

Using the NUS data with non-linear iterative reconstruction, we have validated the TV and MaxEnt reconstruction methods independently in patients with PCa using EP-JRESI in a clinically feasible time. In addition to a significantly increased Cit ratio in cancerous locations, increased metabolite ratios of Spm and ml, and decreased ratios of Glx, were found in cancerous locations compared with non-cancerous locations. Although TV and

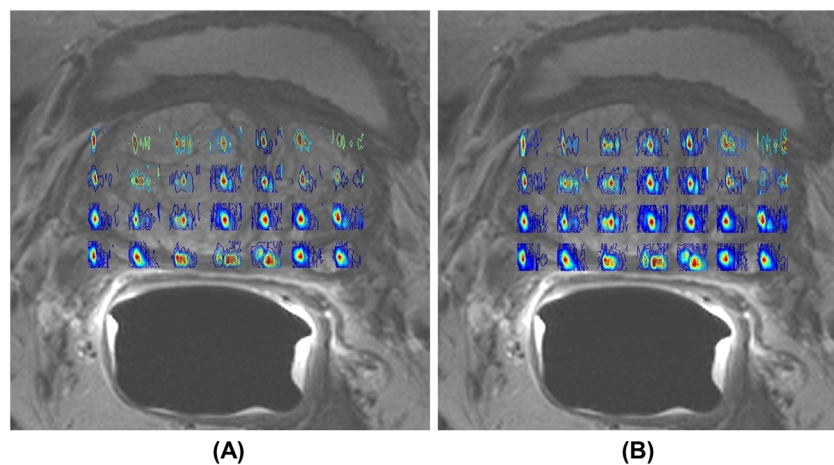


Figure 3. Spatial maps of (choline + creatine) [(Ch + Cr)] for total variation (TV) (A) and maximum entropy (MaxEnt) (B) non-linear reconstruction methods of the four-dimensional (4D) echo planar *J*-resolved spectroscopic imaging (EP-JRESI) data recorded in a 74-year-old patient with prostate cancer (PCa). EP-JRESI was overlaid on top of the T_2 -weighted MRI.

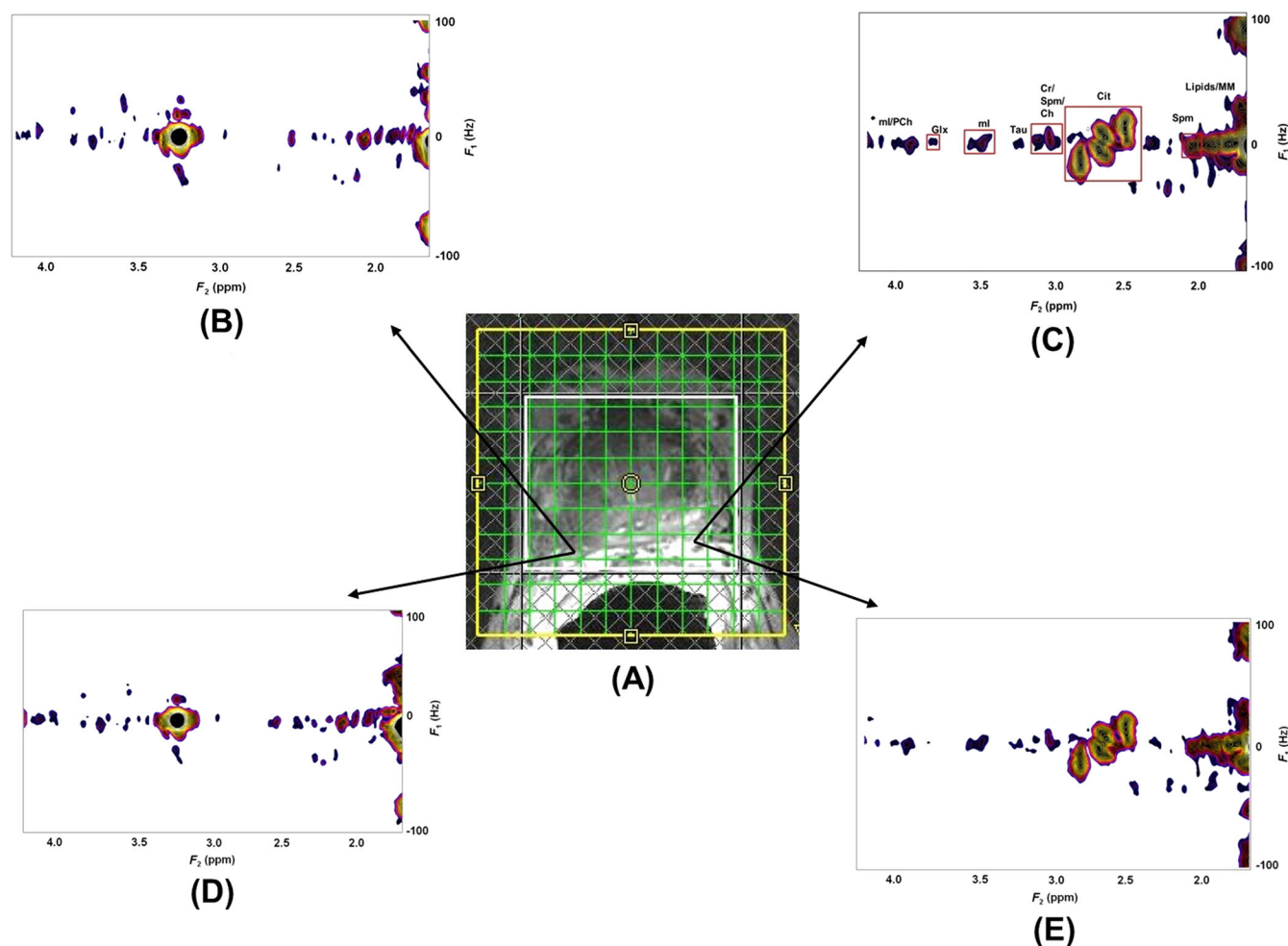


Figure 4. Echo planar J -resolved spectroscopic imaging (EP-JRESI) voxel localization on top of the T_2 -weighted MRI (A); two-dimensional (2D) J -resolved spectroscopy (JPRESS) spectra extracted from the maximum entropy (MaxEnt) and total variation (TV) reconstructions of cancerous (B, D) and non-cancerous (C, E) locations. The regions of interest used for peak integration are shown in (C); (MM, macromolecules; Cit, citrate; Glx, glutamine + glutamate; ml/PCh, myo-inositol/phosphocholine; Tau, taurine; Spm, spermine).

MaxEnt reconstruction methods showed comparable results in cancerous and non-cancerous locations, the sensitivity, accuracy and AUC were slightly increased in the MaxEnt reconstruction.

In the present study, we report the ratios of (Ch+Cr)/Cit, (Ch+Cr)/Spm, (Ch+Cr)/ml and (Ch+Cr)/Glx, because of the proximity of the total Cr peak (3.0 ppm) to the total Ch peak (3.2 ppm) in these *in vivo* MR spectra, which were therefore not always separable. In this study, significantly higher ratios of Cit were observed in the PZ of cancerous locations.

It is likely that the drop in Cit levels precedes malignant transformation (30). It has been suggested that, as a result of a metabolic switch, neoplastic cells oxidize Cit, whereas normal prostatic cells show a low Cit oxidizing capability (31). Decreased levels of zinc, which would relieve *m*-aconitase from inhibition, has been proposed as one of the reasons for the decreased level of Cit in PCa (30).

Ch is an essential component of cell membrane synthesis and phospholipid metabolism, and functions as an important methyl donor. Ch-containing molecules are an essential component of cell membranes, which are more highly concentrated in tumorous areas within the prostate than in healthy prostate tissue (32,33). Ch groups are precursors and breakdown products of the phospholipid phosphatidylcholine, a major cell membrane

compound (34). Increased Ch is observed as a result of altered phospholipid metabolism in PCa cell lines (33). This alteration is most probably a result of an increased expression and activity of choline kinase, a higher rate of Ch transport and an increased phospholipase activity (34).

The polyamines Spm, spermidine and putrescine are essential for the differentiation and proliferation of cells, the synthesis of DNA, RNA and proteins, and the stabilization of cell membranes and cytoskeletal structures (35). Previous studies have observed high levels of Spm in healthy prostate tissue and benign prostatic hyperplasia, and reduced Spm levels in malignant prostate tissue (16,36–38).

The osmoregulator ml is expressed in a variety of tissues, and its decrease was observed in PCa within human expressed prostatic secretions using high-resolution NMR (39) and in breast tumors (40). In our study, slightly increased ml ratios were observed in cancerous locations, but were not statistically significant.

Glu and Gln are difficult to resolve owing to resonance overlap. As a result, most MRS studies use the sum of Glu and Gln (expressed as Glx or Glu + Gln). Glu is extensively involved in metabolic and oncogenic pathways. Koochekpour (41) showed that serum Glu levels correlated directly with Gleason scores

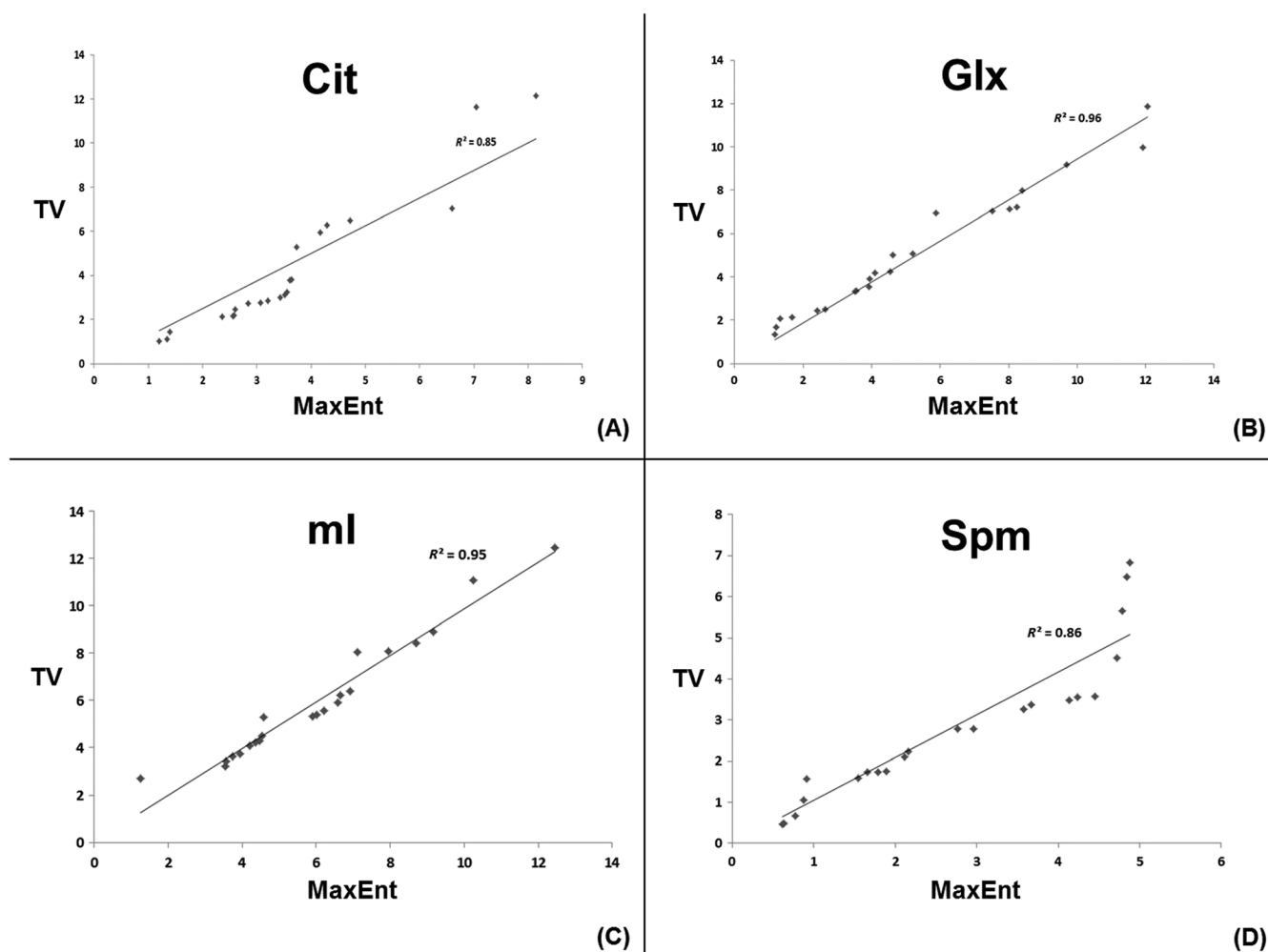


Figure 5. Correlation of maximum entropy (MaxEnt) and total variation (TV) non-linear reconstruction methods for citrate (Cit) (A), glutamine + glutamate (Glx) (B), myo-inositol (ml) (C) and spermine (Spm) (D) in cancerous locations. R^2 values are shown for each metabolite.

Table 1. Measures of sensitivity, specificity, positive predictive value (PPV), negative predictive value (NPV) and accuracy of maximum entropy (MaxEnt) and total variation (TV) methods using receiver operating characteristic (ROC) curve analysis

Metabolite	MaxEnt						
	Sensitivity (%)	Specificity (%)	Accuracy (%)	PPV (%)	NPV (%)	AUC (%)	
Cit	86.4	90.0	88.6	90.5	87.0	94.0	
Glx	66.6	31.8	47.7	48.3	46.7	56.9	
ml	54.5	63.6	59.1	60.0	58.3	65.1	
Spm	50.0	72.7	61.4	64.7	59.3	64.9	
Metabolite	TV						
	Sensitivity (%)	Specificity (%)	Accuracy (%)	PPV (%)	NPV (%)	AUC (%)	
	Cit	86.4	90.9	88.6	90.5	87.0	92.1
	Glx	63.6	36.4	50.0	50.0	50.0	57.2
	ml	40.9	59.1	50.0	50.0	50.0	58.5
Spm	50.0	63.6	56.8	57.9	56.0	58.5	

Cit, citrate; Glx, glutamine + glutamate; ml, myo-inositol; Spm, spermine.

(<6 versus >8) and primary PCa aggressiveness. In our study, decreased Glx ratios were found in cancerous locations, but were not statistically significant.

There was an overlap between cancerous and non-cancerous locations, possibly as a result of the low SNR of the Cr peak. As

a result of patient movement and B_0 inhomogeneity, the resonances of Ch, Cr and Spm are difficult to resolve, especially in cancerous locations, adding to the uncertainty in quantification. However, the use of prior knowledge fitting (ProFit) may improve accurate metabolite (42) quantification, which warrants future

investigation. As a result of the limited patient population, we did not find any significant changes in other metabolites. In addition, this study focused on the PZ of the prostate, where only 80% of cancer occurs. The advantage of the compressed sensing-based 4D EP-JRESI sequence is that it records short TE-based spectra from multiple regions of human prostate, and additional metabolites, such as ml, Spm and Glx, to the normally detected Cit, Cr and Ch.

This pilot work demonstrated the use of slice-based 4D EP-JRESI, and future work will focus on volume-based, five-dimensional (5D) EP-JRESI in PCa (43). Compressed sensing-based 4D EP-JRESI shortens the total acquisition time, effectively enabling future potential to extend to pathological evaluations in a clinical set-up. The current validation method may require further optimization to improve the overall performance. As reported by Burns *et al.* (26), the sample mask is crucial to the SNR of each reconstructed prostate metabolite for the 4D EP-JRESI data. Further optimization of the reduction in non-linearity of the reconstructed peaks may enable accurate quantification of metabolites. In addition, future work will address the use of Poisson gap *versus* deterministic sample masks, and the optimization of the modulation functions for specific metabolites relevant to PCa.

CONCLUSION

We were able to detect metabolites in PCa using compressed sensing-based 4D EP-JRESI data acquired in clinically acceptable times (<12 min). We have shown that it is possible to undersample the 4D EP-JRESI sequence with an acceleration factor of four times, and that the data can be reliably reconstructed using the TV and MaxEnt methods. Both non-linear reconstruction methods provided comparable results.

Acknowledgements

This work was supported by a Congressionally Directed Medical Research Program (CDMRP) grant from the US Army Prostate Cancer Research Program (#W81XWH-11-1-0248) and National Institutes of Health / National Cancer Institute (NIH/NCI) (P50CA092131).

REFERENCES

1. Siegel R, Naishadham D, Jemal A. Cancer statistics, 2013. *CA Cancer J Clin.* 2013; 63(1): 11–30.
2. Andriole GL, Crawford ED, Grubb RL 3rd, Buys SS, Chia D, Church TR, Fouad MN, Gelmann EP, Kvale PA, Reding DJ, Weissfeld JL, Yokochi LA, O'Brien B, Clapp JD, Rathmell JM, Riley TL, Hayes RB, Kramer BS, Izmirlan G, Miller AB, Pinsky PF, Prorok PC, Gohagan JK, Berg CD, PLCO Project Team. Mortality results from a randomized prostate-cancer screening trial. *N. Engl. J. Med.* 2009; 360(13): 1310–1319.
3. Smith DS, Humphrey PA, Catalona WJ. The early detection of prostate carcinoma with prostate specific antigen: the Washington University experience. *Cancer* 1997; 80: 1852–1856.
4. Djavan B, Ravery V, Zlotta A, Dobronski P, Dobrovits M, Fakhari M, Seitz C, Susani M, Borkowski A, Boccon-Gibod L, Schulman CC, Marberger M. Prospective evaluation of prostate cancer detected on biopsies 1, 2, 3 and 4: when should we stop? *J. Urol.* 2001; 166: 1679–1683.
5. McNeal JE, Redwine EA, Freiha FS, Stamey TA. Zonal distribution of prostatic adenocarcinoma. Correlation with histologic pattern and direction of spread. *Am. J. Surg. Pathol.* 1988; 12: 897–906.
6. Thomas MA, Narayan P, Kurhanewicz J, Jajodia P, Weiner MW. ¹H MR spectroscopy of normal and malignant human prostates in vivo. *J. Magn. Reson. B* 1990; 87: 610–619.

7. Kurhanewicz J, Vigneron DB, Nelson SJ, Hricak H, MacDonald JM, Konety B, Narayan P. Citrate as an in vivo marker to discriminate prostate cancer from benign prostatic hyperplasia and normal prostate peripheral zone: detection via localized proton spectroscopy. *Urology* 1995; 45: 459–466.
8. Kurhanewicz J, Vigneron DB, Hricak H, Narayan P, Carroll P, Nelson SJ. Three-dimensional H-1 MR spectroscopic imaging of the in situ human prostate with high (0.24–0.7-cm³) spatial resolution. *Radiology* 1996; 198: 795–805.
9. Mansfield P. Spatial mapping of the chemical shift in NMR. *Magn. Reson. Med.* 1984; 1: 370–386.
10. Matsui S, Sekihara K, Kohno H. High-speed spatially resolved high-resolution NMR spectroscopy. *J. Am. Chem. Soc.* 1985; 107: 2817–2818.
11. Posse S, Tedeschi G, Risinger R, Ogg R, Bihan DL. High speed ¹H spectroscopic imaging in human brain by echo planar spatial-spectral encoding. *Magn. Reson. Med.* 1995; 33: 34–40.
12. Ericsson A, Weis J, Sperber GO, Hemmingsson A. Measurements of magnetic field variations in the human brain using a 3D-FT multiple gradient echo technique. *Magn. Reson. Med.* 1995; 33: 171–177.
13. Ebel A, Soher BJ, Maudsley AA. Assessment of 3D proton MR echo-planar spectroscopic imaging using automated spectral analysis. *Magn. Reson. Med.* 2001; 46: 1072–1078.
14. Du W, Du YP, Fan X, Zamora MA, Karczmar GS. Reduction of spectral ghost artifacts in high-resolution echo-planar spectroscopic imaging of water and fat resonances. *Magn. Reson. Med.* 2003; 49(6): 1113–1120.
15. Ryner LN, Sorenson JA, Thomas MA. Localized 2D J-resolved ¹H MR spectroscopy: strong coupling effects in vitro and in vivo. *Magn. Reson. Imaging* 1995; 13(6): 853–869.
16. Nagarajan R, Gomez AM, Raman SS, Margolis DJ, McClure T, Thomas MA. Correlation of endorectal 2D JPRESS findings with pathological Gleason scores in prostate cancer patients. *NMR Biomed.* 2010; 23(3): 257–261.
17. Lustig M, Donoho D, Pauly JM. Sparse MRI: the application of compressed sensing for rapid MR imaging. *Magn. Reson. Med.* 2007; 58(6): 1182–1195.
18. Hu S, Lustig M, Balakrishnan A, Larson PE, Bok R, Kurhanewicz J, Nelson SJ, Goga A, Pauly JM, Vigneron DB. 3D compressed sensing for highly accelerated hyperpolarized (13)C MRSI with in vivo applications to transgenic mouse models of cancer. *Magn. Reson. Med.* 2010; 63(2): 312–321.
19. Geethanath S, Baek HM, Ganji SK, Ding Y, Maher EA, Sims RD, Choi C, Lewis MA, Kodibagkar VD. Compressive sensing could accelerate ¹H MR metabolic imaging in the clinic. *Radiology* 2012; 262(3): 985–994.
20. Cao P, Wu EX. Accelerating phase-encoded proton MR spectroscopic imaging by compressed sensing. *J. Magn. Reson. Imaging* 2015; 41(2): 487–495.
21. Furuyama JK, Wilson NE, Burns BL, Nagarajan R, Margolis DJ, Thomas MA. Application of compressed sensing to multidimensional spectroscopic imaging in human prostate. *Magn. Reson. Med.* 2012; 67(6): 1499–1505.
22. Sarma MK, Nagarajan R, Macey PM. Accelerated echo-planar J-resolved spectroscopic imaging in the human brain using compressed sensing: a pilot validation in obstructive sleep apnea. *Am. J. Neuroradiol.* 2014; 35(6 Suppl): S81–S89.
23. Skilling J, Bryan RK. Maximum entropy image reconstruction: general algorithm. *Monthly Notices R. Astronom. Soc.* 1984; 211(1): 111–124.
24. Daniell GJ, Hore PJ. Maximum entropy and NMR—a new approach. *J. Magn. Reson.* 1989; 4(3): 515–536.
25. Hoch J, Stern AS. *NMR Data Processing*. Wiley: New York, NY; 1996.
26. Burns B, Wilson NE, Furuyama JK, Thomas MA. Non-uniformly under-sampled multi-dimensional spectroscopic imaging in vivo: maximum entropy versus compressed sensing reconstruction. *NMR Biomed.* 2014; 27(2): 191–201.
27. Rudin L, Osher S, Fatemi E. Nonlinear total variation based noise removal algorithms. *Physica D* 1992; 60: 259–268.
28. Goldstein T, Osher S. The Split Bregman method for L1 regularized problems. *SIAM J. Imaging Sci.* 2009; 2: 323–343.
29. Burns BL, Wilson NE, Thomas MA. Group sparse reconstruction of multi-dimensional spectroscopic imaging in human brain in vivo. *Algorithms* 2014; 7(3): 276–294.
30. Costello LC, Franklin RB. The intermediary metabolism of the prostate: a key to understanding the pathogenesis and progression of prostate malignancy. *Oncology* 2000; 59: 269–282.
31. Costello LC, Franklin RB, Narayan P. Citrate in the diagnosis of prostate cancer. *Prostate* 1999; 38: 237–245.

32. Kurhanewicz J, Swanson MG, Nelson SJ, Vigneron DB. Combined magnetic resonance imaging and spectroscopic imaging approach to molecular imaging of prostate cancer. *J. Magn. Reson. Imaging* 2002; 16(4): 451–463.
33. Ackerstaff E, Pflug BR, Nelson JB, Bhujwala ZM. Detection of increased choline compounds with proton nuclear magnetic resonance spectroscopy subsequent to malignant transformation of human prostatic epithelial cells. *Cancer Res.* 2001; 61: 3599–3603.
34. Glunde K, Bhujwala ZM. Metabolic tumor imaging using magnetic resonance spectroscopy. *Semin. Oncol.* 2011; 38: 26–41.
35. Jänne J, Pösö H, Raina A. Polyamines in rapid growth and cancer. *Biochim. Biophys. Acta* 1978; 473: 241–293.
36. Van der Graaf M, Schipper RG, Oosterhof GO, Schalken JA, Verhofstad AA, Heerschap A. Proton MR spectroscopy of prostatic tissue focused on the detection of spermine, a possible biomarker of malignant behavior in prostate cancer. *MAGMA* 2000; 10: 153–159.
37. Thomas MA, Nagarajan R, Huda A, Margolis D, Sarma MK, Sheng K, Reiter RE, Raman SS. Multidimensional MR spectroscopic imaging of prostate cancer in vivo. *NMR Biomed.* 2014; 27(1): 53–66.
38. Yue K, Marumoto A, Binesh N, Thomas MA. 2D JPRESS of human prostates using an endorectal receiver coil. *Magn. Reson. Med.* 2002; 47(6): 1059–1064.
39. Serkova NJ, Gamito EJ, Jones RH, O'Donnell C, Brown JL, Green S, Sullivan H, Hedlund T, Crawford ED. The metabolites citrate, myo-inositol, and spermine are potential age-independent markers of prostate cancer in human expressed prostatic secretions. *Prostate* 2008; 68(6): 620–628.
40. Griffin JL, Shockcor JP. Metabolic profiles of cancer cells. *Nat. Rev. Cancer* 2004; 4: 551–561.
41. Koochekpour S. Glutamate, a metabolic biomarker of aggressiveness and potential therapeutic target for prostate cancer. *Asian J. Androl.* 2013; 15(2): 212–213.
42. Lange T, Schulte RF, Boesiger P. Quantitative J-resolved prostate spectroscopy using two-dimensional prior-knowledge fitting. *Magn. Reson. Med.* 2008; 59(5): 966–972.
43. Wilson NE, Iqbal Z, Burns BL, Keller M, Thomas MA. Accelerated five-dimensional echo planar J-resolved spectroscopic imaging: implementation and pilot validation in human brain. *Magn. Reson. Med.* 2015. doi: 10.1002/mrm.25605. [Epub ahead of print]

Chapter 30

Two-Dimensional NMR Spectroscopy Plus Spatial Encoding

**M. Albert Thomas¹, Zohaib Iqbal¹, Manoj K. Sarma¹,
Rajakumar Nagarajan¹, Paul M. Macey¹, and
Amir Huda^{1,2}**

¹University of California, Los Angeles, CA, USA

²California State University, Fresno, CA, USA

30.1	Introduction	495
30.2	Single-voxel-based 2D MRS	497
30.3	Echo-planar Correlated and J-resolved MRSI	506
30.4	Accelerated Echo-planar J-resolved MRSI with Nonuniform Undersampling and Compressed Sensing	514
30.5	Prior-knowledge Fitting for Metabolite Quantitation	515
30.6	Future Directions: Clinical Applications	517
	Acknowledgments	517
	References	517

30.1 INTRODUCTION

It is now almost three decades since one-dimensional (1D; in the chemical shift spectral domain) single-voxel (SV)-based magnetic resonance spectroscopy (MRS) was introduced in the clinical setting.¹⁻³ While it has become an integral part of the diagnostic tools in the clinic for some physicians and selected medical centers, it is still considered by others as an ‘investigational technique’.^{1,3} 1D SV-MRS has developed to a point where the five major cerebral metabolites, myo-inositol (mI), total choline (Cho), total creatine (Cr; phosphorylated plus unphosphorylated), glutamine/glutamate (Glx), and *N*-acetyl aspartate (NAA), are identified and quantified accurately with prior-knowledge fitting algorithms such as *LC Model*, *JMRUI*, and others (see Chapters 18, 19, and 20).⁴⁻⁶ Acquisition times have also been accelerated by stronger gradients, and we have arguably now reached a plateau in terms of what can be further extracted from the 1D technique.¹

Beyond the five main cerebral metabolites, approximately 25 others that have been detected in human brain are not commonly assessed for several reasons.⁶ Some are difficult to detect because they have a weak signal (low concentration or fewer hydrogen

nuclei) and/or many overlapping peaks, for example, *N*-acetylaspartylglutamate (NAAG), aspartate, taurine (Tau), *scyllo*-inositol, betaine, ethanolamine, purine nucleotides, histidine, glucose, and glycogen. Others require the use of 'special techniques' to tease them out because they are obscured by much larger overlapping signals, for example, glutathione and γ -aminobutyric acid (GABA).¹⁻⁷ Yet others such as β -hydroxy-butyrate, acetone, phenylalanine, galactitol, ribitol, arabitol, succinate, pyruvate, alanine, glycine, and threonine are detected only when levels are elevated under abnormal or pathological conditions in various disorders. In addition, some exogenous compounds that cross the blood-brain barrier such as ethanol and methylsulfonylmethane can also be detected by proton MRS.⁸⁻¹⁰

The limitations of the 1D SV-MRS methods of yesteryears still remain to a certain extent.^{1-3,7} Overlapping of spectra due to the chemical shifts of metabolites keeps us from identifying the ones with fewer hydrogen protons and/or lower concentrations. Furthermore, an inability to separate J-coupling from chemical shift leads to assignment problems that hinder the identification and quantification of metabolites.^{11,12} One could, in principle, move to higher main magnetic field strengths (B_0) to better resolve the peaks and reduce the overcrowding, as the relative width of the multiplets in ppm varies inversely with B_0 .¹³ However, currently 3T remains the practical limit in the clinical setting.³

The 'special techniques' noted above for teasing out signal information are often called *homonuclear spectral* or *J-difference editing techniques*.^{14,15} They exploit the J-coupling between coupled spins by selectively perturbing particular resonances on alternate acquisitions during a spin-echo sequence. J-coupling results in multiplet signals with distributed peak intensities (heights) over several peaks, leaving a broader footprint along the chemical shift axis. For example, observing GABA, whose concentration is only 1 mM in the human brain, is difficult because the signal at 3.0 ppm is coupled to the 1.9 ppm peak and overshadowed by large signals from NAA, Glx, and Cr. A frequency-selective pulse, which only directly affects those signals close to 1.9 ppm, can be added to the point-resolved spectroscopy sequence (PRESS). The homonuclear radio frequency (RF) pulse will also have an indirect effect on GABA signals at 3.0 ppm because of the coupling, but not on the other uncoupled signals. If alternate experiments are performed with and without this frequency-selective pulse, the

difference will give a spectrum that only contains the signals affected by the selective perturbation.^{14,15}

There are a couple of obvious drawbacks to this technique.¹⁴⁻¹⁷ One is that only one metabolite is optimized at a time (assuming that the multiplets of the J-coupled metabolites are well separated). The second disadvantage is the requirement for subtraction to remove the strong overlapping signals, which makes the technique highly vulnerable to subject movement and to instrumental factors, etc. that can introduce artifacts into the spectrum.^{16,17} Mescher *et al.* proposed a different metabolite-editing technique based on subtraction of two measurements, called *MEGA (Mescher-Garwood)* that can be combined with the two popular SV-MRS techniques, STEAM (stimulated acquisition mode), and PRESS¹⁸⁻²⁰ (see Chapter 7). Optimized MEGA-editing sequences have also been proposed recently.^{21,22} These newer experimental techniques are inherently preferable because they utilize multiple quantum coherences to suppress overlapping signals in a single scan.^{23,24}

Beyond the problems noted above, it has become desirable over the years to obtain multivoxel information in a reasonable amount of time.²⁵⁻²⁷ Chemical shift imaging (CSI) using 1D MRS has helped satiate this appetite somewhat but it is performed with sequences using long echo times (TEs) and hence incurs partial loss of those cerebral metabolites that have low transverse relaxation times (T_2 s).²⁷⁻³⁰ On the other hand, multidimensional/multivoxel MRS imaging (MRSI) techniques tackle these problems head-on during acquisition by unambiguously resolving many overlapping peaks nonselectively through the addition of spectral dimensions, while postprocessing schemes such as Profit deal with quantification (see Chapter 20).³¹⁻³⁶ These approaches have opened up the application of MRS to many fields, and this will lead to new paradigms in the coming decades.

It is important to note that while multidimensional techniques have been the mainstay in chemistry and biochemistry for decades, the road to bringing multidimensional spectroscopy from *in vitro* to *in vivo* applications has been difficult, primarily because of two major challenges: the B_0 field strength and acquisition times. However, current methodologies have, at least in part, addressed these problems, and state-of-the-art techniques using clinical MRI scanners have improved signal-to-noise ratios (SNR) and reduced acquisition times to clinically practical durations.^{11,12}

Currently, at least 15 cerebral metabolites can be identified and quantified using two-dimensional (2D) localized correlated spectroscopy (L-COSY), which combines the original COSY sequence described by Aue *et al.*³⁷ and postprocessing algorithms developed at the University of California in Los Angeles.^{35,38} A tool that can bring so much additional information surely must increase our diagnostic and patient management capabilities in the clinic. This journey to the state-of-the art today is described below.

30.2 SINGLE-VOXEL-BASED 2D MRS

30.2.1 2D L-COSY: Theory

Figure 30.1 shows the 2D L-COSY sequence that was implemented on a 1.5 T MRI/MRS scanner in 2001, where a combination of three slice-selective RF pulses ($90^\circ - 180^\circ - 90^\circ$) enabled the localization of a volume of interest (VOI) in a single shot.³⁸ After the formation of the Hahn spin echo using the first 90° and 180° RF pulse pair, an incremental period for the second spectral dimension (t_1) was inserted immediately. The last slice-selective 90° RF pulse acted also as the coherence transfer pulse, critical for recording the 2D spectrum.^{37,38} To remove unwanted coherences, this sequence used refocusing B_0 gradient crusher pulses around the slice-selective 180° RF pulse, and also before and after the last 90° RF pulse. In order to improve the SNR from the localized volume, multiple averages could be used in combination with or without a multistep RF phase cycling to minimize any artifacts stemming from improper RF pulses. The 2D L-COSY sequence has been successfully implemented and evaluated on 7, 3, and 1.5 T MRI scanners manufactured by different vendors.³⁸⁻⁴⁶

To understand the nature of the interactions between spins during the evolution, mixing, and detection periods, and how these events modulate the amplitude, frequency, and phase of the 2D spectral signal array, a closer look at the time evolution of a weakly coupled AX type spin-pair system with two protons A and X, whose chemical shift is large compared to the J-coupling between them, is considered here. Using the density matrix formalism, the time course of evolution of coherences and magnetization is presented at the different time points marked in Figure 30.1 to describe the spin state before and after each RF pulse, as well as its evolution during different time intervals.

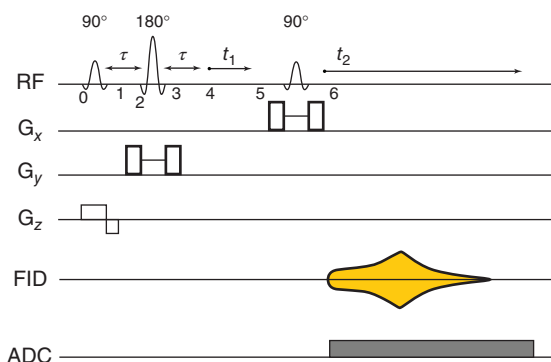


Figure 30.1. A schematic diagram of the 2D L-COSY sequence containing three slice-selective RF pulses (90° , 180° , 90°) for volume localization. The B_0 -crusher gradient pulses were played around the 180° refocusing and the second 90° coherence transfer RF pulses. After the evolution during 2τ , there is a formation of the Hahn spin echo. Direct acquisition along t_2 and indirect detection along t_1 enable encoding of two spectral dimensions

The weakly coupled AX spin system has four energy levels that can lead to 4 observable single quantum (SQ) coherences (ω_{12} , ω_{34} , ω_{13} , ω_{24}) and nonobservable multiple quantum (zero and double quantum) coherences: ω_{23} and ω_{14} under different perturbations.^{37,47} At time point 0 before the first slice-selective 90° RF pulse, the spins are at the Boltzmann equilibrium, and the spin state is described by the F_z matrix as shown below:

$$\rho_0 \propto \begin{pmatrix} 1 & 0 & 0 & 0 \\ 0 & 0 & 0 & 0 \\ 0 & 0 & 0 & 0 \\ 0 & 0 & 0 & -1 \end{pmatrix} \quad (30.1)$$

We assume that the RF pulses are applied along the y-direction in the rotating frame of reference so that the RF pulse rotation operators contain only real numbers. The spin state after the rotation by the first 90° RF pulse along the y-direction (time point 1) is the observable F_x matrix containing nonzero elements for the four SQ coherences:

$$\rho_1 \propto P_y^{-1} F_z P_y$$

$$\rho_1 \propto \frac{1}{4} \begin{pmatrix} 1 & -1 & -1 & 1 \\ 1 & 1 & -1 & -1 \\ 1 & -1 & 1 & -1 \\ 1 & 1 & 1 & 1 \end{pmatrix} \begin{pmatrix} 1 & 0 & 0 & 0 \\ 0 & 0 & 0 & 0 \\ 0 & 0 & 0 & 0 \\ 0 & 0 & 0 & -1 \end{pmatrix}$$

$$\begin{pmatrix} 1 & 1 & 1 & 1 \\ -1 & 1 & -1 & 1 \\ -1 & -1 & 1 & 1 \\ 1 & -1 & -1 & 1 \end{pmatrix} \\ \propto \frac{1}{2} \begin{pmatrix} 0 & 1 & 1 & 0 \\ 1 & 0 & 0 & 1 \\ 1 & 0 & 0 & 1 \\ 0 & 1 & 1 & 0 \end{pmatrix} \quad (30.2)$$

After time point 2, the SQ coherences start evolving during τ as shown in Figure 30.1 and the density matrix is

$$\rho_2 \propto \begin{pmatrix} 0 & e^{-i\omega_{(12)}\tau} & e^{-i\omega_{(13)}\tau} & 0 \\ e^{i\omega_{(12)}\tau} & 0 & 0 & e^{-i\omega_{(24)}\tau} \\ e^{i\omega_{(13)}\tau} & 0 & 0 & e^{-i\omega_{(34)}\tau} \\ 0 & e^{i\omega_{(24)}\tau} & e^{i\omega_{(34)}\tau} & 0 \end{pmatrix} \quad (30.3)$$

The evolving SQ coherences are characterized by

$$\omega_{12} \propto (\delta_X + J/2), \quad \omega_{34} \propto (\delta_X - J/2), \\ \omega_{13} \propto (\delta_A + J/2) \quad \text{and} \quad \omega_{24} \propto (\delta_A - J/2) \quad (30.4)$$

where δ_A and δ_X are the chemical shifts of spins A and X and J represents the indirect spin–spin coupling (in rad s^{-1}) that is communicated through the covalent bonds. The direct spin–spin dipolar coupling between the A and X protons communicated through space is assumed to average to zero due to the tumbling motion of these spins. After the evolution through crusher gradient pairs and slice-selective refocusing of the 180° RF pulse at the end of τ , the spin state is described by

$$\rho_3 \propto R_y^{-1} \rho_2 R_y \\ \propto \frac{1}{2} \begin{pmatrix} 0 & 0 & 0 & 1 \\ 0 & 0 & -1 & 0 \\ 0 & -1 & 0 & 0 \\ 1 & 0 & 0 & 0 \end{pmatrix} \\ \begin{pmatrix} 0 & e^{-i\omega_{(12)}\tau} & e^{-i\omega_{(13)}\tau} & 0 \\ e^{i\omega_{(12)}\tau} & 0 & 0 & e^{-i\omega_{(24)}\tau} \\ e^{i\omega_{(13)}\tau} & 0 & 0 & e^{-i\omega_{(34)}\tau} \\ 0 & e^{i\omega_{(24)}\tau} & e^{i\omega_{(34)}\tau} & 0 \end{pmatrix} \\ \begin{pmatrix} 0 & 0 & 0 & 1 \\ 0 & 0 & -1 & 0 \\ 0 & -1 & 0 & 0 \\ 1 & 0 & 0 & 0 \end{pmatrix} \\ \propto \frac{1}{2} \begin{pmatrix} 0 & -e^{i\omega_{(34)}\tau} & -e^{i\omega_{(24)}\tau} & 0 \\ -e^{-i\omega_{(34)}\tau} & 0 & 0 & -e^{i\omega_{(13)}\tau} \\ -e^{-i\omega_{(24)}\tau} & 0 & 0 & -e^{i\omega_{(12)}\tau} \\ 0 & -e^{-i\omega_{(13)}\tau} & -e^{-i\omega_{(12)}\tau} & 0 \end{pmatrix} \quad (30.5)$$

Now, the SQ coherences included in equation (30.5) will evolve under another period, τ and at the end of this period, the first Hahn spin echo is described by

$$\rho_4 \propto -\frac{1}{2} \begin{pmatrix} 0 & e^{i(\omega_{(34)}-\omega_{(12)})\tau} & e^{i(\omega_{(24)}-\omega_{(13)})\tau} & 0 \\ e^{i(\omega_{(12)}-\omega_{(34)})\tau} & 0 & 0 & e^{i(\omega_{(13)}-\omega_{(24)})\tau} \\ e^{i(\omega_{(13)}-\omega_{(24)})\tau} & 0 & 0 & e^{i(\omega_{(12)}-\omega_{(34)})\tau} \\ 0 & e^{i(\omega_{(24)}-\omega_{(13)})\tau} & e^{i(\omega_{(34)}-\omega_{(12)})\tau} & 0 \end{pmatrix} \\ \propto -\frac{1}{2} \begin{pmatrix} 0 & e^{-i2\pi J\tau} & e^{-i2\pi J\tau} & 0 \\ e^{i2\pi J\tau} & 0 & 0 & e^{i2\pi J\tau} \\ e^{i2\pi J\tau} & 0 & 0 & e^{i2\pi J\tau} \\ 0 & e^{-i2\pi J\tau} & e^{-i2\pi J\tau} & 0 \end{pmatrix} \quad (30.6)$$

It is evident from equation (30.6) that the chemical shift and any other linear interaction terms are refocused at the time of the Hahn spin echo and that the spin state contains phase terms with only the bilinear J -coupling term. The rotation operators P_y and R_y used in equations (30.2) and (30.5) represent the 90° and 180° RF pulses, respectively.⁴⁷

The spin state ρ_4 is followed by encoding of the second spectral dimension with a variable time period t_1 , meaning that during a series of repeat experiments, t_1 takes on a different set of values that is similar to phase encoding a second spatial dimension in MRI. The evolution time (t_1) is being incremented here, as opposed to incrementing the amplitude of the phase-encoding gradient in conventional MRI.

$$\rho_5 \propto -\frac{1}{2} \begin{pmatrix} 0 & Ke^{-i\omega_{(12)}t_1} & Ke^{-i\omega_{(13)}t_1} & 0 \\ K^*e^{i\omega_{(12)}t_1} & 0 & 0 & K^*e^{-i\omega_{(24)}t_1} \\ K^*e^{i\omega_{(13)}t_1} & 0 & 0 & K^*e^{-i\omega_{(34)}t_1} \\ 0 & Ke^{i\omega_{(24)}t_1} & Ke^{i\omega_{(34)}t_1} & 0 \end{pmatrix} \quad (30.7)$$

where $K = e^{-i2\pi J\tau}$ and $K^* = e^{i2\pi J\tau}$.

After the evolution during t_1 , the spins evolve during a mixing period in which a slice-selective 90° RF pulse is applied in the third orthogonal plane, again sandwiched by gradient crusher pulses:

$$\rho_6 \propto P_y^{-1} \rho_5 P_y \\ \propto -\frac{1}{8} \begin{pmatrix} 1 & -1 & -1 & 1 \\ 1 & 1 & -1 & -1 \\ 1 & -1 & 1 & -1 \\ 1 & 1 & 1 & 1 \end{pmatrix} \\ \begin{pmatrix} 0 & Ke^{-i\omega_{(12)}t_1} & Ke^{-i\omega_{(13)}t_1} & 0 \\ K^*e^{i\omega_{(12)}t_1} & 0 & 0 & K^*e^{-i\omega_{(24)}t_1} \\ K^*e^{i\omega_{(13)}t_1} & 0 & 0 & K^*e^{-i\omega_{(34)}t_1} \\ 0 & Ke^{i\omega_{(24)}t_1} & Ke^{i\omega_{(34)}t_1} & 0 \end{pmatrix}$$

$$\begin{pmatrix} 1 & 1 & 1 & 1 \\ -1 & 1 & -1 & 1 \\ -1 & -1 & 1 & 1 \\ 1 & -1 & -1 & 1 \end{pmatrix} \quad (30.8)$$

Only the SQ elements of ρ_6 are observable. These are

$$\begin{aligned} (\rho_6)_{12} \propto & \\ & -1/8\{-K^*(e^{i\omega_1 2t_1} + e^{i\omega_1 3t_1} - e^{-i\omega_2 2t_1} - e^{-i\omega_2 3t_1}) \\ & + K(e^{-i\omega_1 2t_1} - e^{-i\omega_1 3t_1} + e^{i\omega_2 2t_1} - e^{i\omega_2 3t_1})\} \quad (30.9) \end{aligned}$$

$$\begin{aligned} (\rho_6)_{34} \propto & \\ & -1/8\{-K^*(e^{i\omega_1 2t_1} - e^{i\omega_1 3t_1} + e^{-i\omega_2 2t_1} - e^{-i\omega_2 3t_1}) \\ & + K(e^{-i\omega_1 2t_1} + e^{-i\omega_1 3t_1} - e^{i\omega_2 2t_1} - e^{i\omega_2 3t_1})\} \quad (30.10) \end{aligned}$$

$$\begin{aligned} (\rho_6)_{13} \propto & \\ & -1/8\{-K^*(e^{i\omega_1 2t_1} + e^{i\omega_1 3t_1} - e^{-i\omega_2 2t_1} - e^{-i\omega_2 3t_1}) \\ & - K(e^{-i\omega_1 2t_1} - e^{-i\omega_1 3t_1} + e^{i\omega_2 2t_1} - e^{i\omega_2 3t_1})\} \quad (30.11) \end{aligned}$$

$$\begin{aligned} (\rho_6)_{24} \propto & \\ & -1/8\{K^*(e^{i\omega_1 2t_1} - e^{i\omega_1 3t_1} + e^{-i\omega_2 2t_1} - e^{-i\omega_2 3t_1}) \\ & + K(e^{-i\omega_1 2t_1} + e^{-i\omega_1 3t_1} - e^{i\omega_2 2t_1} - e^{i\omega_2 3t_1})\} \quad (30.12) \end{aligned}$$

Similarly, the lower diagonal elements $[(\rho_6)_{21}, (\rho_6)_{43}, (\rho_6)_{31}, \text{ and } (\rho_6)_{42}]$ will also have observable SQ coherences. After this, the data acquisition or detection period, t_2 begins in the L-COSY experiment, during which the digitized signal is recorded as a function of t_2 (direct), similar to conventional 1D MRS. This is repeated several times creating a 2D data matrix in which each row represents a different t_1 (indirect) modulation. The 2D signal acquired by the analog-to-digital converter (ADC) is given by

$$\begin{aligned} s(t_1, t_2) = \text{Tr}[(F_x)\rho_5] \exp(-i\omega_2 t_2) \exp(-t_1/T_2) \\ \exp(-t_2/T_2) [1 - \exp(-TR/T_1)] \quad (30.13) \end{aligned}$$

where ‘Tr’ in the equation (30.13) means the sum over all diagonal elements.

From equations (30.9) through (30.13), it is clear that there is a coherence transfer between A and X, which are J-coupled spins. A 2D Fourier transform (FT) along both the t_1 and t_2 axes will result in a 2D MR spectrum as a function of the two frequency variables (F_1, F_2) described by

$$\mathbf{S}(F_1, F_2) = \iint s(t_1, t_2) dt_1 dt_2 \quad (30.14)$$

The signal acquisition array, $\mathbf{s}(t_2, t_1)$, is the basis of 2D spectroscopy and as discussed in the latter sections of this chapter, the signal acquisition can be extended to further spatial dimensions by adding 2 or 3 spatially encoding gradients to the sequence, thereby enabling multivoxel 2D MRS in a single slice or a three-dimensional (3D) volume.

As discussed by Aue *et al.*,³⁷ the diagonal peaks and cross-peaks can be dispersive and absorptive, respectively, when two hard 90° RF pulses are used to acquire the COSY spectrum. Mixed line shapes in the 2D NMR spectra are typically due to eddy currents (ECs) from the spatial-encoding gradient pulses. Both the diagonal peaks and cross-peaks of an L-COSY spectrum have mixed phases along the F_1 axis, as reported earlier.^{38–40} In contrast to the amplitude modulation in conventional COSY,³⁷ the phase modulation in L-COSY is caused by the evolution of the signal during the gradient pulse before the last 90° RF pulse.^{38–40} A pure-phase L-COSY spectrum can be recorded using a quadrature detection method along the F_1 axis, as described by Brereton *et al.*⁴⁸ This requires two separate P - and N -type spectral acquisitions and recombination of the two datasets, where N and P represent a ‘coherence transfer echo’ and a ‘coherence transfer antiecho’, respectively, selected using different polarities of gradient pulses.^{48–51} As discussed by Keeler,⁵¹ the N stands for ‘negative’, which is due to the coherence order during t_1 being of opposite sign to that along t_2 . In contrast, P stands for ‘positive’ due to the same sign of the coherences during the two spectral dimensions, t_1 and t_2 .

30.2.2 Apodization Filters for 2D L-COSY

The 2D L-COSY spectrum will contain peaks along the diagonal that are similar to those of 1D MRS and cross-peaks connecting multiplets of spins that are J-coupled.^{37,38} The diagonal-peak intensities follow a cosine dependence, and time-domain cross-peak amplitudes increase from zero at the beginning to a maximum at $1/2J$, with the signal decaying according to the inhomogeneously broadened T_2 s (T_2^*). Hence, it is advisable to weight the time-domain signal by a weighting function that de-emphasizes the signal for small t_2 and t_1 values.^{49–51}

As shown in Figure 30.2, optimal matching filters such as a sine-bell (SB) or skewed squared SB can be used along both dimensions for better sensitivity of cross-peaks in the 2D L-COSY spectrum. Use of

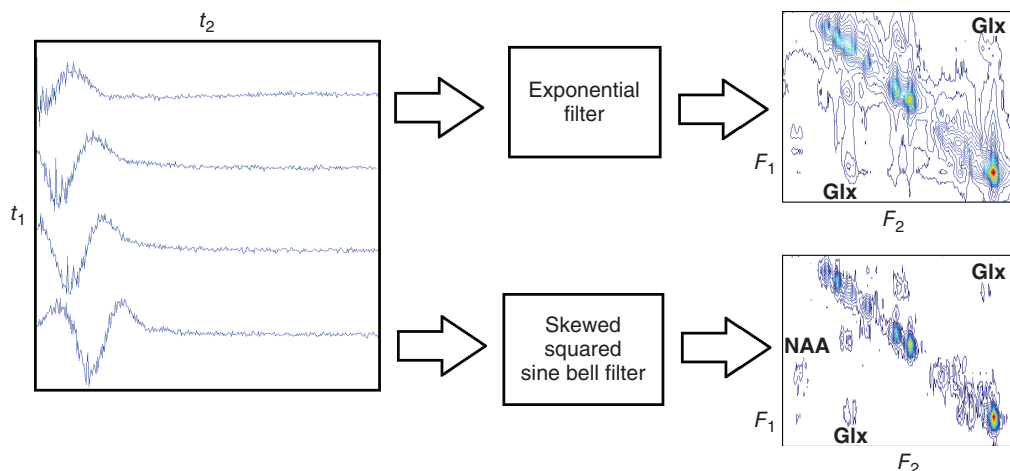


Figure 30.2. Comparison of exponential and sine-bell filters for processing the 2D L-COSY sequence; even though the raw data matrix (t_2 , t_1) contained 100 t_1 signals, only 4 t_1 signals are shown on the left

the skewed squared SB filter instead of a conventional exponential filter for processing the 2D spectrum in Figure 30.2 has three major advantages.⁵² First, unlike the exponential filter, the SB filter begins with a zero value and can emphasize cross-peaks relative to 2D diagonal peaks that are cosine dependent. Second, the SB filter removes broad wings (dispersive components) from 2D magnitude line shapes. Third, truncation errors due to apodization are minimized at the end of the time domain: because of the trailing edge of the SB function, the window function goes smoothly to zero.

30.2.3 Eddy Current (EC) Correction

As shown in Figure 30.1, the 2D L-COSY sequence uses three slice-selective RF pulses combined with spatial gradient pulses. The intense crusher gradient pulses at each side of the second and third RF pulses are used to minimize unwanted coherences arising from imperfect RF pulse refocusing and coherence transfer.^{50,51} As with 1D MRS, 2D MRS is also sensitive to time-dependent frequency shifts that typically last a few milliseconds and that are induced by ECs due to switching the gradients on and off. These affect the first few points of the detected signal array along the t_2 dimension. ECs produce time-dependent magnetic fields that add to the gradient fields and

contribute an EC-related phase to each t_2 signal. In order to calculate an EC-free spectral signal, the phase calculated from an on-resonance signal can be subtracted from the EC-corrupted signal.⁵³⁻⁵⁵ This requires acquisition of two independent L-COSY data matrices⁵⁵: one with water-suppressed (WS) and one without nonwater-suppressed (NWS) water suppression, as depicted in the processing algorithm shown in Figure 30.3.⁵³⁻⁵⁵ Even though multiple signals can be averaged for the WS data, one average typically suffices for the acquisition of the high SNR, NWS data.

Figure 30.4 shows 2D L-COSY spectra acquired from a 27 ml voxel in a phantom containing 21 brain metabolites at physiological concentrations acquired at 3 T, in about 30 min. The WS and NWS time-domain data were processed using the steps shown in Figure 30.3. The EC-uncorrected and corrected L-COSY (WS) data were postprocessed with (i) apodization using shifted squared SB filters applied in both frequency dimensions; (ii) zero filling once or twice along the t_2 and t_1 dimensions; and (iii) a complex fast FT (FFT) along two dimensions. Even though a classical N -type COSY spectrum is presented with the diagonal running from the lower left to upper right corner of the 2D spectral display, owing to the severe asymmetry of cross-peaks in vivo,⁵⁶ our practice is to present the 2D L-COSY spectrum with the diagonal running from the upper left to lower right corner.

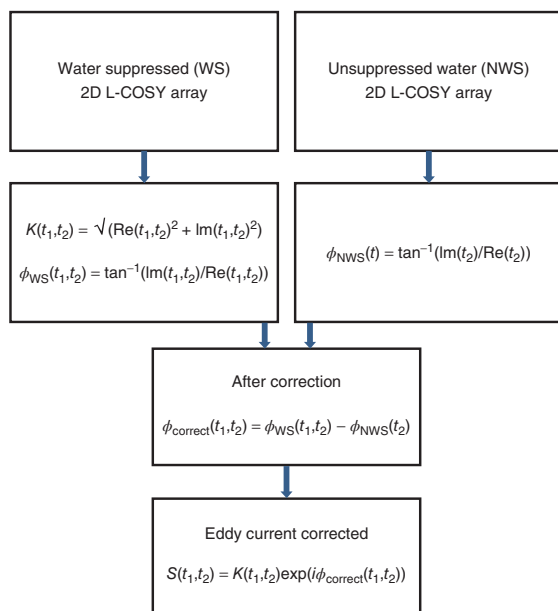


Figure 30.3. Eddy current (EC) correction scheme. Re and Im represent the real and imaginary parts of the complex time-domain signal; ϕ_{WS} and ϕ_{NWS} represent the phase angles calculated from the water-suppressed and water-unsuppressed data sets

Figure 30.4(a) shows the 2D L-COSY spectrum without using the NWS data for EC correction. Using only the first signal ($\Delta t_1 = 0$) from the NWS array for EC correction results in the L-COSY spectrum shown in Figure 30.4(b). Figure 30.4(c) shows the L-COSY spectrum after the EC correction of the WS array using all rows of the NWS array. However, the improvement observed in the phantom following EC correction was minimal in this case, possibly due to less impact of EC on coherence transfer echoes in the 2D L-COSY data. The more significant impact of EC on a multivoxel-based correlated spectroscopic imaging data will be discussed in a latter section.

30.2.4 Localized Spin-echo Correlated Spectroscopy (L-SECSY)

Even though there is no real limitation on the number of complex points along the detected t_2 dimension, the resolution along the F_1 dimension of COSY is dictated by the total number of t_1 increments, which directly affects the acquisition duration. Nagayama

et al. proposed a novel sequence called *spin-echo correlated spectroscopy (SECSY)* in which the incremental delay was equally added before and after the coherence transfer 90° RF pulse. This reduced the number of t_1 increments and spectral width along the F_1 dimension.⁵⁷ Following the same strategy, we presented a second variation of L-COSY, namely localized spin-echo correlation spectroscopy (L-SECSY).⁵⁸ Localized SECSY works the same way as L-COSY (Figure 30.1), except that the second incremental period (Δt_1) after the coherence transfer 90° RF pulse is set the same as the first t_1 evolution period. Compared to L-COSY, the diagonal peaks of L-SECSY lie on ($F_1 = 0$) and the J -cross-peaks are symmetrically disposed above and below the diagonal, falling on a straight line intersecting the diagonal at 45° . The application of 2D L-SECSY was demonstrated in a brain phantom and in healthy human brain at 1.5 T.⁵⁸ Inclusion of t_1 encoding before and after the last 90° RF pulse leads to severe T_2^* weighting. One solution that minimizes this loss is to acquire the data with the t_1 increments before the 90° RF pulse only (similar to 2D L-COSY) and then impose the phase shift for the second t_1 evolution as shown in Figure 30.5. The phase shift is required along the t_1 dimension only, so the 2D array must be Fourier transformed once along the t_2 dimension and the t_1 signals multiplied by a phase factor of $\exp(-2\pi F_2 t_1)$.

Shown in Figure 30.6 are (i) a voxel location on an axial MRI and (ii) the corresponding 2D L-COSY spectrum acquired from a 35-year-old healthy human subject. The 2D L-COSY data were acquired using the same acquisition parameters that were used for the brain phantom in Figure 30.4, and the WS L-COSY array was phase-corrected using the EC correction scheme in Figure 30.3, based on the first row of the NWS data. The 2D L-COSY data shown in Figure 30.6(b) were phase rotated as discussed above (Figure 30.5). Figure 30.6(c) is the resulting 2D L-SECSY spectrum after phase rotation. An advantage of L-SECSY over L-COSY is that a smaller sweep width (1250 Hz vs ± 312.5 Hz) is needed along F_1 .

30.2.5 2D J -resolved Spectroscopy Using PRESS (JPRESS)

Another 2D technique that can be used for improved peak dispersion in the spectral domain is the J -resolved spectroscopy (JPRESS) sequence. This method was initially proposed for high-resolution NMR

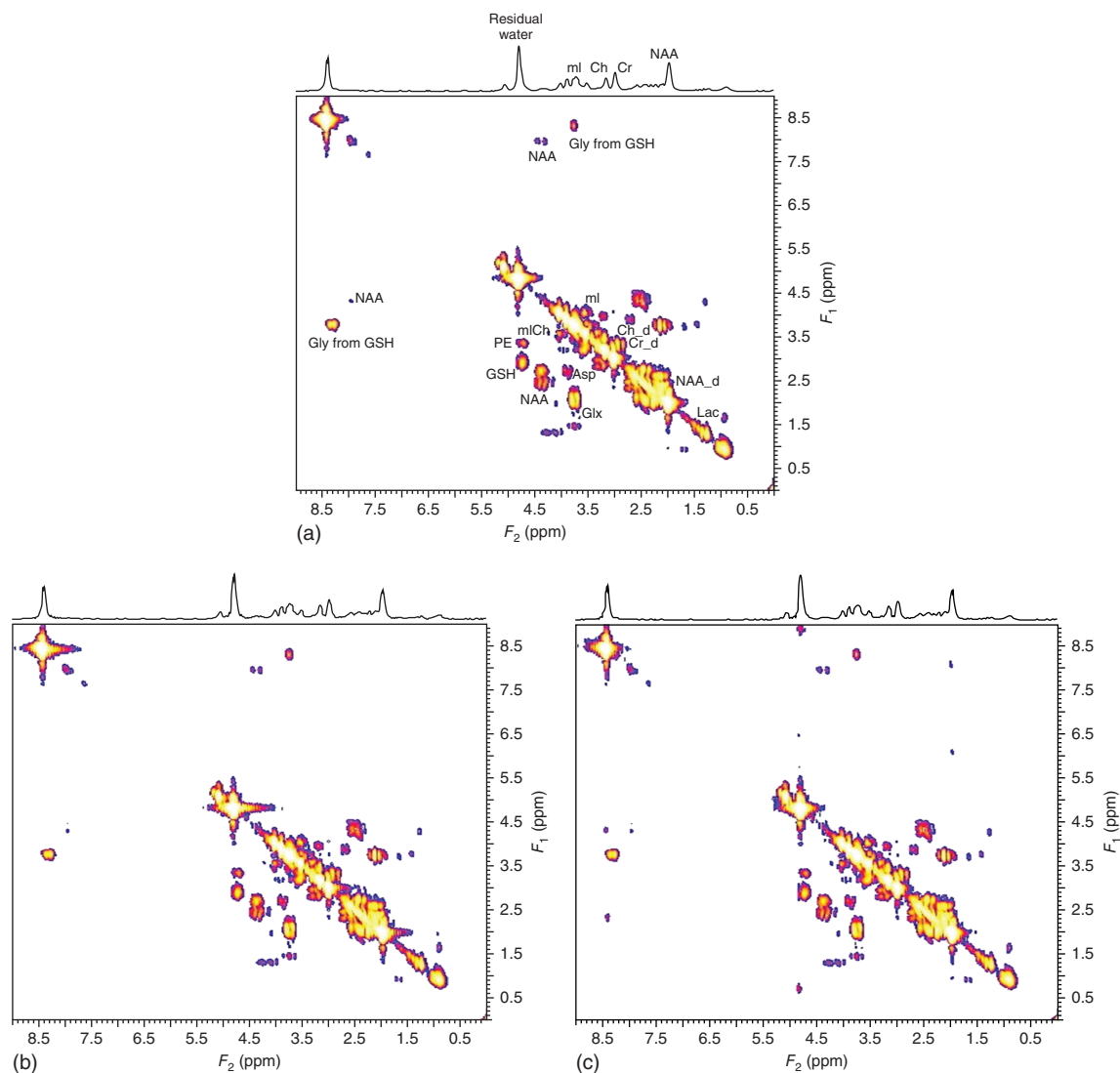


Figure 30.4. 2D L-COSY spectra acquired at 3T from a 27 ml voxel in a phantom comprised of brain metabolites at physiological concentrations. (a) The EC-uncorrected spectrum with water suppression (WS) only. (b) EC corrected with WS using the first row of the non-water-suppressed (NWS) spectrum only. (c) EC corrected with WS using all rows of the NWS data. The phantom comprised: 8.9 mM NAA, 0.7 mM GABA, 2.1 mM aspartate (Asp), 0.9 mM choline (Ch), 7 mM creatine (Cr), 1 mM glucose (Glc), 12.5 mM glutamate (Glu), 2.5 mM glutamine (Gln), 10 mM glutathione (GSH), 4.4 mM myo-inositol (mI), 1.0 mM lactate (Lac), 0.6 mM phosphocholine (PCh), 1.8 mM taurine (Tau), 1.0 mM threonine (Thr), 1 mM phosphoethanolamine (PE), 1 mM lysine (Lys), 1 mM valine (Val), 1 mM leucine (Leu), 1 mM isoleucine (iLeu), 1 mM alanine (Ala), 100 mM formate, 5 mM sodium azide, and 1 mM dimethyl sulfoxide (DSS) in a phosphate buffer solution to maintain pH at 7.2. Acquisition parameters were echo time, TE = 30 ms; sequence repetition time, TR = 2 s; total number of scans = 800; and 100 Δt_1 increments with eight averages/ Δt_1 for WS and one average/ Δt_1 for NWS. Total scan times were 26 min (WS) and 3 min (NWS)

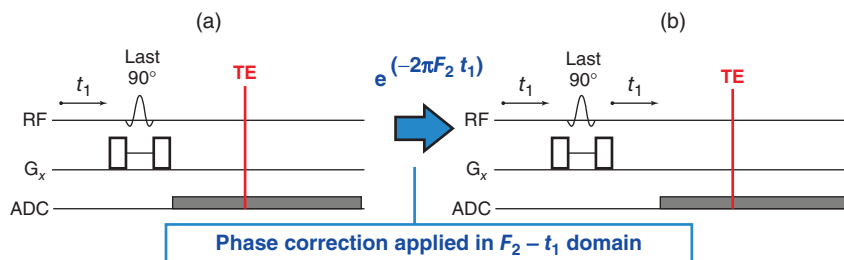


Figure 30.5. (a) Partial 2D L-COSY sequence showing the t_1 increments and 90° RF pulse followed by detection along t_2 . (b) Conversion of the 2D L-COSY sequence into a 2D L-SECSY is depicted

spectroscopy^{49–51}, but has been successfully adapted for in vivo MRS^{31,32,40,59,60} using the PRESS sequence for spatial localization. Accordingly, the new 2D sequence is named ‘JPRESS’.³² Chemical shift information in addition to that of the J-coupling is acquired along the t_2 (detected/direct) dimension, whereas the t_1 (indirect) dimension only contains J-coupling information. Originally, the in vivo JPRESS sequence was developed by adding the t_1 increment before and after the last 180° pulse. Subsequently, the direct dimension was acquired with a half-echo sampling scheme as shown in Figure 30.7(a).^{31,32,40,59,60}

A more efficient way to perform the JPRESS experiment was demonstrated by Schulte *et al.*, also depicted in Figure 30.7.^{34,61,62} This modified JPRESS has two major differences from the earlier version: (i) the t_1 increment is only before the last 180° pulse and (ii) the data acquisition starts immediately after the crusher gradient pulse next to the last 180° RF pulse. This is called a *maximum-echo sampling* scheme (Figure 30.7a). Half-echo sampling starts data acquisition at the echo time (TE), whereas maximum-echo sampling starts collecting data after the last crusher gradient is played out. Maximum-echo sampling has been shown to improve sensitivity compared with the half-echo sampling scheme for JPRESS.^{34,60,61}

As in the reconstruction of L-SECSY from the L-COSY data, a linear phase correction must be applied to the data along the F_2 - t_1 dimension when using the maximum-echo sampling scheme³⁴:

$$\text{Phase correction } (F_2, t_1) \text{ factor} = \exp(-2\pi F_2 t_1) \quad (30.15)$$

where $t_1 = \text{TE} - \text{TE}_{\min}$ and F_2 is the frequency along the direct dimension. This linear phase correction is necessary because each echo needs to be shifted to the same temporal point and is equivalent to adding

a second t_1 increment after the last 180° pulse. However, B_0 inhomogeneity is not refocused using this postprocessing method. A schematic of the linear phase corrections is shown in Figure 30.7(b).

The phase corrections have implications for the spectral bandwidth along the indirect dimension (BW_1). For example, suppose $\Delta t_1 = 1$ ms, so that $\text{BW}_1 = 1000$ Hz (± 500 Hz). After the linear phase correction is applied by adding a second t_1 increment, $\Delta t_1 = 2$ ms and BW_1 is now only ± 250 Hz. This is important to note when designing the maximum-echo sampling experiment. JPRESS has been used for in vivo studies of the human brain,^{31,32,40,59} muscle,³³ prostate,^{60,63} and breast.⁶⁴ Quantitation methods incorporating prior knowledge exist to help fit metabolite peaks that are difficult to identify with traditional 1D (chemical shift) spectroscopy.^{34,36,43} This makes JPRESS a powerful 2D technique for the investigation of different metabolites in vivo.

30.2.6 Apodization Filters for 2D JPRESS

The J-coupled multiplets are better resolved along the indirect t_1 dimension than in the detected t_2 (direct) dimension, as any defocusing linear B_0 interactions including the static field inhomogeneity during the first half of t_1 are refocused during the second half, resulting in a net zero dependence on the B_0 inhomogeneity and other static field interactions. Even though this is a major advantage, the phase-modulated time-domain datasets are transformed into phase-twisted 2D peaks after the double FFT of the 2D JPRESS raw data. Hence, the squared or simple SB filter functions described in Section 30.2.2 can be used before the double FFT.

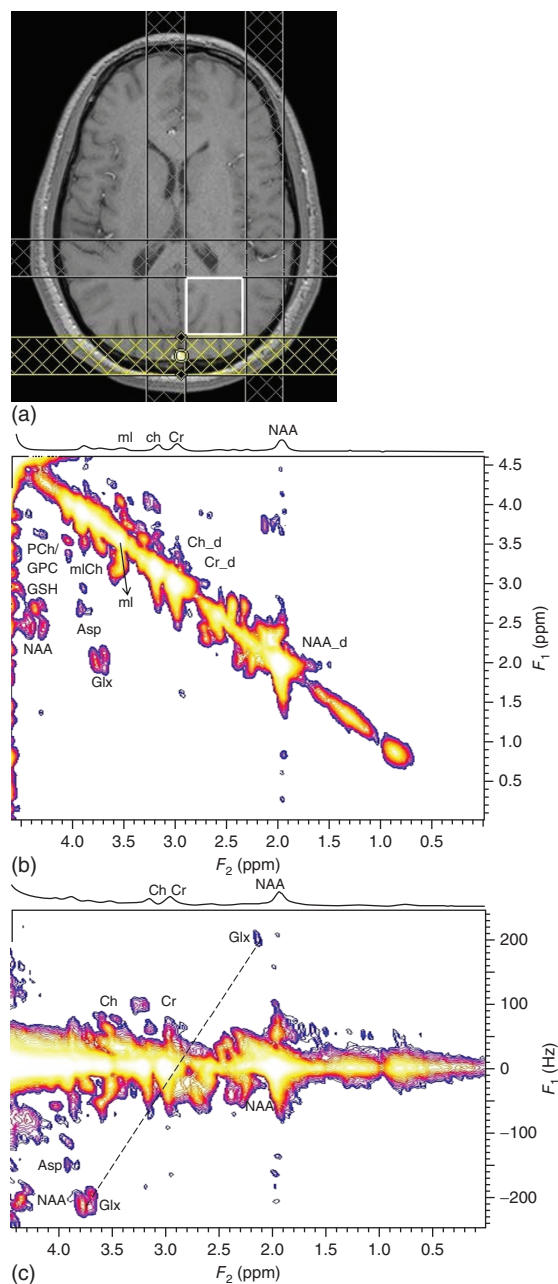


Figure 30.6. 2D L-COSY spectrum acquired from a 35-year-old healthy human subject: (a) Axial MRI slice showing the voxel location. (b) Water-suppressed (WS) L-2D COSY spectrum using only the first row of the non-WS (NWS) data for EC correction. (c) Conversion of the 2D L-COSY data from (b) into 2D L-SECSY, after phase rotating the data (Figure 30.3)

30.2.7 Strong Coupling Effects in 2D JPRESS

One of the advantages of JPRESS over L-COSY is that the chemical shift and any linear interaction are refocused during the t_1 dimension while the J -interaction remains unrefocused. At 3 T or lower B_0 , this assumption is applicable only for weakly coupled metabolites such as lactate, alanine, and glycine. Most other metabolites have strongly coupled protons where J -coupling is equal to or larger than their chemical shifts ($\delta < J$). Hence, the refocusing 180° RF pulse at the center of the t_1 evolution does not refocus all chemical shifts and results in more cross-peaks. It has been demonstrated earlier that 2D JPRESS spectra of brain and prostate metabolites contain more cross-peaks than those of weakly coupled ones.^{32,60}

30.2.8 Adiabatic COSY and JPRESS

One of the limitations of in vivo MRS/MRSI using conventional RF pulses performed at 3 T or higher fields is the chemical shift displacement error (CSDE),^{65–67} defined as the difference in the location of the center of the excitation or refocusing slices of two resonances with a different chemical shift (see Chapter 7). With NMR signal excitation using large body coils, the bandwidths of conventional refocusing RF pulses, such as optimized 180° pulses,⁶⁸ become quite small. As the chemical shift increases with B_0 , the CSDE at 3 T and higher fields can become very large, if ignored.

A second problem with MRS/MRSI using conventional RF pulses is the difficulty of achieving a uniform RF transmit (B_1) field, leading to poor slice-selection profiles. Accurate volume selection using slice-selective RF pulses is a prerequisite for proton (^1H) MRSI of the brain in order to exclude contamination by large lipid signals from the skull and/or water signals from poorly shimmed regions outside the selected volume. Owing to inhomogeneous transmit B_1 fields, flip angles may vary inside the voxel, causing not only signal loss but also an increase in the side lobes of the slice profile, leading to nonzero flip angles outside the selected volume.^{69,70} In addition, when strongly coupled spin systems are observed in spin-echo experiments, the spectral shape of the corresponding signals can vary, depending on the local flip angle of the refocusing pulses.⁷¹ JPRESS-localized MRSI also has the complication of unreliable spectra at the edges of the PRESS box due

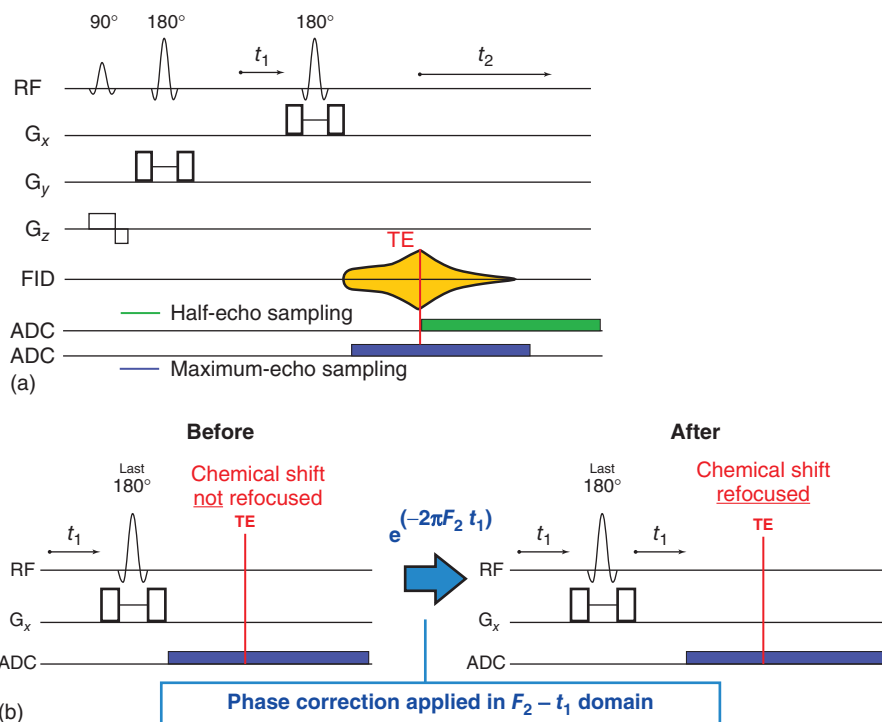


Figure 30.7. (a) A schematic for a JPRESS sequence utilizing maximum-echo sampling for acquisition (highlighted in gold; FID; ADC, analog-to-digital converter). Half-echo sampling is started exactly at the echo time (green), whereas maximum-echo sampling starts immediately after the last crusher gradient (blue). The number of t_2 points sampled using each method is the same. (b) The effects of adding a linear phase correction to refocus the chemical shift information. The linear phase acts as if a second t_1 increment is added after the last 180° pulse. The linear phase correction effectively halves the spectral bandwidth in the indirect dimension

to the imperfect slice profiles of the 180° pulses. All of these limitations and potential artifacts apply equally to L-COSY and JPRESS. In addition, the efficiency of coherence transfer echoes may suffer when the 90° RF pulses are inhomogeneous, resulting in suboptimal cross-peaks in L-COSY.

These shortcomings can be addressed using adiabatic pulses, as they have relatively high bandwidths, and their flip angles are insensitive to transmit B_1 inhomogeneities, as demonstrated by Garwood and Delabarre.⁶⁵ Adiabatic-refocusing pulses have sharp slice-selection profiles to produce a localized Hahn spin echo. The adiabatic excitation or refocusing pulses have been implemented in techniques such as ‘LASER’ (localization by adiabatic selective refocusing)^{66,72} and its simplified version semi-localization by adiabatic selective refocusing (sLASER; see Chapter 7).^{66,67} The sLASER sequence consists of a conventional nonadiabatic 90°

slice-selective pulse and two pairs of adiabatic hyperbolic secant (HS) pulses for refocusing. While some insensitivity to B_1 inhomogeneity is lost, the sLASER sequence has reduced RF power and can achieve shorter TEs than LASER. For pulse spacing that is short compared to the reciprocal of the J-coupling and the chemical shift bandwidth, J-coupling losses will generally be minimal despite short echo times and can be neglected.⁷³ The two adiabatic RF-refocusing pulse pairs can reduce antiphase coherence that results from J-coupling and has been shown to improve the spectral shape of coupled spin systems at 3 T.⁶⁷ With the small CSDE and sharp-selection profiles of the adiabatic-refocusing pulses, the VOI can be positioned close to the skull, while largely avoiding contamination from subcutaneous lipid signals from outside the voxel.

Ramadan *et al.* implemented an adiabatic localized correlated spectroscopy (AL-COSY) in which the

VOI was localized by a 90° nonselective adiabatic RF pulse for excitation followed by two pairs of adiabatic HS RF pulses for refocusing and a terminal 90° RF sine pulse for the coherence transfer.⁷⁴ Compared to L-COSY using nonadiabatic 90° and modified Mao⁷⁴ 180° RF pulses, chemical shift artifacts were reduced with AL-COSY and slice profiles of adiabatic pulses were found to be sharper and more symmetrical than those obtained with conventional Mao pulses.⁶⁸

Another adiabatic version of L-COSY was proposed by Lin *et al.*⁷⁵ They showed that an 'sLASER-first-COSY' sequence yielded stronger cross-peaks and higher ratios of cross-peak volumes to diagonal-peak volumes than the 'sLASER-last-COSY' sequence in which the nonselective hard 90° coherence transfer RF pulse is replaced by a slice-selective 90° RF pulse. In addition, these authors presented two adiabatic versions of JPRESS: the first used three pairs of adiabatic pulses for voxel localization for *J*-resolved LASER and the second used two pairs of 180° RF pulses in sLASER.⁷⁶ The first half of the t_1 period was inserted between the last pair of adiabatic pulses, to record 2D *J*-resolved spectra in phantoms and human brain. Significant advantages over conventional JPRESS were demonstrated. These were that: (i) the *J*-resolved LASER and sLASER sequences exhibited better suppression of both chemical shift artifacts and additional *J*-refocused peaks that arise from spatially dependent *J*-coupling evolution; and (ii) they were relatively insensitive to RF frequency offset over a large bandwidth. However, there were also a few drawbacks: the adiabatic versions had higher RF power specific absorption rates (SARs) and slightly longer TE compared to the basic versions of L-COSY and JPRESS.

30.3 ECHO-PLANAR CORRELATED AND *J*-RESOLVED MRSI

30.3.1 MRSI/Echo-planar Spectroscopic Imaging

Depending on the desired spatial resolution, traditional 2D or 3D MRSI²⁵⁻²⁷ with conventional CSI phase-encoding schemes generally lead to intolerable scan times. To sample a 3D volume with numbers of phase-encoding steps N_x , N_y , and N_z along all three spatial dimensions (x , y , z), with a repetition time TR, and number of averages per frame of N_{AV} , requires a total measurement time of $N_x \times N_y \times N_z \times TR \times N_{AV}$.

Thus, for a simple 3D CSI acquisition with an N_{AV} of 1, a spatial matrix size of $16 \times 16 \times 8$, and TR = 2 s, the total scan time will be more than an hour. Although all of the gradient phase-encoding steps contribute to the SNR, if the MRSI scan requires multiple averages to achieve adequate SNR, or longer TRs to avoid saturation effects, the resultant total acquisition time can easily render clinical applications impractical. In such scenarios, integrating multivoxel spatial-encoding techniques with multidimensional sequences, such as L-COSY and JPRESS that require extra spectral dimensions, results in MRSI sequences that are even less clinically feasible. Hence, novel MRSI techniques with reduced scan times are essential for implementing 2D and 3D spectroscopy in the clinic.

Different methods of performing MRSI that avoid discrete phase-encoding gradients in one or more dimension have been developed and implemented to address this time constraint. In 1983, Mansfield^{77,78} proposed the use of an echo-planar readout gradient to simultaneously acquire one spatial and one spectral (temporal) dimensions during a single readout. That approach had the potential to greatly shorten the acquisition of 2D and 3D MRSI data, but owing to implementation issues with the gradients⁷⁹ at that time, it took an extra decade until 1994 when Posse *et al.*^{80,81} implemented the first clinically applicable proton echo-planar spectroscopic imaging (PEPSI) protocol, also known as echo-planar spectroscopic imaging (EPSI)⁸¹ (see also Chapter 12). In EPSI, a time-varying readout gradient is employed to frequency encode the same line in *k*-space repeatedly, so that the spatial information is collected as a function of time. In this way, phase encoding of that spatial dimension is not needed. The remaining spatial dimensions are phase-encoded sequentially, similar to spin-echo MRI, resulting in an acceleration of N_x times if the frequency encoding is performed along the *x*-direction, say. Such an acceleration by over an order-of-magnitude in total scan time makes it feasible to acquire spatially resolved multidimensional MRS data in a clinical setting,⁸² collect 3D data sets,⁸² or increase spatial resolution.

Four-dimensional (4D) echo-planar correlated spectroscopic imaging (EP-COSI) and echo-planar *J*-resolved spectroscopic imaging (EP-JRESI)⁸³⁻⁸⁵ sequences combine the speed advantage of the EPSI readout with the increased spectral dispersion offered by 2D L-COSY/JPRESS, enabling collection of better-resolved 2D spectra from multiple regions. The EPSI readout acquires one spatial (k_x) dimension and

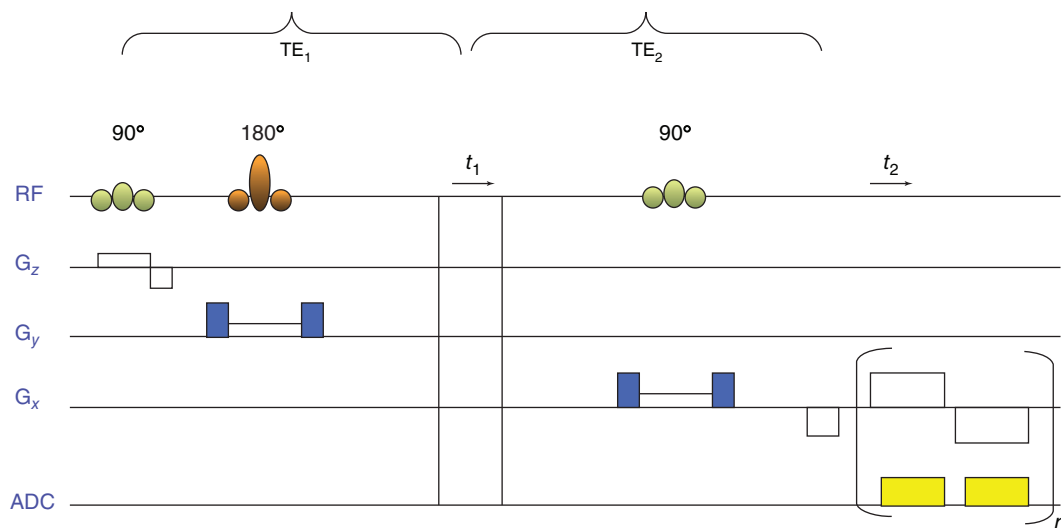


Figure 30.8. A schematic diagram of a 4D EP-COSI sequence

one temporal (t_2) dimension simultaneously, leaving the remaining spatial and spectral dimensions (k_y and t_1 , respectively) to be recorded incrementally. This can reduce total scan time to around 20 min. In contrast, if one were to use conventional phase-encoding gradients (16×16) in combination with an L-COSY or JPRESS ($2048 t_2$ and $100 t_1$) sequence, the total acquisition time with TR of 2 s will be longer than 14 h.

30.3.2 4D Echo-planar Correlated Spectroscopic Imaging (EP-COSI)

A 4D EP-COSI sequence is shown in Figure 30.8, using two spatial encodings (k_x and k_y) and two spectral dimensions (t_2 and t_1). The sequence uses a 90° – 180° – 90° scheme for localizing the VOI with crusher gradients surrounding the refocusing 180° and coherence transfer 90° RF pulses. The crusher gradients ensure that magnetization outside of the VOI is dephased and does not significantly contribute to the acquired signal. The ‘ n ’ subscript along the ADC and G_x axes in Figure 30.8 represents the total number of echo-planar readout pairs (positive and negative) that result in the desired number of t_2 spectral points. TE_1 and TE_2 are the echo times for the first and the second echoes and $TE = TE_1 + TE_2$. As already noted, by utilizing the EPSI readout to acquire the k_x and t_2 data simultaneously, the total duration

of the EP-COSI scan time is reduced N_x -fold. The second spatial dimension (k_y) is encoded using phase encoding, and the indirect temporal dimension (t_1) is acquired by incrementing the evolution time between the 180° and final 90° RF pulses by Δt_1 . Some typical parameters for a 4D-EP-COSI experiment on a 3 T scanner include $k_x = 32$ (with oversampling), $k_y = 16$, t_2 points = 256, $\Delta t_2 = 0.84$ ms, t_1 points = 64, $\Delta t_1 = 0.8$ ms, TE = 30 ms, and TR = 1500 ms.

30.3.3 Echo-planar J -resolved Spectroscopic Imaging (EP-JRESI)

Replacing the second 90° slice-selective RF pulse in Figure 30.8, with a slice-selective 180° yields the 4D EP-JRESI sequence. As this sequence uses an EPSI readout as well, the acceleration factor remains N_x times a conventional 3D CSI. This sequence has the same advantages that JPRESS has over 2D L-COSY, mainly due to improved sensitivity as a result of refocusing the spin echo. Similar to 4D EP-COSI, the typical parameters for a 4D EP-JRESI experiment on a 3 T scanner include $k_x = 32$ (with oversampling), $k_y = 16$, t_2 points = 256, $\Delta t_2 = 0.84$ ms, t_1 points = 64, $\Delta t_1 = 1$ ms, TE = 30 ms, and TR = 1500 ms. The main difference between the two sequence parameters is that a spectral bandwidth of 1000 Hz is used for the indirect dimension in EP-JRESI, whereas EP-COSI

uses a spectral bandwidth of 1250 Hz for the indirect dimension. Of course, after phase corrections to account for the maximum-echo sampling scheme as described above, each 2D J -resolved spectrum that is extracted from the 4D EP-JRESI data will have a spectral bandwidth of ± 250 Hz along the indirect spectral dimension (t_1), as discussed in Section 30.2.5. On the basis of the organ (prostate, brain, etc.) under investigation, scan parameters typically including the t_1 points, TE, and TR may need to be adjusted.

30.3.4 Postprocessing of the 4D EP-COSI/EP-JRESI Data

Reconstruction of 4D EP-COSI and EP-JRESI data sets is performed offline using custom MATLAB software macroroutines. Details for the reconstruction are provided in Figure 30.9. The center of the k -space is traversed repeatedly with a constant time interval in an ideal EPSI readout. Alternating readout gradients result in opposing directions for the trajectories along k_x . Hence, the odd/even echoes must be temporally reversed and the reversal of odd echoes translates this temporal shift in the echo train into a relative misalignment along k_x between the odd and even echoes. This misalignment generates spectral ghost artifacts when the echoes are combined. Echo misalignment due to the sample itself may be due to background gradients resulting from improper shimming, local susceptibility-induced inhomogeneity, and ECs.⁸⁶ These effects will produce additional phase

and magnitude discontinuities between the echoes that generate spectral artifacts.

One widely used and effective method to tackle the ghost peaks is to separate the odd and even echoes in data processing. This method sacrifices half of the spectral bandwidth: however, sufficient bandwidth is typically retained to maintain the 10 ppm necessary at 3 T. When a limited bandwidth is problematic, Karczmar and coworkers have developed a method for combining the odd and even echoes that will maintain the spectral bandwidth and reduce spectral ghosts.⁸⁷ Both the reference NWS scans and WS scans have to be first separated into even and odd subsets and reorganized into $k_x - k_y - t_2 - (t_1$ for WS only) matrices. In order to reduce the total scan time, NWS scans are taken with only a single t_1 point, which makes a 3D total data matrix, so only the WS matrix is 4D. Skewed squared SB apodization filters can be used to improve the spectral sensitivity as well as resolution.^{37-39,52} Both data sets will then be subjected to 3D and 4D FFT reconstruction to produce two $x-y-F_2-(F_1$ for WS only) data matrices. The NWS EP-COSI/EP-JRESI data are used to determine the spatially-dependent resonant frequency shifts owing to local B_0 inhomogeneities and ECs from gradient switching. The corrections can be measured as the drift from the central frequency of the main water resonance, and compensated for by shifting the associated spectra of the WS EP-COSI/EP-JRESI data set. The even and odd echoes are combined by adding the complex subsets followed by FFT along the t_1 dimension.

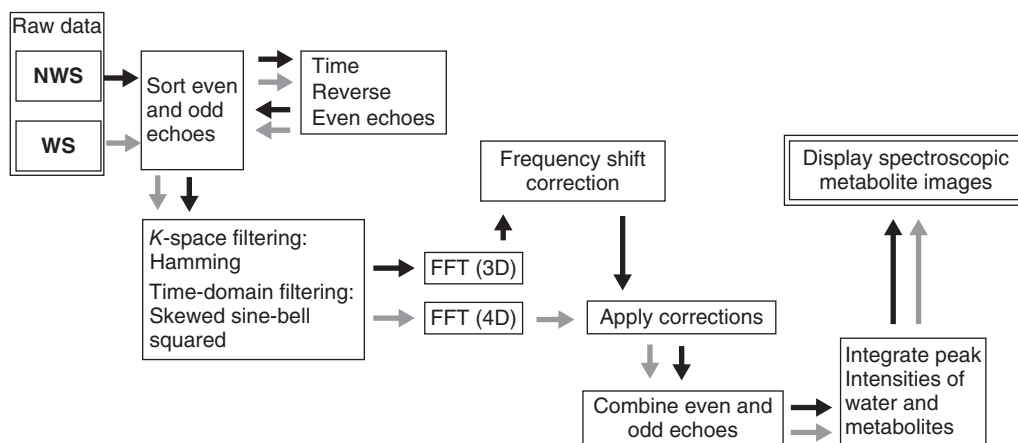


Figure 30.9. Reconstruction of the 4D EP-COSI/EP-JRESI datasets

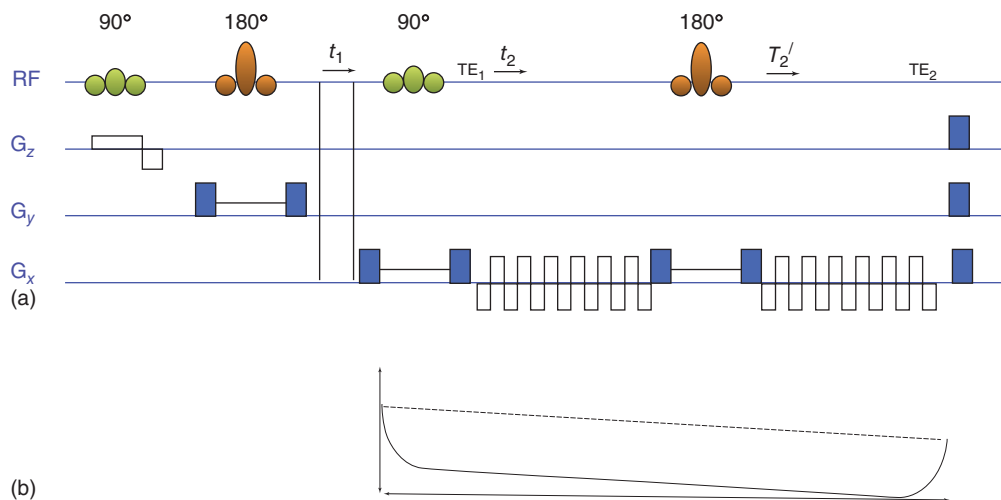


Figure 30.10. (a) The MEEP-COSI Pulse sequence diagram. (b) Diagram showing the effect of both T_2 (dashed line) and T_2^* (solid line) on the overall shape of the signal envelope

30.3.5 Multiecho Echo-planar Correlated Spectroscopic Imaging (MEEP-COSI)

To record a turbo spin-echo (TSE) or fast spin-echo (FSE) MRI,^{88–90} multiecho (ME)-encoding schemes have been used to reduce the overall scan duration dramatically. Similar ME-based techniques have shown greatly reduced scan times in MRSI and their applicability has already been demonstrated in 1D spectral-based MRSI, EP-JRESI, and correlated spectroscopic imaging^{91–95} studies. A two-echo-based multiecho echo-planar correlated spectroscopic imaging (MEEP-COSI)⁹⁶ sequence (Figure 30.10) enables further acceleration (2×) of the EP-COSI sequence with only half of the acquisition time. In contrast to the 4D EP-COSI sequence, the 4D MEEP-COSI sequence refocuses the decaying magnetization during the initial readout train with a 180° RF pulse and samples a differently phase-encoded k -space line as the magnetization grows back until TE_2 during the second readout train within the same repetition time. The initial phase-encoding gradient is combined with the final spoiler gradient before the echo-planar readout. Following the first echo-planar readout (t_2), the initial phase encoding is reversed just before the 180° pulse, whereupon a different line in k -space is phase encoded after the 180° pulse.

Compared to the EP-COSI sequence, the repeated bipolar readout gradient creates two different sets

of k -space trajectories that result in mirror images in real space. These two different sets of echoes can be summed together by time-reversing the even-numbered gradient echoes to create a single image. In a typical MEEP-COSI scan, 256 bipolar-gradient echo pair spectral signals are collected for each EPSI readout, yielding 256 t_2 points. 50 t_1 points are incrementally collected resulting in a scan time of 10 min, which is twice as fast as EP-COSI (20 min).⁹⁶

30.3.6 Multiecho Echo-planar J -resolved Spectroscopic Imaging (MEEP-JRESI)

Furuyama *et al.*⁹³ first implemented the ME-based echo-planar spectroscopic imaging (ME-EPSI) on a 3 T MRI scanner and showed its application in human brain. Sarma *et al.*⁹⁵ modified the ME-EPSI sequence to implement ME-based echo-planar J -resolved Spectroscopic Imaging (MEEP-JRESI) in the human brain. At the core of the MEEP-JRESI sequence is the JPRESS module. To accelerate the acquisition, it employs two bipolar EPSI readouts separated by a slice-selective refocusing 180° pulse. After the last localization pulse, the first EPSI readout samples the magnetization starting at echo time, TE_1 . After the completion of the first EPSI readout, the initial phase encoding is reversed, and the decaying magnetization

during the first readout train is refocused using the slice-selective 180° pulse. Subsequently, the second EPSI readout is used to measure the magnetization phase encoded to another line in k -space. In this way, two phase-encoding steps are accomplished within the same TR. A more detailed discussion on the implementation of multiecho, its effect on the point-spread function (PSF), and postprocessing steps to combine the two EPSI readouts can be found elsewhere (see also Chapter 12).⁹³

A limiting factor for ME-based spectroscopic imaging is the T_2 decay, which diminishes the signal with each echo, and presents a potential problem in living tissue where T_2 relaxation times are shorter. This can be addressed by keeping the time between the different echoes as short as possible, although this limits the overall spectral resolution. Sarma *et al.* and Rajakumar *et al.* have successfully implemented the ME-EP-JRESI method in human brain and prostate, respectively.^{95,97}

30.3.7 Data Processing of 4D MEEP-COSI/MEEP-JRESI

Reconstruction of the ME-EP-COSI/MEEP-JRESI data sets is done offline using a custom MATLAB software package as shown in Figure 30.11. Because of the opposite directions of the trajectories along k_x caused by the alternating readout gradients, the odd (or even) echoes must be reversed during data processing for reasons discussed in Section 30.3.4. Both the reference and water-suppressed scans will first be separated into positive (even) and negative (odd) subsets and reorganized into x - y - t_2 -(t_1 for WS only) matrices. The reorganized spectral points will be interpolated to 1024 points using zero filling in the time domain (t_2). A skewed squared SB apodization filter can be used to reduce contamination from extra-voxel signals due to the imperfect PSF in both the non-water-suppressed and water-suppressed scans. Both data sets will then be subjected to 3D FFT reconstruction to produce two x - y - F_2 -(F_1 for water suppressed only) data matrices.

30.3.8 Necessity of EC Correction in EP-COSI/EP-JRESI

As discussed in Section 30.2.3, the ECs can cause distortions in the spectra after FT and these distortions can

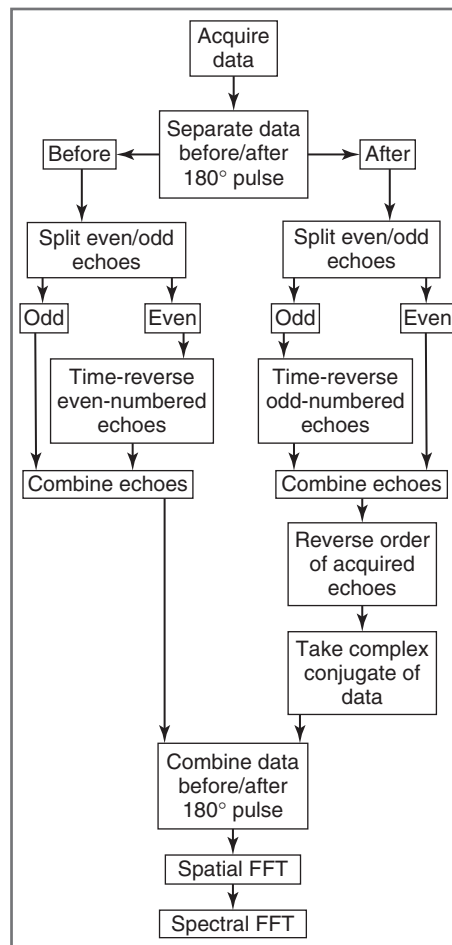


Figure 30.11. Different steps for postprocessing the MEEP-COSI/MEEP-JRESI datasets

be corrected in the WS scan using the phase differences measured from an NWS reference scan.^{53–55} With the use of an EPSI readout, EC effects are greatly amplified and separate water reference scans or interleaved water reference scans are the norm for 1D spectroscopic imaging.^{80,98} This is also the case when acquiring two spectral dimensions for spectroscopic imaging.

A pseudo 4D EP-COSI data recorded in a gray matter brain phantom (see Figure 30.4 caption) is considered here, using a sequence employing frequency encoding (k_x) only with one phase-encoding gradient along the other spatial dimension ($\Delta k_y = 0$) on a 3 T scanner. In this experiment, several columns are acquired instead of individual voxels in order to see the

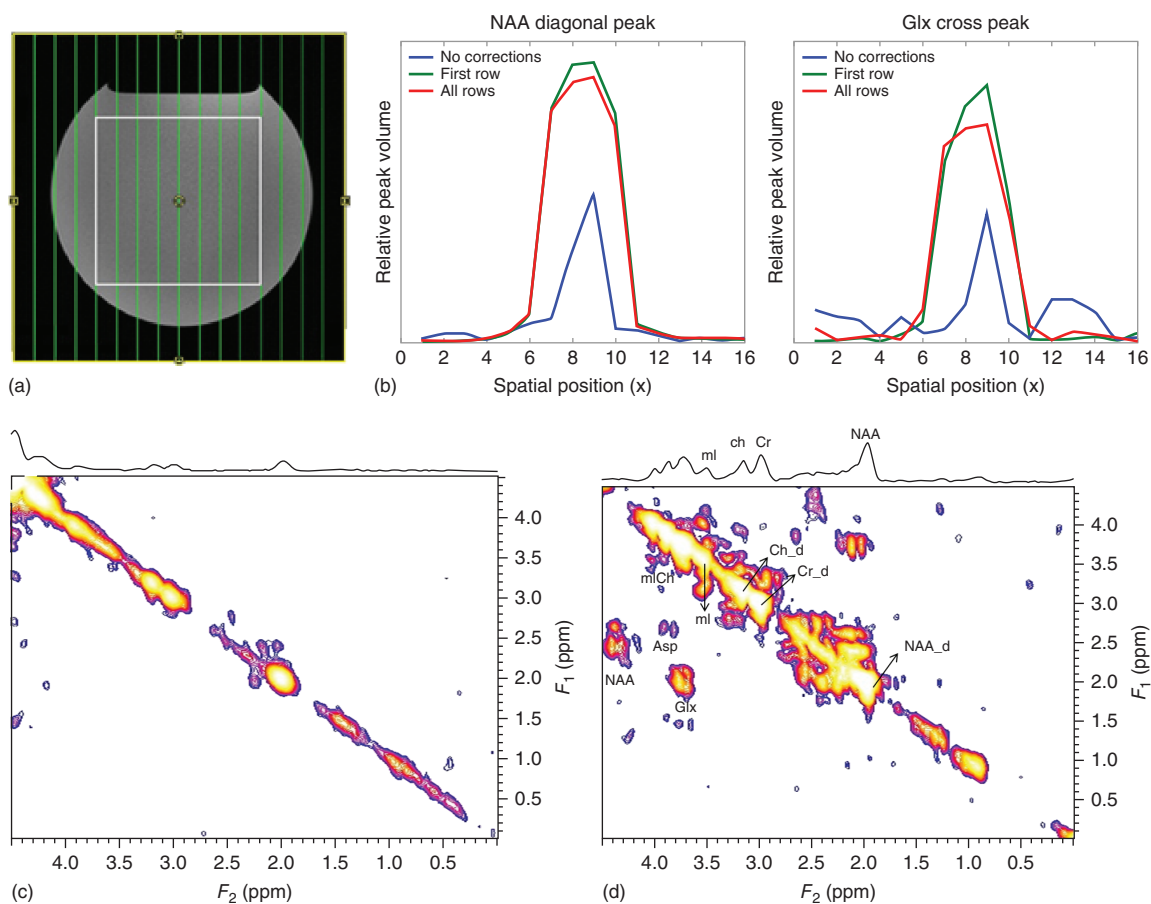


Figure 30.12. (a) Axial MRI of a phantom showing 16 vertical grids for EP-COSY with only one phase-encoding step ($\Delta k_y = 0$). (b) 1D spatial profiles of the NAA diagonal peak at 2 ppm (left) and glutamate/glutamine (Glx) cross-peaks (right) after postprocessing the EP-COSY data with and without EC corrections. The three colored curves represent three postprocessing methods: no EC corrections are applied (blue), EC corrections are applied only using the first NWS row (green), and EC corrections are applied using all t_1 NWS rows (red). (c) Extracted 2D COSY spectra from one of the columns without and (d) with EC (Klose's) correction

effects of the EC, as discussed in Section 30.2.3, on the spatial profile as evident in Figure 30.12(a). A reference NWS scan is also obtained with the same parameters. After data acquisition, the data are post-processed in three different ways as discussed earlier (Figure 30.3): (i) using no corrections to the NWS data; (ii) using the first t_1 point for the EC⁵³; and (iii) using all the t_1 points for EC correction. The difference between the second and third methods is that the second method does not correct the phase differences line by line, but instead uses the phase difference from the first line ($\Delta t_1 = 0$) and applies these changes to all successive lines ($\Delta t_1 > 0$). The second method is useful

because an NWS scan with only a single t_1 point is necessary to perform the corrections, which greatly reduces scan time.⁵⁵

Figure 30.12(b) shows the spatial profile along the echo-planar readout direction for the NAA diagonal peak as well as the Glx cross-peak. It is clear that not only the amplitudes of the diagonal peak and cross-peaks are affected by the EC, but the spatial profile as a whole is distorted too. It is interesting to note that the second correction method gives almost similar results to the third correction method and implies that the EC corrections do not greatly vary from t_1 point to t_1 point. Spectral quality of a central voxel

($x=9$) is also greatly enhanced after the EC corrections, which can be seen by comparing the differences in Figure 30.12(c) and Figure 30.12(d). Without any corrections, the Glx and NAA cross-peaks are not qualitatively noticeable, whereas after corrections, the cross-peaks are apparent. Therefore, it is recommended that when performing multidimensional spectroscopic imaging (with 2 spectral + spatial dimensions), an NWS scan should be acquired with $\Delta t_1 = 0$ to use for EC corrections for higher spatial and spectral quality.

30.3.9 Application of 4D MEEP-JRESI in Human Brain

Sarma *et al.*⁹⁵ showed the feasibility of implementing MEEP-JRESI on human brain at 3 T. Figure 30.13 shows selected 2D J -resolved spectra extracted from a 4D MEEP-JRESI data set acquired from the mid-occipital and left temporal region of a healthy 59-year-old human brain. The peaks were localized within the PRESS excitation volume (Figure 30.13a; white box) with minimal leakage. 2D J -resolved spectra extracted from voxels in the left temporal and mid-occipital regions (Figure 30.13a; yellow and blue boxes) are shown in Figure 30.13(b) and (c). Both in the occipital and temporal lobes, Sarma *et al.* were able to quantify many metabolite resonances reliably, including cross-peaks due to J -coupling not observable with 1D MRS. In addition to the major metabolites, their results indicate stable estimation of important but minor metabolites such as Gln, Asp, PE, GSH, GABA, and Lac, which is particularly promising if it can allow a more accurate and reliable investigations of the roles these metabolites play in normal and disease states.

30.3.10 Evaluation of EP-COSY and MEEP-COSY in Calf Muscle

There has been significant attention focused on the relationships between lipid composition within the skeletal muscle and insulin sensitivity, diabetes and obesity. Determination of muscle triglycerides was classically only possible by invasive techniques.^{99–102} In vivo spectra have been recorded in different regions of human skeletal muscle using SV 1D MRS with the VOI in the soleus, anterior tibialis, and other muscle regions, using the PRESS or STEAM SV

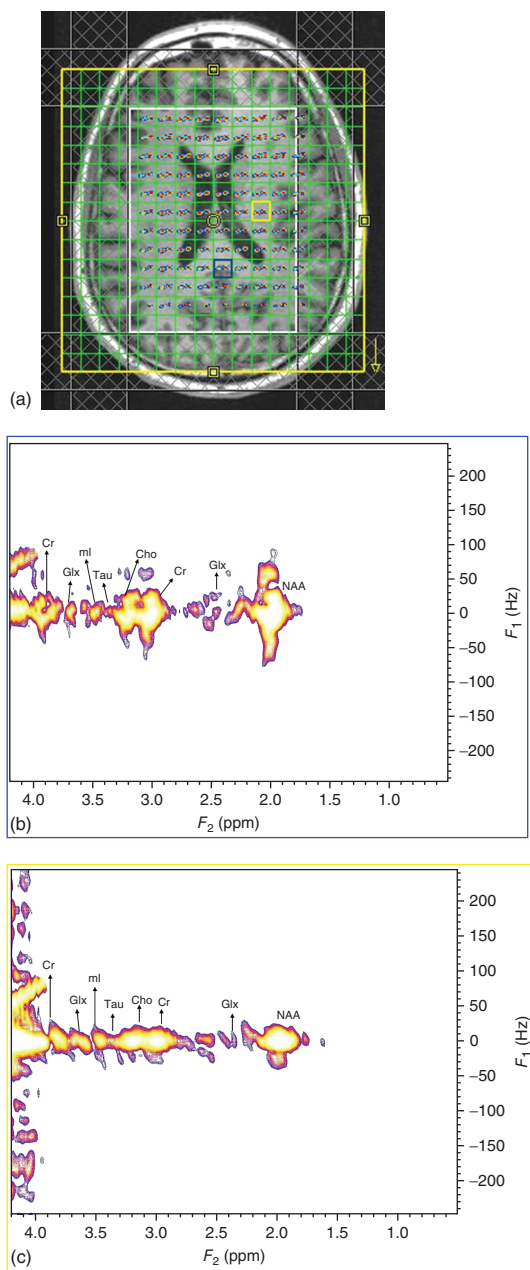


Figure 30.13. (a) Multivoxel spatial distribution of 2D diagonal peaks of Cr and Cho (3.0 and 3.2 ppm) overlaid on a T_1 -weighted axial MRI. The white box indicates PRESS inner-volume localization, with voxels in the mid-occipital and left temporal lobes highlighted in blue and yellow, respectively. (b) Selected 2D J -resolved spectra extracted from the mid-occipital and (c) left temporal voxels

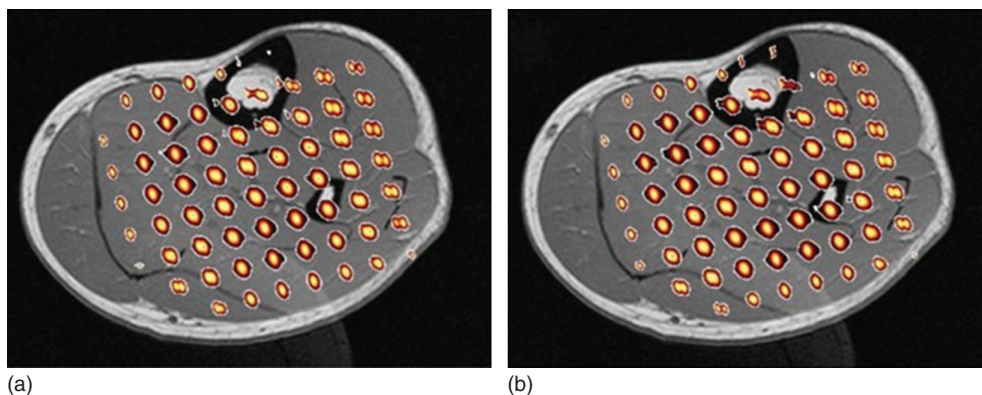


Figure 30.14. Comparison of the performance of the (a) MEEP-COSY and the (b) EP-COSY sequences in the calf of a healthy 28-year-old male volunteer. Spatial projections of the creatine diagonal peak at 3.9 ppm are overlaid on top of T_1 -weighted axial MRI. (Reproduced with permission from Ref. 96. © John Wiley & Sons, Ltd., 2014)

sequences.^{99,102–110} Spatially resolved MRS techniques enable quantitation of several metabolites including Cr, Cho groups, carnosine, etc. as well as intramyocellular lipids (IMCLs) and extramyocellular lipids (EMCLs).

As the IMCLs in muscle cells are stored in spheroid droplets adjacent to mitochondria, their proton density and concentration is larger than EMCLs, which are distributed over large regions of muscle fascia. Thus, the signal strength of IMCL is fairly constant, while the signal strength of EMCL may be affected by even a slight translocation of the voxel, so the challenge has been to develop appropriate, spatially efficient techniques that yield reproducible results. Li *et al.*¹⁰⁹ have compared MRSI and SV-MRS such as PRESS and STEAM techniques at 3 T and found that 2D MRSI showed better reproducibility for IMCL quantification than SV-MRS. It was also shown that both MRSI and SV-MRS methods have good reproducibility for measuring IMCL *in vivo*, but that MRSI offered greater flexibility, reliability, and higher sensitivity to IMCL differences, whereas a shorter scan time was possible with SV-MRS.¹⁰⁹ However, there is significant spectral overlap between the methyl groups of the saturated and unsaturated lipid signals in 1D MRS, which makes it difficult to distinguish and quantify these groups. In contrast, 2D L-COSY can clearly resolve the saturated and unsaturated peaks of IMCL and EMCL as well as those of metabolites such as Cr, Cho, and carnosine. This technique can provide a quantitative measure of the ratios of IMCL and EMCL, and saturated and unsaturated lipids *in vivo*.^{44,83,111,112}

A major drawback of the SV-based 2D L-COSY^{44,111,112} technique is that a larger voxel size (e.g., 27 cm³) and longer acquisition time (>15 min) per VOI are typically required due to SNR limitations and the time required for the extra encoding. Hence, the acquisition of 2D L-COSY from multiple spatial locations can be very time consuming. Longer scan times demand system stability over a long duration and are less well tolerated by patients.

Figure 30.14 compares the performance of the 4D MEEP-COSY sequence with the 4D EP-COSY sequence. The images show spatial projections of the diagonal Cr peak at 3.9 ppm overlaid on top of a T_1 -weighted axial MRI in the calf muscles of a healthy 28-year-old male volunteer.

Differences between the 2D spectra from soleus, tibialis anterior, and bone marrow from a 26-year-old healthy subject are shown in Figure 30.15. Figure 30.15(a) shows a T_1 -weighted axial MRI annotated to highlight three voxels in the marrow, and in the tibialis and soleus muscles. The 2D COSY spectrum extracted from the soleus (Figure 30.15b) shows resonances in the muscle owing to the *N*-methyl and *N*-methylene protons of Cr (3.0 and 3.9 ppm), the trimethyl amine protons of Cho (3.20 ppm) and taurine (3.35 ppm), and the imidazole protons of carnosine (7.0 and 8.0 ppm), which are not present in the bone marrow (Figure 30.15b). In addition, the diagonal peaks of Cr (3.9 and 3.0 ppm) and other molecules in Figure 30.15(c) from the anterior tibialis show clear splitting due to residual dipole–dipole interactions. The MEEP-COSY data thus demonstrate discrimination of different tissues within the human calf. Similar

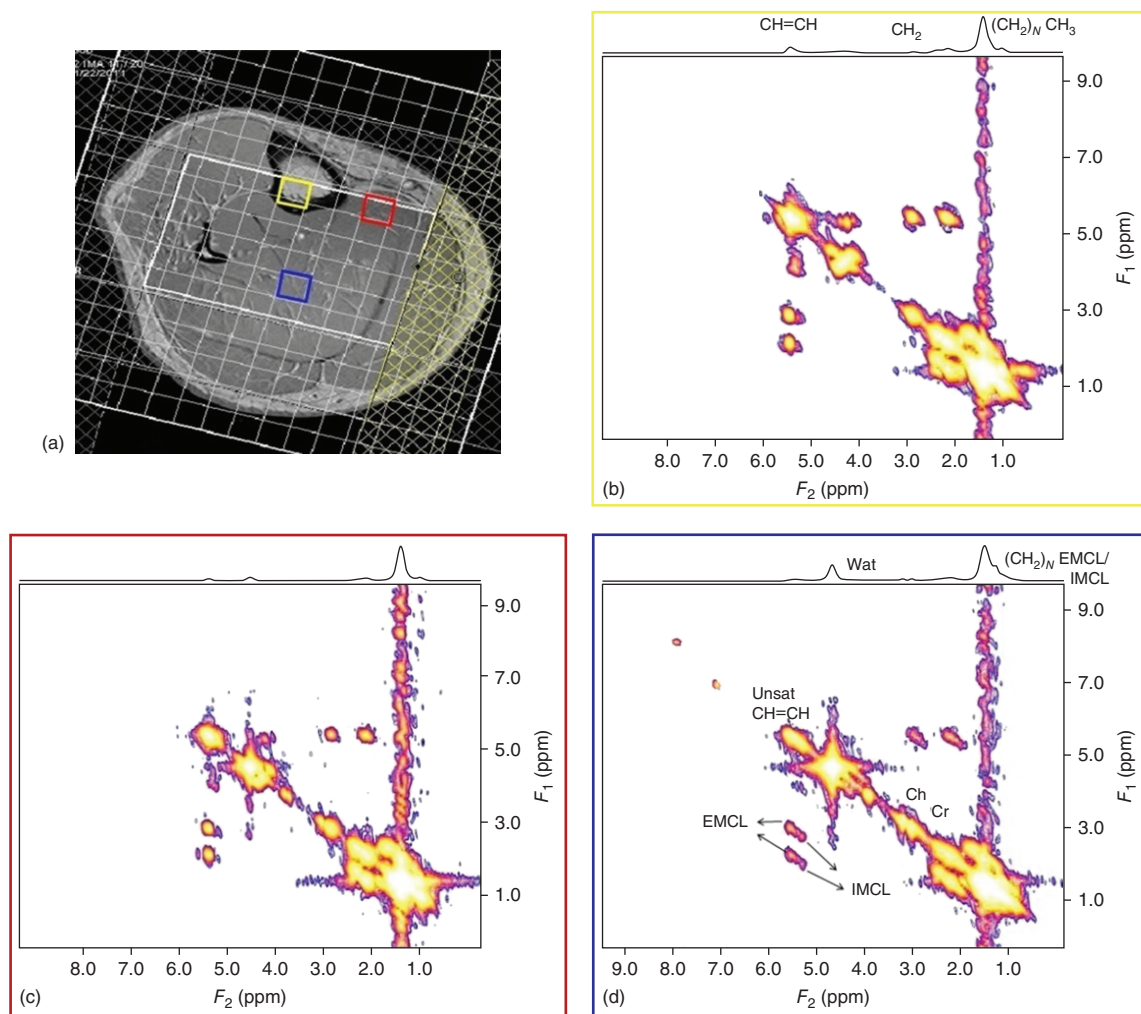


Figure 30.15. (a) T_1 -weighted MRI of a human calf muscle in a 26-year-old healthy volunteer overlaid with an MRSI grid with voxels highlighted in the tibia marrow (yellow), tibialis anterior (red), and soleus (blue) muscles. 2D spectra with 1D diagonal projections (above) for (b) the marrow, (c) tibialis, and (d) soleus voxels

spectra can be obtained using EP-COSY in about 20 min of scan time.

30.4 ACCELERATED ECHO-PLANAR J -RESOLVED MRSI WITH NONUNIFORM UNDERSAMPLING AND COMPRESSED SENSING

Nonuniform undersampling (NUS) of k -space and subsequent reconstruction using compressed sensing (CS) are other ways to accelerate the scan time that

have been successfully implemented in MRI and MRSI.^{113–116} To implement CS successfully, the data should have a sparse representation in some transform domain and the aliasing artifacts produced by the NUS must be incoherent within the transform domain. The CS reconstruction attempts to enforce the sparsity, while simultaneously maintaining the fidelity of the original measurements to within the noise. Although CS has been used in standard CSI, its real advantage comes in multidimensional spectroscopic imaging employing echo-planar methods. Hu *et al.*¹¹⁵ implemented NUS in hyperpolarized

^{13}C spectroscopic imaging along the spatial as well as spectral dimension using pseudo-random phase-encoding blips during the EPSI readout. Furuyama *et al.* and Sarma *et al.* successfully modified the 4D EP-JRESI sequence to accommodate NUS in the $k_y t_1$ plane,^{84,116} while using the EPSI readout gradient to encode the spatial (k_x) and temporal dimensions (t_2). They achieved a twofold acceleration in scan time.

In both of these cases, an exponentially decaying sampling density scheme was used for NUS of the 4D EP-JRESI data. The sampling scheme was defined as

$$\eta(k_y, t_1) = \exp\left(-\frac{|k_y|}{a} - \frac{t_1}{b}\right) \quad (30.16)$$

where $\eta(k_y, t_1)$ is the probability that a data point is sampled, $-k_{y,\max} \leq k_y \leq k_{y,\max}$, $0 \leq t_1 \leq t_{1,\max}$, and a and b are flexible parameters that determine the acquired percentage of data. The CS method solves the constrained optimization problem¹¹³:

$$\arg \min_u \|\Psi u\|_1 \quad \text{s.t.} \quad \|F_p u - d\|_2^2 < \sigma \quad (30.17)$$

where u is the final reconstructed data, Ψ the sparsity transform, F_p the undersampled FT, d the sampled data, σ a fidelity factor, and $\|x\|_n$ the ' ℓ_n -norm'.

To implement EP-JRESI, Furuyama *et al.*¹¹⁶ used the 'total variation' (TV) to enforce sparsity. The constrained problem in equation (30.17) is written as an unconstrained problem,

$$\arg \min_u TV(u) + \frac{\lambda}{2} \|F_p u - d\|_2^2 \quad (30.18)$$

where λ is a regularization parameter that weighs the sparsity against the data consistency, $u = R(x, y, F_1, F_2)$ is the final dataset, F_p is applied only along the y and F_1 dimensions, and $d = r(x, k_y, t_1, F_2)$ is the sampled data. The authors successfully implemented CS-based EP-JRESI in the prostates of healthy human volunteers, detecting the main metabolites citrate, Cr, spermine, Cho, etc.¹¹⁶ They showed that CS reconstruction successfully cleans up the incoherent artifacts with fourfold undersampled data (one-fourth of the $k_y t_1$ points sampled) using two averages.

Sarma *et al.*⁸⁴ used CS-based EP-JRESI to investigate metabolic changes in multiple brain locations of obstructive sleep apnea (OSA) patients and healthy controls. Figure 30.16 shows extracted spectra from two voxels in medial frontal grey and dorsolateral prefrontal white matter regions after CS reconstruction of a fourfold undersampled in vivo brain scan

(fourfold acceleration; two averages) together with the multivoxel display. Despite having only used 25% of the original data, the reconstructed data sets show alterations of metabolic features of OSA patients and healthy human brain⁸⁴ and demonstrate the clinical feasibility of a CS-based 4D EP-JRESI sequence.

Recently, NUS masking schemes and CS reconstruction have also been used to obtain a five-dimensional (5-D; k_x, k_y, k_z, t_2, t_1) in vivo brain acquisition in a clinically feasible scan time.¹¹⁷ Normally this scan would take over 2–3 h, but using an eightfold acceleration factor allows a 21-min acquisition with $k_x = 16$, $k_y = 16$, $k_z = 8$, $t_2 = 256$, $t_1 = 64$, and $\text{TR} = 1.2$ s. Instead of utilizing an NUS scheme in the $k_y t_1$ plane, the nonuniform sampling is performed in the $k_y k_z t_1$ volume using the following sampling density function:

$$\eta(k_y, k_z, t_1) = \exp\left(-\frac{|k_y|}{a} - \frac{|k_z|}{a} - \frac{t_1}{c}\right) \quad (30.19)$$

where $\eta(k_y, k_z, t_1)$ is the probability a data point is sampled, $-k_{y,\max} \leq k_y \leq k_{y,\max}$, $-k_{z,\max} \leq k_z \leq k_{z,\max}$, $0 \leq t_1 \leq t_{1,\max}$, and a , b , and c are adjustable parameters that determine the sample weighting in each dimension. The data are reconstructed in the same manner that the 4D data are reconstructed, using either the ℓ_1 -norm or TV-norm minimization [equations (30.17) and (30.18)]. However, these optimizations must also account for the extra dimension, which increases computation time by an order of magnitude.

Wilson *et al.*¹¹⁷ showed that despite using higher acceleration factors (eightfold), peak integrals of major brain metabolites including NAA, Glx, Cr, Cho, and mI show high reproducibility in vivo. In phantom studies, these same metabolites show very low peak root-mean-square errors (RMSEs), implying that the peaks are properly reconstructed. As this is a novel technique, further validation studies must be conducted and its potential applications in different pathologies determined.¹¹⁸

30.5 PRIOR-KNOWLEDGE FITTING FOR METABOLITE QUANTITATION

A few years ago, Schulte *et al.* developed a prior-knowledge fitting (ProFit) algorithm based on a linear combination of 2D model spectra and demonstrated the feasibility of quantification of brain and prostate metabolites (see Chapter 20).^{34,61,119,120} Unlike the 1D MRS fitting algorithms such as LC

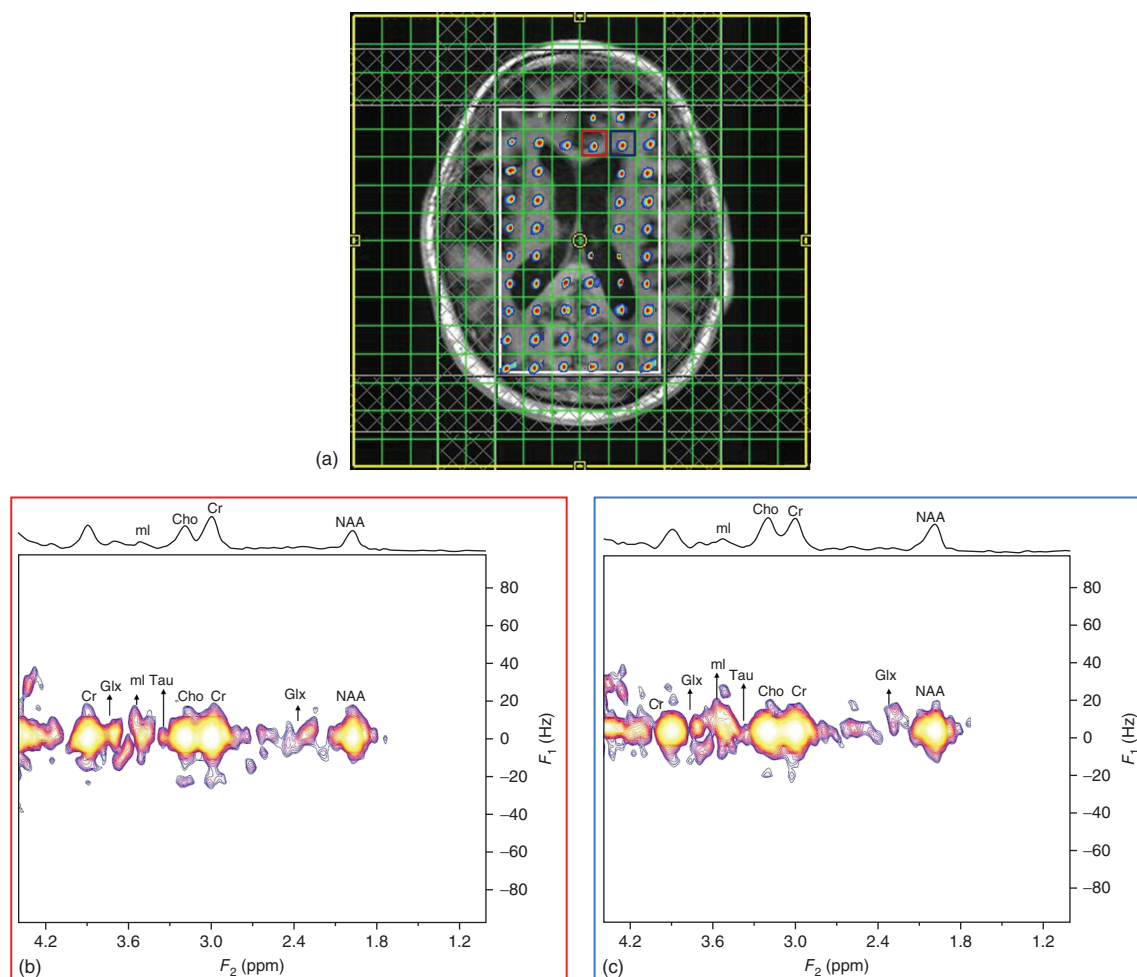


Figure 30.16. Reconstruction of an undersampled 4D EP-JRESI in vivo brain scan of a 69-year-old OSA patient with only 25% of the samples (as required by the Nyquist–Shannon criterion). (a) An MRSI GRID with the diagonal NAA peaks overlaid on top of a T_1 -weighted axial MRI. The white box indicating the PRESS inner-volume localization, containing voxels highlighted in the mid-frontal (red) and left-frontal (blue) brain. The corresponding 2D J -resolved spectra extracted from the mid-frontal and left-frontal voxels are shown in (b) and (c), respectively. (Reproduced with permission from Ref. 84. © American Society of Neuroradiology, 2014)

model and JMRUI,^{4,5} ProFit performs a hybrid time- and frequency-domain fitting using a nonlinear outer loop and an inner linear least-squares fit for obtaining signal amplitudes (proportional to the concentrations) and incorporates the maximum available prior knowledge. Before fitting the data, zeroth-order phase correction and frequency shifts in F_1 and F_2 dimensions are applied to the extracted 2D spectra. After the fitting process, the quality of the fit can be individually evaluated for each metabolite using

Cramer–Rao lower bounds (CRLB) criteria.¹²¹ A statistical lower bound for the achievable standard deviation of the estimated parameters is provided by CRLB, which is not dependent on the individual signal intensities but only on the noise and the orthogonality of the basis function. The architecture of the fitting process allows for another useful measure of the quality of the fitting of the spectrum by comparing the creatine 3.9 ppm (Cr3.9) to the creatine 3.0 ppm (Cr3.0) signal ratio, which ideally should be 1 because

the number of protons (2 and 3, respectively) is already accounted for in their prior-knowledge basis set. Higher Cr3.9/Cr3.0 ratios reflect poor or suspect spectra that may provide grounds for excluding a data set. Note that in order to implement this control, Cr3.9 and Cr3.0 have to be entered as separate elements in the basis sets. Our preliminary results using ProFit quantitation of previously acquired GE 1.5 T, and Siemens 3 T and 1.5 T 2D L-COSY data acquired from several brain pathologies, has demonstrated an improved ability for estimating more brain metabolites such as GSH, phosphocholine (PCh), phosphoethanolamine (PE), and glycerophosphocholine.^{35,45} However, the applicability of ProFit in a clinical setting and multisite testing is yet to be demonstrated.

30.6 FUTURE DIRECTIONS: CLINICAL APPLICATIONS

Localized 2D MRS has left its infancy and is maturing. In contrast to the decades-old SV-based 2D L-COSY and 2D JPRESS spectroscopic sequences, fully-sampled multivoxel-based 4D EP-JRESI and EP-COSI sequences facilitate the recording of 2D COSY and *J*-resolved spectra from multiple regions of the brain. In past, lengthy scan times of approximately 20–40 min and longer have also been a major impediment to clinical 2D MRS, depending on the number of steps for the incremented spectral- (t_1) and spatial-encoding (k_y) dimensions. Now, recent developments demonstrate that further acceleration is possible using NUS schemes, the end result being the shortening of the total scan time for 4D EP-JRESI and EP-COSI sequences to around 10 min or less. Postprocessing of 4D and 5-D NUS data using the nonlinear CS reconstruction schemes such as ℓ_1 -norm-minimization, maximum entropy, and group sparsity is required.

The inclusion of adiabatic RF pulses into the multidimensional MRSI sequences has been a recent interest and different versions of sLASER-based 4D and 5-D EP-COSI/EP-JRESI sequences are currently being investigated for more reliable and quantitative detection of metabolites in the whole brain, other organs, and glands. Future efforts will undoubtedly focus on demonstrating the clinical potential of multidimensional MRSI using fast imaging methods including those described herein. It is our hope that all these recent developments will lead to clinical value for these novel MRSI sequences and create a

new paradigm for noninvasive clinical investigation of normal and diseased states. At the very least, these techniques clearly demonstrate a rich treasure trove of information linking molecules, metabolism, and function that awaits our investigation.

ACKNOWLEDGMENTS

The authors would like to acknowledge the scientific support of Dr. Jonathan Furuyama, Mr. Neil Wilson and Dr. Brian Burns with the NUS-based acquisition schemes and postprocessing using CS algorithms. Also this work was supported by National Institute of Health [R21NS080649 (MAT), R21NS086449 (RN), R01NR013693 (PMM)] and CDMRP Prostate and Breast Cancer Research Programs (#W81XWH-11-1-0248 and W81XWH-10-1-0743, MAT)].

REFERENCES

1. M. Van der-Graaf, *Eur. Biophys. J.*, 2010, **39**, 527. Epub 2009 Aug 13.
2. J. H. Hwang and H. S. Choi, *Exp. Mol. Med.*, 2015, **47**, e139.
3. G. Oz, J. R. Alger, P. B. Barker, R. Bartha, A. Bizzi, C. Boesch, P. J. Bolan, K. M. Brindle, C. Cudalbu, A. Dincer, U. Dydak, U. E. Emir, J. Frahm, R. G. González, S. Gruber, R. Gruetter, R. K. Gupta, A. Heerschap, A. Henning, H. P. Hetherington, F. A. Howe, P. S. Hüppi, R. E. Hurd, K. Kantarci, D. W. Klomp, R. Kreis, M. J. Kruiskamp, M. O. Leach, A. P. Lin, P. R. Luijten, M. Marjańska, A. A. Maudsley, D. J. Meyerhoff, C. E. Mountford, S. J. Nelson, M. N. Pamir, J. W. Pan, A. C. Peet, H. Pop-tani, S. Posse, P. J. Pouwels, E. M. Ratai, B. D. Ross, T. W. Scheenen, C. Schuster, I. C. Smith, B. J. Soher, I. Tkáč, D. B. Vigneron, R. A. Kauppinen, and MRS Consensus Group, *Radiology*, 2014, **270**, 658.
4. S. W. Provencher, *NMR Biomed.*, 2001, **14**, 260.
5. A. Naressi, C. Couturier, I. Castang, R. de Beer, and D. Graveron-Demilly, *Comput. Biol. Med.*, 2001, **31**, 269.
6. J. Pfeuffer, I. Tkac, S. W. Provencher, and R. Gruetter, *J. Magn. Reson.*, 1999, **141**, 104.
7. N. Puts and R. A. E. Edden, *Prog. Nucl. Magn. Reson. Spectrosc.*, 2012, **60**, 29.
8. K. Wakamatsu, H. Tanaka, K. Tabuchi, M. Ojika, F. A. Zucca, L. Zecca, and S. Ito, *Molecules*, 2014, **19**, 8039.

9. J. M. Duarte, K. Q. Do, and R. Gruetter, *Neurobiol. Aging*, 2014, **35**, 1660. Epub 2014 Jan 31.
10. A. M. Weber, N. Soreni, and M. D. Noseworthy, *MAGMA*, 2014, **27**, 291. Epub 2013 Nov 28.
11. M. A. Thomas, R. Nagarajan, A. Huda, D. Margolis, M. K. Sarma, K. Sheng, R. E. Reiter, and S. S. Raman, *NMR Biomed.*, 2014, **27**, 53. Epub 2013 Jul 31.
12. M. A. Thomas, A. Huda, H. K. Chung, N. Binesh, T. Venkatraman, A. Ambrosio, and S. Banakar, *Modern Magn. Reson.*, 2006, 1171. Webb G.A. (ed.).
13. M. Marjańska, E. J. Auerbach, R. Valabrègue, P. F. Van de Moorlele, G. Adriany, and M. Garwood, *NMR Biomed.*, 2012, **25**, 332. Epub 2011 Jul 27.
14. D. L. Rothman, O. A. Petroff, K. L. Behar, and R. H. Mattson, *Proc. Natl. Acad. Sci. U. S. A.*, 1993, **90**, 5662.
15. L. An, Y. Zhang, D. M. Thomasson, L. L. Latour, E. H. Baker, J. Shen, and S. Warach, *J. Magn. Reson. Imaging*, 2009, **30**, 263.
16. W. Bogner, S. Gruber, M. Doelken, A. Stadlbauer, O. Ganslandt, U. Boetcher, S. Trattnig, A. Doerfler, H. Stefan, and T. Hammen, *Eur. J. Radiol.*, 2010, **73**, 526. Epub 2009 Feb 7.
17. C. J. Evans, N. A. Puts, S. E. Robson, F. Boy, D. J. McGonigle, P. Sumner, K. D. Singh, and R. A. Edden, *J. Magn. Reson. Imaging*, 2013, **38**, 970. Epub 2012 Nov 27.
18. M. Mescher, H. Merkle, J. Kirsch, M. Garwood, and R. Gruetter, *NMR Biomed.*, 1998, **11**, 266.
19. P. Bottomley, *Ann. N. Y. Acad. Sci.*, 1987, **508**, 333.
20. J. Frahm, H. Bruhn, M. L. Gyngell, K. D. Merboldt, W. Hänicke, and R. Sauter, *Magn. Reson. Med.*, 1989, **9**, 79.
21. M. Craveiro, C. Cudalbu, V. Mlynárik, and R. Gruetter, *NMR Biomed.*, 2014, **27**, 1151. Epub 2014 Jul 29.
22. A. Andreychenko, V. O. Boer, C. S. Arteaga de Castro, P. R. Luijten, and D. W. Klomp, *Magn. Reson. Med.*, 2012, **68**, 1018. Epub 2011 Dec 28.
23. W. Nosel, L. A. Trimble, J. F. Shen, and P. S. Allen, *Magn. Reson. Med.*, 1989, **11**, 398.
24. M. A. Thomas, H. P. Hetherington, D. J. Meyerhoff, and D. B. Twieg, *J. Magn. Reson.*, 1991, **93**, 485.
25. T. R. Brown, B. M. Kincaid, and K. Ugurbil, *Proc. Natl. Acad. Sci. U. S. A.*, 1982, **79**, 3523.
26. P. A. Bottomley, H. C. Charles, P. B. Roemer, D. Flamig, H. Engeseth, W. A. Edelstein, and O. M. Mueller, *Magn. Reson. Med.*, 1988, **7**, 319.
27. S. Posse and W. P. Aue, *NMR Biomed.*, 1989, **2**, 234.
28. P. R. Luyten, A. J. Marien, W. Heindel, P. H. van Gerwen, K. Herholz, J. A. den Hollander, G. Friedmann, and W. D. Heiss, *Radiology*, 1990, **176**, 791.
29. V. Govind, S. Gold, K. Kaliannan, G. Saigal, S. Falcone, K. L. Arheart, L. Harris, J. Jagid, and A. A. Maudsley, *J. Neurotrauma*, 2010, **27**, 483.
30. J. M. Lupo and S. J. Nelson, *Semin. Radiat. Oncol.*, 2014, **24**, 248. Epub 2014 Jul 26.
31. L. N. Ryner, J. A. Sorenson, and M. A. Thomas, *J. Magn. Reson. B*, 1995, **107**, 126.
32. L. N. Ryner, J. A. Sorenson, and M. A. Thomas, *Magn. Reson. Imaging*, 1995, **13**, 853.
33. R. Kreis and C. Boesch, *J. Magn. Reson.*, 1996, **B113**, 103.
34. R. F. Schulte and P. Boesiger, *NMR Biomed.*, 2006, **19**, 255.
35. M. K. Sarma, A. Huda, R. Nagarajan, C. H. Hinkin, N. Wilson, R. K. Gupta, E. Frias-Martinez, J. Sayre, B. Guze, S. H. Han, and M. A. Thomas, *Metab. Brain Dis.*, 2011, **26**, 173.
36. A. Fuchs, P. Boesiger, R. F. Schulte, and A. Henning, *Magn. Reson. Med.*, 2013. Epub ahead of print.
37. W. P. Aue, E. Bartholdi, and R. R. Ernst, *J. Chem. Phys.*, 1976, **64**, 2229.
38. M. A. Thomas, K. Yue, N. Binesh, P. Davanzo, A. Kumar, B. Siegel, M. Frye, J. Curran, R. Lufkin, P. Martin, and B. Guze, *Magn. Reson. Med.*, 2001, **46**, 58.
39. N. Binesh, K. Yue, L. Fairbanks, and M. A. Thomas, *Magn. Reson. Med.*, 2002, **48**, 942.
40. M. A. Thomas, N. Hattori, U. Umeda, T. Sawada, and S. Naruse, *NMR Biomed.*, 2003, **16**, 245.
41. S. Banakar, N. Wyckoff, A. Huda, A. Marumoto, and S. Raman, *Spectroscopy*, 2003, **17**, 521.
42. N. Binesh, A. Huda, M. Bugbee, R. Gupta, N. Rasgon, A. Kumar, M. Green, S. Han, and M. A. Thomas, *J. Magn. Reson. Imaging*, 2005, **21**, 398.
43. M. A. Thomas, T. Lange, S. S. Velan, R. Nagarajan, S. Raman, A. Gomez, D. Margolis, S. Swart, R. R. Raylman, R. F. Schulte, and P. Boesiger, *MAGMA*, 2008, **21**, 443.
44. P. Srikanthan, A. Singhal, C. C. Lee, R. Nagarajan, N. Wilson, C. K. Roberts, T. J. Hahn, and M. A. Thomas, *Magn. Reson. Insights*, 2012, **5**, 29.
45. R. Nagarajan, M. K. Sarma, A. D. Thames, S. A. Castellon, C. H. Hinkin, and M. A. Thomas, *Int. J. Hepatol.*, 2012, **2012**, 179365.

46. G. Verma, H. Hariharan, R. Nagarajan, R. P. Nanga, E. J. Delikatny, M. Albert Thomas, and H. Poptani, *J. Magn. Reson. Imaging*, 2014, **40**, 1319. Epub 2013 Nov 22.
47. O. W. Sorensen, G. W. Eich, M. H. Levitt, G. Bodenhausen, and R. R. Ernst, *Prog. NMR Spectrosc.*, 1983, **16**, 163.
48. I. M. Brereton, G. J. Galloway, S. E. Rose, and D. M. Doddrell, *Magn. Reson. Med.*, 1994, **32**, 251.
49. R. R. Ernst, G. Bodenhausen, and A. Wokaun, *Principles of NMR Spectroscopy in One and Two Dimensions*, Oxford Publications: Oxford, 1987, 283.
50. M. H. Levitt, *Spin Dynamics: Basics of Nuclear Magnetic Resonance*, John Wiley & Sons, Ltd: Chichester, UK, 2002, 361.
51. J. Keeler, *Understanding NMR Spectroscopy*, John Wiley & Sons: Cambridge, UK, 2002.
52. E. J. Delikatny, W. E. Hull, and C. E. Mountford, *J. Magn. Reson.*, 1991, **94**, 563.
53. U. Klose, *Magn. Reson. Med.*, 1990, **14**, 26.
54. F. Jiru, *Eur. J. Rad.*, 2008, **67**, 202.
55. H. Watanabe, N. Takaya, and F. Mitsumori, *Magn. Reson. Med. Sci.*, 2013, **12**, 215.
56. S. Banakar, T. N. Venkatraman, K. Yue, N. Binesh, and M. A. Thomas, In *Proceedings of International Conference on Mathematics and Engineering Techniques in Medicine and Biological Sciences*. June 24–27, 2002, pp. 500–504.
57. K. Nagayama, K. Wuthrich, and R. R. Ernst, *Biochem. Biophys. Res. Commun.*, 1979, **90**, 305.
58. N. Binesh, K. Yue, and M. A. Thomas, *Proc. Intl. Soc. Mag. Reson. Med.*, 2000, **8**, 1864.
59. M. A. Thomas, L. N. Ryner, M. P. Mehta, P. A. Turski, and J. A. Sorenson, *J. Magn. Reson. Imaging*, 1996, **6**, 453.
60. K. Yue, A. Marumoto, N. Binesh, and M. A. Thomas, *Magn. Reson. Med.*, 2002, **47**, 1059.
61. R. F. Schulte, T. Lange, J. Beck, D. Meier, and P. Boesiger, *NMR Biomed.*, 2006, **19**, 264.
62. S. Macura and L. R. Brown, *J. Magn. Reson.*, 1983, **53**, 529.
63. M. G. Swanson, D. B. Vigneron, T. K. Tran, N. Sailasuta, R. E. Hurd, and J. Kurhanewicz, *Magn. Reson. Med.*, 2001, **45**, 973.
64. P. J. Bolan, L. DelaBarre, E. H. Baker, H. Merkle, L. I. Everson, D. Yee, and M. Garwood, *Magn. Reson. Med.*, 2002, **48**, 215.
65. M. Garwood and L. DelaBarre, *J. Magn. Reson.*, 2001, **153**, 155.
66. T. W. Scheenen, D. W. Klomp, J. P. Wijnen, and A. Heerschap, *Magn. Reson. Med.*, 2008, **59**, 1.
67. T. W. Scheenen, A. Heerschap, and D. W. Klomp, *MAGMA*, 2008, **21**, 95.
68. J. Mao, T. H. Mareci, and E. R. Andrew, *J. Magn. Reson.*, 1988, **79**, 1.
69. J. Pauly, D. Nishimura, and A. Macovski, *J. Magn. Reson.*, 1989, **81**, 43.
70. D. Nishimura and A. Macovski, *J. Magn. Reson.*, 1989, **82**, 571.
71. R. V. Mulkern and J. L. Bowers, *Concepts Magn. Reson.*, 1994, **6**, 1.
72. J. Slotboom, A. F. Mehlkopf, and W. M. M. J. Bovee, *J. Magn. Reson.*, 1991, **95**, 396.
73. A. Allerhand, *J. Chem. Phys.*, 1966, **44**, 1.
74. S. Ramadan and C. Mountford, *J. Magn. Reson. Imaging*, 2011, **33**, 1447.
75. M. Lin, A. Kumar, and S. Yang, *Magn. Reson. Med.*, 2014, **72**, 26. Epub 2013 Oct 1.
76. M. Lin, A. Kumar, and S. Yang, *Magn. Reson. Med.*, 2014, **71**, 911.
77. P. Mansfield, *J. Phys. D Appl. Phys.*, 1983, **16**, L235.
78. P. Mansfield, *Magn. Reson. Med.*, 1984, **1**, 370.
79. S. Matsui, K. Sekihara, and H. Kohno, *J. Magn. Reson.*, 1986, **67**, 476.
80. S. Posse, C. DeCarli, and D. Le-Bihan, *Radiology*, 1994, **192**, 733.
81. S. Posse, G. Tedeschi, R. Risinger, R. Ogg, and D. Le-Bihan, *Magn. Reson. Med.*, 1995, **33**, 34.
82. A. Ebel, B. Soher, and A. Maudsley, *Magn. Reson. Med.*, 2001, **46**, 1072.
83. S. Lipnick, G. Verma, S. Ramadan, J. Furuyama, and M. Thomas, *Magn. Reson. Med.*, 2010, **64**, 947.
84. M. K. Sarma, R. Nagarajan, P. M. Macey, R. Kumar, J. P. Villablanca, J. Furuyama, and M. A. Thomas, *Am. J. Neuroradiol.*, 2014, **35**, S81.
85. Nagarajan R, Furuyama J, Margolis D, S. Raman, M. K. Sarma, and M. A. Thomas, Echo Planar based J Resolved and Correlated Spectroscopic Imaging of Human Prostate Using External Coil, 2011. Published online at www.ismrm.org. Abstract 2801.
86. P. Jezzard, A. S. Barnett, and C. Pierpaoli, *Magn. Reson. Med.*, 1998, **39**, 801.

87. W. Du, Y. P. Du, X. Fan, M. A. Zamora, and G. S. Karczmar, *Magn. Reson. Med.*, 2003, **49**, 1113.
88. J. Hennig, A. Nauerth, and H. Friedburg, *Magn. Reson. Med.*, 1986, **3**, 823.
89. R. Constable, R. Smith, and J. Gore, *J. Comput. Assist. Tomogr.*, 1992, **16**, 41.
90. J. Listerud, S. Einstein, E. Outwater, and H. Y. Kressel, *Magn. Reson. Q.*, 1992, **8**, 199.
91. J. H. Duyn and C. T. W. Moonen, *Magn. Reson. Med.*, 1993, **30**, 409.
92. U. Dydak, D. Meier, R. Lamerichs, and P. Boesiger, *Am. J. Neuroradiol.*, 2006, **27**, 1441.
93. J. K. Furuyama, B. L. Burns, N. E. Wilson, and M. A. Thomas, *Materials*, 2011, **4**, 1818.
94. G. Verma, S. Lipnick, S. Ramadan, R. Nagarajan, and M. A. Thomas, *J. Magn. Reson. Imaging*, 2011, **34**, 262.
95. M. K. Sarma, R. Nagarajan, N. Wilson, J. K. Furuyama, and M. A. Thomas, *Proc. Int. Soc. Mag. Reson. Med.*, 2012, **20**, Abstract 4462.
96. J. K. Furuyama, R. Nagarajan, C. K. Roberts, C. C. Lee, T. J. Hahn, and M. A. Thomas, *NMR Biomed.*, 2014, **27**, 1176.
97. R. Nagarajan, J. Furuyama, M. K. Sarma, D. J. Margolis, S. S. Raman, R. Reiter, and M. A. Thomas. Multi-Echo EP-based J-resolved Magnetic Resonance Spectroscopic Imaging of Prostate Cancer, 2011. Published online at www.rsna2011.rsna.org, Abstract 186.
98. A. Ebel and A. A. Maudsley, *Magn. Reson. Med.*, 2005, **53**, 465.
99. S. Sinha, M. Rathi, A. Misra, V. Kumar, M. Kumar, N. R. Jagannathan, R. M. Pandey, M. Dwivedi, and K. Luthra, *Clin. Endocrinol. (Oxf)*, 2005, **63**, 350.
100. D. A. Pan, S. Lillioja, A. D. Kriketos, M. R. Milner, L. A. Baur, C. Bogardus, A. B. Jenkins, and L. H. Storlien, *Diabetes*, 1997, **46**, 983.
101. K. Levin, H. D. Schroeder, F. P. Alford, and H. Beck-Nielsen, *Diabetologia*, 2001, **44**, 824.
102. M. Torriani, B. J. Thomas, E. F. Halpern, M. E. Jensen, D. I. Rosenthal, and W. E. Palmer, *Radiology*, 2005, **236**, 609.
103. C. Boesch, J. Machann, P. Vermathen, and F. Schick, *NMR Biomed.*, 2006, **19**, 968.
104. B. H. Goodpaster, R. Theriault, S. C. Watkins, and D. E. Kelley, *Metabolism*, 2000, **49**, 467.
105. J. He, S. Watkins, and D. E. Kelley, *Diabetes*, 2001, **50**, 817.
106. F. Schick, B. Eismann, W.-I. Jung, H. Bongers, M. Bunse, and O. Lutz, *Magn. Reson. Med.*, 1993, **29**, 158.
107. C. Boesch, J. Slotboom, H. Hoppeler, and R. Kreis, *Magn. Reson. Med.*, 1997, **37**, 484.
108. L. S. Szczepaniak, E. E. Babcock, F. Schick, R. L. Dobbins, A. Garg, D. K. Burns, J. D. McGarry, and D. T. Stein, *Am. J. Physiol.*, 1999, **276**, E977.
109. X. Li, J. F. Youngren, B. Hyun, G. K. Sakkas, K. Mulligan, S. Majumdar, U. B. Masharani, M. Schambelan, and I. D. Goldfine, *Magn. Reson. Imaging*, 2008, **26**, 188.
110. G. D. Wells, M. D. Noseworthy, J. Hamilton, M. Tarnopolski, and I. Tein, *Can. J. Neurol. Sci.*, 2008, **35**, 31.
111. S. S. Velan, C. Durst, S. K. Lemieux, R. R. Raylman, R. Sridhar, R. G. Spencer, G. R. Hobbs, and M. A. Thomas, *J. Magn. Reson. Imaging*, 2007, **25**, 192.
112. S. S. Velan, N. Said, C. Durst, S. Frisbee, J. Frisbee, R. R. Raylman, M. A. Thomas, V. M. Rajendran, R. G. Spencer, and S. E. Alway, *Am. J. Physiol. Regul. Integr. Comp. Physiol.*, 2008, **295**, R1060.
113. D. Donoho, *IEEE Trans. Info. Theory*, 2006, **52**, 1289.
114. M. Lustig, D. Donoho, and J. M. Pauly, *Magn. Reson. Med.*, 2007, **58**, 1182.
115. S. Hu, M. Lustig, A. Chen, J. Crane, A. Kerr, D. Kelley, R. Hurd, J. Kurhanewicz, S. Nelson, J. Pauly, and D. Vigneron, *J. Magn. Reson.*, 2008, **192**, 258.
116. J. Furuyama, N. Wilson, B. Burns, R. Nagarajan, D. J. Margolis, and M. A. Thomas, *Magn. Reson. Med.*, 2012, **67**, 1499.
117. N. E. Wilson, Z. Iqbal, B. L. Burns, M. Keller, and M. A. Thomas, *Magn. Reson. Med.*, 2016, **75**, 42.
118. N. E. Wilson, B. L. Burns, Z. Iqbal, and M. A. Thomas, *Magn. Reson. Med.*, 2015, **74**, 1199.
119. T. Lange, R. F. Schulte, and P. Boesiger, *Magn. Reson. Med.*, 2008, **59**, 966.
120. M. A. Thomas, T. Lange, S. S. Velan, R. Nagarajan, S. Raman, A. Gomez, D. Margolis, S. Swart, R. R. Raylman, R. F. Schulte, and P. Boesiger, *Magn. Reson. Mater. Phys. Biol. Med.*, 2008, **21**, 443.
121. S. Cavassila, S. Deval, C. Huegen, D. van Ormondt, and D. Graveron-Demilly, *J. Magn. Reson.*, 2000, **143**, 311.

Prostate Cancer Detection Using Accelerated 5D EPJRESI - sLASER Combined With DWI

Rajakumar Nagarajan¹, Zohaib Iqbal¹, Neil Wilson¹, Daniel J Margolis¹, Steven S Raman¹, Robert E Reiter², and M.Albert Thomas¹

¹Radiological Sciences, University of California Los Angeles, Los Angeles, CA, United States, ²Urology, University of California Los Angeles, Los Angeles, CA, United States

Synopsis

Prostate cancer (PCa) is the second leading cause of cancer related death in Western countries. Conventional 3D MRSI in PCa using weighted encoding and long echo time. One dimensional MRSI suffers from overlapping of metabolites. In this study, a non-uniformly undersampled (NUS) five dimensional (5D) echo planar J-Resolved spectroscopic imaging (EP-JRESI) sequence using semi LASER radio-frequency pulses for optimal refocusing was used to record 2D J-resolved spectra from multiple prostate locations and to quantify changes in prostate metabolites, Cit, Cr, Ch and ml after compressed sensing reconstruction of the NUS 5D EP-JRESI data by minimizing total variation method. Also, we found the prostate metabolites ratios (Ch+Cr/Cit and Ch+Cr/ml) were inversely correlated with ADC values.

Purpose/Introduction

Prostate cancer (PCa) is the most common cancer, other than skin cancer, among American men. The accuracy of prostate MRI has improved over the past decade, partly relating to advances in scanner and receiver coil hardware. However, it has been the emergence of diffusion-weighted imaging (DWI) as a central component of prostate MRI acquisition and interpretation that has been crucial to MRI's current impact. Apparent diffusion coefficient (ADC) values derived from DWI are significantly associated with tumor aggressiveness shown in several studies (1-3). Overlap of metabolites is a major limitation in one-dimensional (1D) spectral-based single voxel MR Spectroscopy (MRS) and multivoxel-based MR spectroscopic imaging (MRSI). By combining echo-planar spectroscopic imaging (EPSI) with two-dimensional (2D) J resolved spectroscopic sequence (JPRESS), 2D spectra can be recorded in single (4) and multiple slices of prostate using five dimensional (5D) Echo-Planar J-Resolved Spectroscopic Imaging (EP-JRESI) (5). Compressed Sensing (CS) is a technique for accelerating the inherently slow data acquisition process, and is well suited for MRSI due to its intrinsic denoising effect. In this study, semi LASER (sLASER) based 5D EP-JRESI was used to quantitate changes in prostate metabolites (citrate (Cit), creatine (Cr), choline (Ch) and myoinositol (ml)) using compressed sensing reconstruction by minimizing total variation method and correlated with DWI findings.

Materials and Methods

The NUS based 5D EP-JRESI sequence and the conventional DWI were evaluated in nine PCa patients (mean age 64.0 years) using a 3T MRI scanner (Siemens Medical Systems, Germany) using endorectal 'receive' coil. Axial DWI images were recorded using the single-shot echo planar imaging technique using the following imaging parameters: TR/TE= 2000/83 ms, 27cm FOV, 4-mm slice thickness, 0 mm intersection gap, 3 averages. Isotropic diffusion weighted images were obtained by using diffusion gradients with three b-values (0, 50 and 400 sec/mm²) along three directions of motion-probing gradients. In the 5D EP-JRESI data, CS reconstruction was then performed by solving the total variation minimization problem using the linearized Bregman iteration. The 5D EP-JRESI parameters were: FOV = 160x160x120 mm³, image matrix = 16x16x8, spectral width (F₂) = 1190 Hz, number of spectral points = 256, TE = 41ms, TR = 1.2s, Avg=1. For the second dimension (F₁), 64 increments with bandwidths of 1000Hz were used. Data acquisition included water-suppressed (WS) and non-water-suppressed (NWS) scans (20 mins). The NWS scan was used to perform eddy current and spectral phase correction. A 8X NUS scheme was imposed along the two spatial dimensions (k_y, k_z and t₁). Extractable individual voxel volume in prostate was 1.5 ml. The 5D EP-JRESI data acquired in the PCa patients were extracted and post-processed using a homebuilt MATLAB-based (The Mathworks, Natick, MA, USA) library of programs. The FWHM was approximately 18Hz observed in all the PCa patients. Eight patients were investigated using the 3T Prisma and one using the 3T Trio-Tim scanner. A p-value of <0.05 was considered significant.

Results

Fig.1 shows the ADC values of PCa patients in cancer and non-cancer regions. The mean and standard deviation (SD) ADC values were: 1.18 ±0.05 and 1.51 ±0.10-3 mm²/sec in cancer and unaffected regions. Significant changes observed between cancer and non-cancer regions (p<0.05). Using the NUS based 5D EP-JRESI data, 2D peaks due to Cit, Ch, Cr and ml, were quantified in cancer and non-cancer regions using the home-developed peak integration MATLAB code. Figs. 2 shows the (Ch+Cr)/Cit and (Ch+Cr)/ml of cancerous and non-cancerous regions processed using total variation method. The mean metabolite ratios and SD of (Ch+Cr)/Cit of cancer and non-cancerous regions processed using TV was: 0.379 ±0.094 and 0.228 ±0.69. Similarly (Ch+Cr)/ml was: 4.531 ±1.60 and 3.137 ±1.56. Fig.3 shows the Cit and Ch metabolites map of 65 year old PCa patient processed using 5D EP-JRESI data. Significant changes observed in (Ch+Cr)/Cit and (Ch+Cr)/ml in cancer and non-cancer regions. The metabolites ratios were inversely correlated with ADC values (p<0.05).

Discussion

In this study, we observed increased (Ch+Cr)/Cit and (Ch+Cr)/ml ratios in the cancer compared to non-cancer locations which agree with our earlier findings of slice based four dimensional (4D) EP-JRESI technique (4). Decrease in zinc is a prerequisite to the decrease in citrate level in prostate cancer (6). The osmoregulator myo-inositol is expressed in a variety of tissues, and its decrease was observed in PCa within human expressed prostatic secretions (EPS) using high resolution NMR (7).

Conclusion

The advantage of compressed sensing based 5D EP-JRESI sequence is in recording short TE-based spectra from multiple regions of human prostate and it can be easily combined with DWI and other protocols. These pilot findings need further validation using larger cohorts.

Acknowledgements

This work was supported by CDMRP grant from the US Army Prostate Cancer Research Program: (#W81XWH-11-1-0248).

References

1. Kobus T, Vos PC, Hambrock T, et al. Prostate cancer aggressiveness: in vivo assessment of MR spectroscopy and diffusion-weighted imaging at 3 T. *Radiology*. 2012;265:457-467.
2. Nagarajan R, Margolis D, Raman SS, et al. Correlation of Gleason scores with diffusion-weighted imaging findings of prostate cancer. *Adv Urol*. 2012;2012:374805.
3. Yagci AB, Ozari N, Aybek Z, Duzcan E. The value of diffusion-weighted MRI for prostate cancer detection and localization. *Diagn Interv Radiol*. 2011;17:130-134.
4. Nagarajan R, Iqbal Z, Burns B, et al. Accelerated echo planar J-resolved spectroscopic imaging in prostate cancer: a pilot validation of non-linear reconstruction using total variation and maximum entropy. *NMR Biomed*. 2015 Nov; 28(11):1366-73.
5. Wilson NE, Iqbal Z, Burns BL, et al. Accelerated five-dimensional echo planar J-resolved spectroscopic imaging: Implementation and pilot validation in human brain. *Magn. Reson. Med*. 2015. doi: 10.1002/mrm.25605.
6. Costello LC, Franklin RB, Narayan P. Citrate in the diagnosis of prostate cancer. *Prostate*. 1999 Feb 15; 38(3):237-45.
7. Serkova NJ, Gamito EJ, Jones RH, et al. The metabolites citrate, myo-inositol, and spermine are potential age-independent markers of prostate cancer in human expressed prostatic secretions. *Prostate* 2008 May 1; 68(6):620-8.

Abstract ID: 3558

Figures

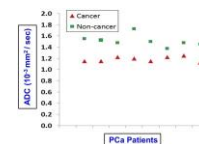


Fig.1. ADC values of PCa patients in cancer and non-cancer regions

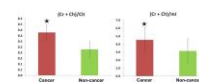


Fig.2. (Ch+Cr)/Cit and (Ch+Cr)/ml of cancerous and non-cancerous regions processed using total variation

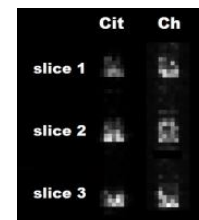


Fig.3. Cit and Ch metabolites map of 65 year old PCa patient processed using 5D EP-JRESI data

Resolution Enhanced accelerated Four Dimensional Echo Planar Spectroscopic Imaging: Application in Prostate Cancer

Zohaib Iqbal¹, Brian L. Burns¹, Rajakumar Nagarajan¹, Robert E. Reiter², Steven S. Raman¹, and M. Albert Thomas¹

¹Radiological Sciences, University of California - Los Angeles, Los Angeles, CA, United States, ²Urology, University of California - Los Angeles, Los Angeles, CA, United States

Synopsis

Prostate cancer (PCa) remains the most prevalent form of cancer in men. For diagnosis, Prostate-Specific Antigen (PSA) levels are most commonly used as a screening tool. In addition, chemical shift imaging (CSI) methods can provide information on the biochemical concentrations in different regions of the prostate. Here, we demonstrate a novel technique capable of improving spatial and spectral resolution for the accelerated echo-planar J-resolved spectroscopic imaging (EP-JRESI) method, which obtains 2 spatial and 2 spectral dimensions in a single scan. This resolution enhanced EP-JRESI (RE-JRESI) method is evaluated in PCa patients and compared to the EP-JRESI results.

Introduction

Prostate cancer (PCa) is the second leading cause of cancer related deaths among men in the United States¹. Chemical shift imaging (CSI)² can be used to aid in the diagnosis of PCa when used in conjunction with the Prostate-Specific Antigen (PSA) test. One technique capable of improving spectral dispersion while retaining spatial resolution when compared to the CSI method is the accelerated echo planar J-resolved spectroscopic imaging (EP-JRESI) technique^{3,4}. However, spatial resolution and spectral resolution along the indirect spectral domain remain low. Using cubic convolution interpolation in the spatial domain and a covariance transformation in the spectral domain, we present a novel resolution enhanced EP-JRESI (RE-JRESI) technique and show applications of this method in PCa.

Methods

Acquisition and Reconstruction: Data were acquired as previously discussed⁴ on a Siemens 3T Trio scanner (Siemens Healthcare, Erlangen, Germany). Data were acquired as (k_x, k_y, t_2, t_1) , where k_x, k_y are the spatial dimensions and t_2, t_1 are the direct and indirect temporal dimensions, respectively. The following acquisition parameters were used for the phantom and in vivo acquisitions: (k_x, k_y, t_2, t_1) points = (16,16,512,64), voxel resolution = $1 \times 1 \times 1 \text{ cm}^3$, TE/TR = 30/1500ms, direct spectral bandwidth = 1190Hz, and indirect spectral bandwidth = 1000Hz. All fifteen in vivo subjects with PCa (mean age = 60 years old) were consented as per the IRB protocol, and were scanned using the endo-rectal coil in addition to the body coil. For prostate phantom measurements, which included citrate (Cit), creatine (Cr), phosphocholine (PCh), spermine (Spm), myo-Inositol (ml), glutamate+glutamine (Glx), only the body coil was used.

A non-uniform sampling scheme was applied to the k_y, t_1 volume³ in order to accelerate the scan by a factor of four-fold (4x). Data were subsequently reconstructed by maximizing the entropy of the data, as previously described in detail⁵.

Resolution Enhancement: After performing the acquisition and reconstruction steps above, the data were transformed into (x, y, F_2, t_1) , where x, y are the spatial dimensions and F represents the spectral dimension. First, cubic convolution interpolation⁶ was applied iteratively to each spatial point for all F_2, t_1 points. Cubic interpolation utilizes 4×4 points from the original image and interpolates a continuous plane by evaluating the values and derivatives in all directions of these points. The whole image is interpolated by stringing these continuous planes together, while keeping the derivatives at the boundaries of these planes equivalent. Spatial resolution was enhanced from 16×16 to 128×128 in this manner using the built in `imresize` command in MATLAB. Afterwards, the F_2, t_1 data in each voxel in the 128×128 grid underwent a covariance transformation⁷ to yield a covariance spectrum, S . If A is a data set in F_2, t_1 for a single voxel, the covariance transformation is performed using the following:

$$S = [Re(A) \cdot Re(A^T)]^{\frac{1}{2}} + [Im(A) \cdot Im(A^T)]^{\frac{1}{2}}$$

Above, Re and Im are the real and imaginary parts of A , respectively, $[\]^{\frac{1}{2}}$ is the matrix square root operator, and T is the transpose. The covariance transformation using this method improves indirect spectral resolution by a factor of 6.7 with the acquisition parameters above. The combined spatial/spectral resolution enhanced method was applied in phantom and in vivo to evaluate the performance of this method.

Results

Figure 1 shows the spatial comparison of the regular EP-JRESI, or JRESI, and the RE-JRESI method for Cit, Cr, and choline metabolite maps, which are displayed through projecting peak volumes. Figures 2 and 3 show axial MRIs of the prostate (A), along with citrate metabolite maps (B), and choline metabolite maps (C). Locations with high choline and low citrate are indicative of cancerous tissues. The high choline areas seen in both figures (C) agree with clinical biopsy results. Finally, Figure 4 shows the spectral comparison between the J-resolved spectrum and the resolution enhanced covariance J-resolved (RE-Cov) spectrum for both healthy and cancerous tissues shown in Figure 2.

Discussion and Conclusion

The RE-JRESI method is a novel technique capable of improving both spatial and spectral resolution of an EP-JRESI acquisition. The primary benefit of the spatial enhancement is that metabolite images can be directly overlaid onto MRIs, which may be especially useful in the clinic. Spectral resolution improvement may also allow for more accurate detection of metabolites, which will be investigated in the future. Future studies will focus on evaluating the quantitative benefit of using RE-JRESI compared to EP-JRESI and applying this method in five dimensions⁸.

Acknowledgements

The authors would like to acknowledge the UCLA Dissertation Year Fellowship, and the NIH R21 (NS080649-02) grant.

References

1. Siegel RL, Miller KD, Jemal A. Cancer statistics, 2015. *CA: a cancer journal for clinicians* 2015;65:5-29.
2. Brown T, Kincaid B, Ugurbil K. NMR chemical shift imaging in three dimensions. *Proceedings of the National Academy of Sciences* 1982;79:3523-3526.
3. Furuyama JK, Wilson NE, Burns BL, et. al. Application of compressed sensing to multidimensional spectroscopic imaging in human prostate. *Magnetic Resonance in Medicine* 2012;67:1499-1505.
4. Nagarajan R, Iqbal Z, Burns B, et. al. Accelerated echo planar J-resolved spectroscopic imaging in prostate cancer: a pilot validation of non-linear reconstruction using total variation and maximum entropy. *NMR in Biomedicine* 2015;28:1366-1373.
5. Burns B, Wilson NE, Furuyama JK, Thomas MA. Non-uniformly under-sampled multidimensional spectroscopic imaging in vivo: maximum entropy versus compressed sensing reconstruction. *NMR in Biomedicine* 2014;27:191-201.
6. Keys R. Cubic convolution interpolation for digital image processing. *IEEE transactions on acoustics, speech, and signal processing* 1981;29:1153-1160.
7. Brüschweiler R, Zhang F. Covariance nuclear magnetic resonance spectroscopy. *The Journal of chemical physics* 2004;120:5253-5260.
8. Wilson NE, Iqbal Z, Burns BL, et. al. Accelerated Five-dimensional echo planar J-resolved spectroscopic imaging: Implementation and pilot validation in human brain. *Magnetic Resonance in Medicine* 2016;75:42-51.

Figures

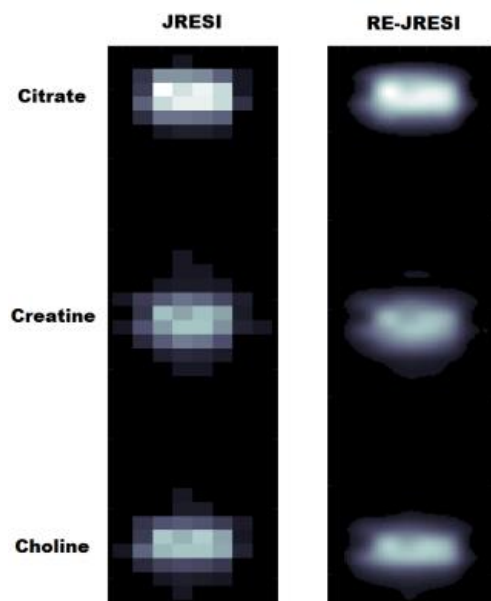


Figure 1. Metabolite maps of Citrate, Creatine, and Choline are shown for both the EP-JRESI, or JRESI method, (left) and the RE-JRESI (right). All maps were produced by integrating over the peak ranges for the desired metabolite signal.

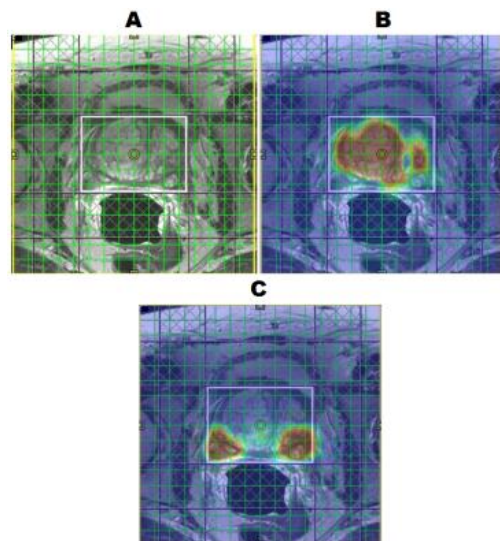


Figure 2. An axial MRI from a 3+3 PCa patient can be seen in (A). The citrate (B) and choline (C) metabolite maps are also displayed on top of the axial MRI. Areas with high choline and low citrate correspond to cancerous tissues, as confirmed by a biopsy.

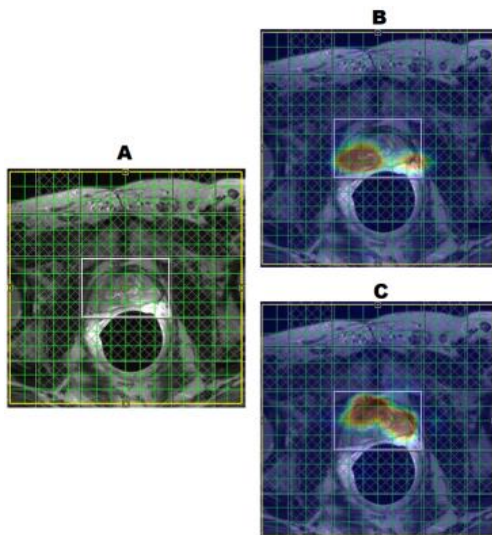


Figure 3. An axial MRI from a 4+4 PCa patient can be seen in (A). The citrate (B) and choline (C) metabolite maps are also displayed on top of the axial MRI. Areas with high choline and low citrate correspond to cancerous tissues, as confirmed by a biopsy.

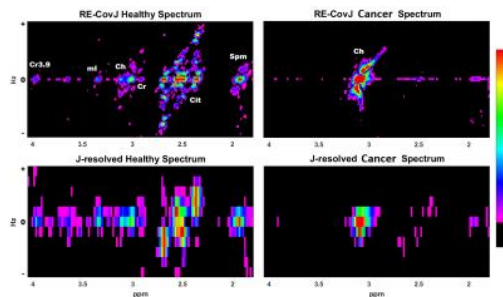


Figure 4. Spectral comparison between the resolution enhanced covariance J-resolved spectra (top) and the J-resolved spectra (bottom) are shown for both cancerous tissue (right) and healthy tissue (left). These voxels were taken from the 3+3 PCa patient shown in Figure 2.